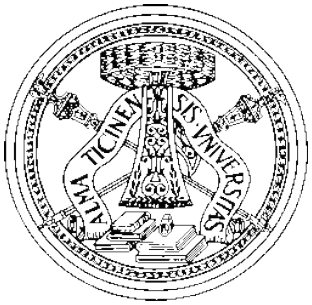

Università degli Studi di Pavia
Facoltà di Ingegneria
Dipartimento di Ingegneria Civile e Architettura
Degree of Doctor in Philosophy

Multiscale Patient-Specific Computational Fluid Dynamics to Assess Thoracic Aortic Hemodynamics

Supervisor:
Prof. Michele Conti

Author:
Anna Ferrarini

Coadvisor:
Prof. Alessandro Veneziani

Academic year 2020/2021

Ci sarà sempre un'altra opportunità, un'altra amicizia, un altro amore, una nuova forza. Per ogni fine c'è sempre un nuovo inizio.

Antoine de Saint-Exupery

Abstract

Thoracic aorta is the first portion of the main artery of the systemic circulation, i.e., the aorta, supplying oxygenated blood to main organs of our body. For this reason, it is evident that an impairment of its function can have dramatic impact on the overall circulation. Among the aortic diseases, arteriosclerotic (degenerative) disease represents the most common cause of thoracic aneurysms. A detailed comprehension of the local hemodynamic change and of the effects of vascular walls modification on the flow could be very useful in predicting the disease progression. The development of Computational Fluid Dynamics (CFD), also due to the increasing in the power of electronic computers and algorithms, has contributed to a significant improvement in vascular research. In this context, CFD simulations are less invasive than in vivo experiments and potentially more accurate and flexible than in vitro ones. CFD simulations can be performed by solving all the length scales of motion, i.e. Direct Numerical Simulation (DNS), or using alternative, but corroborated, approaches, like Reynolds Averaged Navier-Stokes (RANS) equations or Large-Eddy Simulation (LES). Due to the moderate/large Reynolds number and complex geometries, DNS could be significantly computationally expensive in aneurysmatic aortic simulations. Several studies demonstrated that LES models are promising candidates for hemodynamic problems, with high efficiency and accuracy. In three-dimensional (3D) CFD simulations the treatment of boundary conditions still represents a critical aspect. Recently, a widely used choice consists in the prescription of particular lumped parameter (or 0D) models, leading to the coupled 3D-0D models. These lumped parameter models allow to prescribe patient-specific boundary conditions, by tuning the parameter values according to the available measurements of patients. The enforcement of lumped parameters models as boundary conditions of 3D ones corresponds to the prescription of Neumann boundary conditions. However, it is known that Neumann boundary condition is more prone to numerical instabilities. In particular, Neumann outlet boundary conditions in presence of flow reversal at the outlets lead to the so called backflow instability. The goal of this work is to provide a set of tools and a clear workflow aiming at performing accurate and

efficient CFD simulations with acceptable computational cost on both healthy and diseased patients. First, we derive, implement, and assess some particular lumped parameter models, useful for coupling to more sophisticated 3D models. Then, a patient-specific 3D-0D model is studied to investigate the impact of the transcatheter aortic root procedure on coronary perfusion. Moreover, a comparison between the coupled 3D-0D model and the full 0D model is addressed. Another prominent aim of this work consists in proving that a particular LES model, i.e. the Smagorinsky model, provides an accurate solution for patient-specific simulations, and controls the occurrence of backflow instability by a proper selection of the Smagorinsky coefficient. The application of CFD in other vascular regions is presented as well; we focus on a case study concerning the intra-stent thrombotic apposition that occurred in two patients undergoing endovascular treatment for popliteal arterial aneurysm.

Acknowledgements

First of all, I would like to thank my supervisor, Prof. Michele Conti, for his support and encouragement to push my limits (especially on teaching/conference activities), and for providing a collaborative research environment. I hope we can keep in touch.

A warmly thanks to my coadvisor, Prof. Alessandro Veneziani. His passion and enthusiasm for his work impressed me from the minicourse on mathematical models for the cardiovascular system, organized by him at the University of Verona, during my Master's degree. I will always be grateful to him for kindly inviting me to his lab at Emory University in fall 2019, for his teachings and advice, and for making me feel at home, together with Manuela, in the huge Atlanta.

I would like to thank Proff. Ferdinando Auricchio, Alessandro Reali, and Simone Morganti, who trusted me and gave me the opportunity to begin the PhD. In particular, thank to Prof. Ferdinando Auricchio for the precious advices, and for supporting me during the research period in Atlanta.

Thank to all the CompMech group, in particular to Alessia, Alice, Franca, Michele, Giulia, Maddalena, Valentina, Luigi, Massimo, and Rodrigo for all the laughs and for making Pavia less gray. Another thank to the ex CompMech components: Laura, Daniele, Gaetano, Jessica, Giorgione, Guillermo, Mauro, Alfredo, Gianmaria, Lorenzo, and especially to Alex (thank you for helping and advising me when I needed).

Thanks to my historical and loyal friend Arianna, who always listens to me patiently, with the power to calm me down.

An affectionate thanks to all the friends met in Atlanta: Malena, Maura, Sasha, Raquel, Ohiane, Tania, Cristina, Caterina, Jialin, Marcelo, Irving, Kelvin. A special thank to: Quimi, to always making me laugh and allowing to eat his Peruvian recipes; Kashif, for never getting bored of winning table tennis against me; and mostly to the Fun group (i.e. Philipp, Demet, and Nicolas), for all the great moments that we spent together, I'll never forget them (if my time in Atlanta was awesome it was thanks to you, I hope to see you all soon).

A special thank to my family for the support in all the choices that I have

taken and their affection.

Last but not the least, thanks to Fabio, for your unconditional love, encouragement, and tolerance during the lockdown. Without your love and constant support I probably wouldn't have finished my PhD.

Contents

List of Figures

List of Tables

Chapter 1

Introduction

Cardiovascular diseases are the leading cause of death in the Western world [1]. In particular, one person dies every 36 seconds in the United States from cardiovascular disease [2]. Cardiovascular diseases include heart and blood vessel diseases, such as stroke, aortic aneurysms, and peripheral artery disease. The aorta is the main artery in the human body, originating from the left ventricle of the heart and extending down to the abdomen, where it splits into two smaller arteries (the common iliac arteries). The aorta could be anatomically divided into a thoracic section and an abdominal section: the thoracic aorta goes from heart to diaphragm, the abdominal aorta extends from diaphragm to the aortic bifurcations. The most common thoracic aortic diseases are aneurysm and dissection. A thoracic aortic aneurysm is a permanent, localized, congenital or acquired dilatation of the thoracic aorta. An aortic dissection is a disruption of the medial layer of the aorta resulting in the separation of the layers of the aortic wall.

Recently, the development of Computational Fluid Dynamics (CFD) as well as the advances in electronics and mathematical algorithms have produced a significant improvement in vascular research. A detailed comprehension of the local hemodynamic change, of the effects of vascular wall modification on the flow pattern, of the gradual adaptation of the global system as a result of surgery, is possible with the use of sophisticated computer simulations and could be extremely useful to accurately set up therapeutic and/or surgical treatments [3].

The first and simplest model simulating the cardiovascular system was developed by Frank in 1899 [4] and was called lumped parameter model (or 0D model). By exploiting the analogy between hydraulic and electric circuits, it includes a peripheral resistance and a compliance, in order to represent the arterial system as a single elastic chamber. However, this first model does not allow to describe the phenomenon of pulse wave propagation throughout the

arterial tree, and flow rate and pressure waveforms at different districts of the circulatory system. This model has been refined several times over the years (Jager et al. [5], Westerhof et al. [6], Avolio [7], Schumacher et al. [8],...) in order to provide more reliable results. For example, Avolio [7] proved a good agreement with experimental measurements, by implementing a lumped parameter model with 128 segments corresponding to the central vessels and major peripheral arteries. Nowadays, the most widely used lumped parameter models allow to provide simulations of large parts of the systemic circulation, including systemic dynamics, such as feedback mechanisms [9], at low computational cost. However, the straightforward interpretation of the results risks being too little detailed, especially in the pathological cases. To overcome this drawback, the lumped parameter models have been coupled with more sophisticated three-dimensional (3D) ones, arising the so-called geometrical multiscale approach.

The geometrical multiscale approach includes dimensionally heterogeneous models, in order to represent the interactions between local and systemic hemodynamics [3]. The term *multiscale* does not only refer to the coupled 3D-0D models, but also to those coupled with the one-dimensional (1D) ones, i.e. 3D-1D or 3D-1D-0D. This approach calls 3D models only in those regions where a detailed knowledge of the hemodynamic is required, while 1D and 0D models are applied to represent the remainder of the vascular tree [10]. The present thesis does not deal with 1D models, except to provide a rigorous derivation of lumped parameter models. Several groups successfully performed 3D-0D blood flow simulations [11]-[15]. However, CFD simulations involving 3D-0D models are still critical for two main reasons, i.e. the computational cost and the treatment of boundary conditions.

Direct Numerical Simulations (DNS) are the most widely used in CFD simulations featured by laminar flow and low Reynolds number. However, in aortic simulations, DNS may require high computational cost to solve the smallest significant scales of flow, especially in aortic diseased simulations in which flow could become turbulent. For example, such computational cost is not compatible with a large number of patients, like in a computer-aided clinical trial. Reynolds-Averaged Navier-Stokes (RANS) equations and Large-Eddy Simulations (LES) represent alternative approaches to DNS. RANS models reduce significantly the computational cost compared to both DNS and LES, yet they decrease the accuracy [16]. LES models have been proved to be more suitable on modeling the disturbed nature of flow [17]. Therefore, in Chapter 5 we will consider a LES model to describe turbulent flows.

Another challenge in modern CFD simulations is represented by the treatment of boundary conditions. Typically, we do not have all data we need for the

correct statement of the mathematical problem. As matter of fact, for either practical or ethical reasons, three scalar data on each point of the boundary are seldom (or never) available. Also, available data are affected by noise and measurement errors and, sometimes, inconsistencies. Surrogate models must be advocated to replace the missing data, yet introducing arbitrary choices resulting in additional errors. In Chapters 3 and 5, we impose Neumann boundary conditions, in order to prescribe the pressure at the outlet of the 3D model and at the inlet of the 0D one, since velocity boundary data are mostly inaccessible in patient-specific setting. However, the prescription of Neumann outlet boundary conditions in presence of flow reversal at the outlets leads to a numerical instability, called backflow instability. This numerical problem occurs due to the energy injection caused by the convective term of the Navier-Stokes equations. Xu et al. [18] proved theoretically and numerically that a particular deconvolution-based LES model is able to suppress the occurrence of the backflow instability. Given such encouraging outcomes, in Chapter 5 we will use a LES model, i.e. the Smagorinsky model, already implemented in the commercial software Ansys Fluent, to prove that it provides accurate results, comparing with the DNS, and controls the backflow instability, thanks to a reasonable selection of the LES parameter.

Finally, we present two clinical cases concerning the intra-stent thrombotic apposition occurring after endovascular treatment for popliteal arterial aneurysm (PAA) [19]. Intra-stent thrombosis is one of the major failure models of endovascular repair to treat PAA. In Appendix, we will perform patient-specific CFD analyses of popliteal stenting assuming different boundary conditions and assessing the impact of leg bending [20].

Overall, this framework aims at providing a basis for performing accurate and efficient patient-specific simulations that can help clinical research in reasonable computational time. All the aspects just described find a place in this thesis, which is structured as follows:

- Chapter 2 focuses on the derivation and some applications of lumped parameter models. First, it provides the derivation of 1D models from the 3D ones, thanks to conservation principles. Then, the lumped parameter models are retrieved from the 1D model, by an averaging procedure and applying some approximations. Moreover, it introduces some example of lumped parameter models that could be useful in clinical research, such as a 0D describing the entire systemic circulation, one the peripheral circulation (i.e. the three-element Windkessel model), and one the circulation of coronary arteries.

- Chapter 3 illustrates a coupled 3D-0D model of aneurysmatic ascending aorta including the coronary ostia. DNS simulations were performed in

order to investigate the impact of a particular endovascular procedure on the coronary circulation. This study was conducted in collaboration with Cardiocentro Ticino, Lugano.

- Chapter 4 presents the main properties of LES models and a brief review of the most common LES models found in literature. In particular, more details about the Smagorinsky model are discussed, since it is used in Chapter 5 to perform patient-specific simulations.

- Chapter 5 deals with a LES model, i.e. the Smagorinsky model, for thoracic aortic aneurysms. The parameter estimation of the LES model is not trivial, in particular with high Reynolds number and complex geometry. This calibration could be very useful in each engineering application dealing with CFD simulations and turbulence models. The main purpose of this section is to prove that the Smagorinsky model both provides accurate results and stabilizes the backflow instability, by a proper selection of the Smagorinsky coefficient. Qualitative and quantitative analyses are conducted from the results of the patient-specific simulations related to three patients with aortic aneurysm. This study started during my research period abroad (September-December, 2019) at Emory University under the supervision of Prof. A. Veneziani.

- Chapter 7 draws the conclusions of this thesis, focusing on the ideal framework to perform the most accurate and efficient patient-specific simulations. Future developments are also discussed.

- Appendix 1 introduces CFD simulations based on two patients undergoing endovascular treatment for popliteal arterial aneurysm. This study is part of the PERFEKT project led by Dr. B. Pane, Dr. G. Salsano (San Martino Hospital, Genova) and Prof. M. Conti, and funded by the Italian Ministry of Health.

- Appendix 2 reports all the lumped parameter values estimated in the present thesis.

Chapter 2

Lumped parameter models

CFD simulations are usually based on three-dimensional models, described by the Navier-Stokes equations, which govern fluid mechanics. However, the high computational cost, the difficult modeling of the circulatory system through different length scales, required to represent the blood flow from the large aorta to the smaller blood vessels, have led to the development of reductive models. The latter models can provide reliable results even if they are simplified with respect to the local physiology.

As many reductive models can be considered, at the beginning of the first year of PhD program we focused on derivation and implementation of lumped parameter (or 0D) models describing the systemic circulation.

2.1 Derivation of lumped parameter models

In the next section, 1D models will be derived from the 3D Navier-Stokes equations, directly using the conservation principles. Then, we will obtain the equations representing the lumped parameter model from the 1D equations (see section 2.1.2). Some applications will also be introduced.

2.1.1 From 3D to 1D models

1D models are such models in which the space dependence is reduced only to the axial coordinate. We assume that the fluid is incompressible, Newtonian, and with constant viscosity. Then, the Navier-Stokes equations write:

$$\rho\frac{\partial \mathbf{u}}{\partial t} + (\mathbf{u}\cdot\nabla)\mathbf{u} - \mathrm{div}(\mathbf{T}) = \rho\mathbf{f}^b$$
$$\nabla\cdot\mathbf{u} = 0$$

where $\mathbf{u}(\mathbf{x},t) = \big(u_1(x,y,z,t), u_2(x,y,z,t), u_3(x,y,z,t)\big)$ is the velocity field, $\mathbf{T}$ the Cauchy stress tensor, and $\mathbf{f}^b$ denotes the body forces.

There are (at least) two ways to derive 1D models:

- assuming cylindrical symmetry and integrating the Navier-Stokes equations on a generic section (L. Formaggia et al. [21]);
- using the conservation principles (L. Formaggia et al. [3]).

Here we follow the second approach, since it is more general and does not require simplifying assumptions on the geometry of the vessel section.

We consider a simple compliant tube as a model of the artery, with volume V_t, boundary $\partial V_t = \partial V_{t,w} \cup S_1 \cup S_2$, and outer normal $\mathbf{n}$. S_1 (fixed), S_2 (fixed), S are assumed normal to the x-axis. The axis of the vessel is rectilinear and coincides with the x-axis (see Figure 2.1).

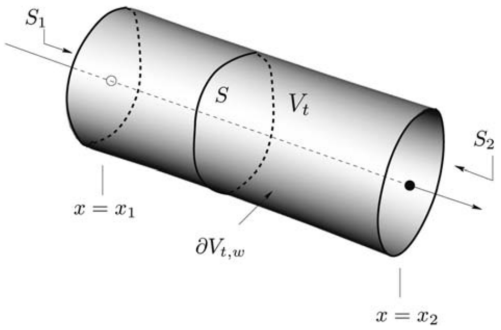

Figure 2.1: Notation used to describe a simple compliant tube [3].

Before deriving the equations of the 1D model, we recall the Reynolds' transport theorem and some useful definitions.

Theorem (Reynolds' transport theorem)
Let $f = f(\boldsymbol{x},t)$ be a continuous function, then

$$\frac{d}{dt}\int_{V_t} f\, dV = \int_{V_t} \frac{\partial f}{\partial t}\, dV + \int_{\partial V_t} f\ \mathbf{u}_b \cdot \mathbf{n}\, d\sigma, \tag{2.1.1}$$

where $\mathbf{x} = (x,y,z)$ and $\mathbf{u}_b$ is the velocity of the boundary of V_t.

From the previous assumptions:

$$\mathbf{u}_b \cdot \mathbf{n} = 0 \qquad \text{on } S_1,\ S_2$$
$$\mathbf{u}_b = \mathbf{u}_w \qquad \text{on } \partial V_t$$

The relative velocity between the arterial wall and the fluid at the lumen is defined as $\mathbf{w} = \mathbf{u}_w - \mathbf{u}$. Then, we can write the second term on the right in equation (2.1.1) as:

$$\begin{aligned}\int_{\partial V_t} f\ \mathbf{u}_b \cdot \mathbf{n}\, d\sigma &= \int_{\partial V_{t,w}} f\ \mathbf{u}_w \cdot \mathbf{n}\, d\sigma \\ &= \int_{\partial V_{t,w}} f\ \mathbf{w} \cdot \mathbf{n}\, d\sigma + \int_{\partial V_{t,w}} f\ \mathbf{u} \cdot \mathbf{n}\, d\sigma.\end{aligned}$$

We introduce the area-averaged value of f, given by

$$\overline{f} = \frac{1}{A}\int_S f\, d\sigma, \qquad \text{where } A = \int_S d\sigma. \tag{2.1.2}$$

where $A = A(x,t) = \int_S d\sigma$ is the area of the section S. Using equation (2.1.2), then

$$\int_{V_t} f\, dV = \int_{x_1}^{x_2} \left(\int_S f\, d\sigma\right) dx = \int_{x_1}^{x_2} A\overline{f}\, dx,$$

and the left hand side of the equation of the Reynolds' transport theorem becomes:

$$\frac{d}{dt}\int_{V_t} f\, dV = \frac{d}{dt}\left(\int_{x_1}^{x_2} A\overline{f}\, dx\right) = \int_{x_1}^{x_2} \frac{\partial}{\partial t}(A\overline{f})\, dx,$$

since x_1 and x_2 are independent of time. Focusing on the right hand side of the equation (2.1.1), we observe that

$$\begin{aligned}\int_{\partial V_{t,w}} f\ \mathbf{u} \cdot \mathbf{n}\, d\sigma &= \int_{\partial V_t} f\ \mathbf{u} \cdot \mathbf{n}\, d\sigma - \int_{S_1} f\ \mathbf{u} \cdot \mathbf{n}\, d\sigma - \int_{S_2} f\ \mathbf{u} \cdot \mathbf{n}\, d\sigma \\ &= \int_{\partial V_t} f\ \mathbf{u} \cdot \mathbf{n}\, d\sigma + \int_{S_1} f u_1\, d\sigma - \int_{S_2} f u_1\, d\sigma.\end{aligned}$$

Thanks to the Gauss' theorem and using the area-averaged quantity, we obtain

$$\begin{aligned}\int_{\partial V_{t,w}} f\ \mathbf{u} \cdot \mathbf{n}\, d\sigma &= \int_{\partial V_t} f\ \mathbf{u} \cdot \mathbf{n}\, d\sigma + \int_{S_1} f u_1\, d\sigma - \int_{S_2} f u_1\, d\sigma \\ &= \int_{V_t} \nabla \cdot (f\mathbf{u})\, dV - \int_{x_1}^{x_2} \frac{\partial}{\partial x}\Big(A(\overline{f u_1})\Big)\, dx.\end{aligned}$$

The final form of the one-dimensional Reynolds' transport theorem is

$$\begin{aligned}\int_{x_1}^{x_2} \frac{\partial}{\partial t}(A\overline{f})\,dx &= \int_{V_t} \frac{\partial f}{\partial t}\,dV + \int_{\partial V_{t,w}} f\ \mathbf{w}\cdot\mathbf{n}\,d\sigma + \int_{\partial V_{t,w}} f\ \mathbf{u}\cdot\mathbf{n}\,d\sigma \\ &= \int_{V_t} \frac{\partial f}{\partial t}\,dV + \int_{\partial V_{t,w}} f\ \mathbf{w}\cdot\mathbf{n}\,d\sigma - \int_{x_1}^{x_2} \frac{\partial}{\partial x}\Big(A(\overline{fu_1})\Big)\,dx \\ &\quad + \int_{V_t} \nabla\cdot(f\mathbf{u})\,dV \\ &= \int_{x_1}^{x_2} \left(\int_S \frac{\partial f}{\partial t}\,d\sigma\right)\,dx + \int_{x_1}^{x_2} \left(\int_{\partial S} f\ \mathbf{w}\cdot\mathbf{n}\,d\gamma\right)\,dx + \\ &\quad + \int_{x_1}^{x_2} \left(\int_S \nabla\cdot(f\mathbf{u})\,d\sigma\right)\,dx - \int_{x_1}^{x_2} \frac{\partial}{\partial x}\Big(A(\overline{fu_1})\Big)\,dx.\end{aligned}$$

Since it is true for any values of x_1 and x_2, then the one-dimensional Reynolds' transport theorem reads:

$$\frac{\partial}{\partial t}(A\overline{f}) + \frac{\partial}{\partial x}\Big(A(\overline{fu_1})\Big) = \int_S \left(\frac{\partial f}{\partial t} + \nabla\cdot(f\mathbf{u})\right)\,d\sigma + \int_{\partial S} f\mathbf{w}\cdot\mathbf{n}\,d\gamma.$$

Starting from the latter equation, we use the conservation principles, i.e. conservation of mass and balance of momentum, to derive the equations representing the 1D model. Concerning the conservation of mass, we consider $f = 1$, then

$$\frac{\partial A}{\partial t} + \frac{\partial}{\partial x}(A\bar{u}_1) = \int_{\partial S} \mathbf{w}\cdot\mathbf{n}\,d\gamma,$$

recalling that we are assuming incompressible fluids (i.e., $\nabla\cdot\mathbf{u} = 0$). For the balance of momentum, taking $f = u_1$, we get

$$\frac{\partial}{\partial t}(A\bar{u}_1) + \frac{\partial}{\partial x}\Big(A\overline{u_1^2}\Big) = \int_S \left(\frac{\partial u_1}{\partial t} + \mathbf{u}\cdot\nabla u_1\right)\,d\sigma + \int_{\partial S} u_1\mathbf{w}\cdot\mathbf{n}\,d\gamma, \quad (2.1.3)$$

thanks to the property: $\nabla\cdot(\mathbf{u}u_1) = \mathbf{u}\cdot\nabla u_1 + u_1\nabla\cdot\mathbf{u} = \mathbf{u}\cdot\nabla u_1$. Using the material derivative ($\frac{D}{Dt} = \frac{\partial}{\partial t} + \mathbf{u}\cdot\nabla$), then equation (2.1.3) becomes:

$$\frac{\partial}{\partial t}(A\bar{u}_1) + \frac{\partial}{\partial x}\Big(A\overline{u_1^2}\Big) = \int_S \frac{Du_1}{Dt}\,d\sigma + \int_{\partial S} u_1\mathbf{w}\cdot\mathbf{n}\,d\gamma. \quad (2.1.4)$$

In order to calculate the first term on the right in equation (2.1.4), we recall the balance of momentum for a generic volume V_t :

$$\begin{aligned}\int_{V_t} \frac{D}{Dt}(\rho\mathbf{u})\,dV &= \mathbf{F}_v + \mathbf{F}_s \\ &= \int_{V_t} \rho\mathbf{f}^b\,dV + \int_{\partial V_t} \mathbf{T}\mathbf{n}\,d\sigma,\end{aligned}$$

where $\mathbf{f}^b$ is the body force. Dividing by ρ and using the divergence theorem we obtain

$$\int_{V_t} \frac{D\mathbf{u}}{Dt}\, dV = \int_{V_t} \mathbf{f}^b\, dV + \frac{1}{\rho}\int_{V_t} \nabla \cdot \mathbf{T}\, dV.$$

Invoking the constitutive equation for the fluid, i.e. $\mathbf{T} = -p\mathbf{I} + \mathbf{D}$ (p is the pressure, $\mathbf{I}$ the identity tensor, $\mathbf{D}$ the tensor of deviatoric stresses), and setting $\nabla \cdot \mathbf{D} = \mathbf{d}$, then

$$\int_{x_1}^{x_2} \left(\int_S \frac{D\mathbf{u}}{Dt}\, d\sigma \right) dx = \int_{x_1}^{x_2} \left[\int_S \left(\mathbf{f}^b + \frac{1}{\rho}(-\nabla p + \mathbf{d}) \right) d\sigma \right] dx. \tag{2.1.5}$$

Since x_1 and x_2 can be arbitrarily chosen, we could write the x-component of the latter equation (2.1.5) as

$$\int_S \frac{Du_1}{Dt}\, d\sigma = \int_S \left(f_1^b + \frac{1}{\rho}\Big(-\frac{\partial p}{\partial x} + d_1\Big) \right) d\sigma. \tag{2.1.6}$$

Substituting (2.1.6) in the previous equation (2.1.4) gives

$$\begin{aligned} \frac{\partial}{\partial t}(A\bar{u}_1) + \frac{\partial}{\partial x}\Big(A\overline{u_1^2}\Big) &= \int_S \left(f_1^b + \frac{1}{\rho}\Big(-\frac{\partial p}{\partial x} + d_1\Big) \right) d\sigma + \int_{\partial S} u_1 \mathbf{w}\cdot\mathbf{n}\, d\gamma \\ &= \frac{A}{\rho}\left(\rho \bar{f}_1^b - \frac{\partial \bar{p}}{\partial x} + \bar{d}_1 \right) + \int_{\partial S} u_1 \mathbf{w}\cdot\mathbf{n}\, d\gamma. \end{aligned} \tag{2.1.7}$$

The term $\overline{u_1^2}$ in this equation is handled by defining a momentum-flux correction coefficient α (sometimes called the Coriolis coefficient), which is a function of the velocity profile, as

$$\overline{u_1^2} = \frac{1}{A}\int_S u_1^2\, d\sigma = \alpha \bar{u}_1^2. \tag{2.1.8}$$

The term representing the viscous forces $\bar{d}_1$ is taken to be a linear function of $\bar{u}_1$ of the form:

$$\frac{A}{\rho}\bar{d}_1 = -k_R \bar{u}_1, \tag{2.1.9}$$

where k_R denotes the viscous resistance of the flow per unit length of the tube. Therefore, using equations (2.1.8) and (2.1.9), the balance of momentum (2.1.7) reads:

$$\frac{\partial}{\partial t}(A\bar{u}_1) + \frac{\partial}{\partial x}\Big(A\alpha\bar{u}_1^2\Big) = A\bar{f}_1^b - \frac{A}{\rho}\frac{\partial \bar{p}}{\partial x} - k_R\bar{u}_1 + \int_{\partial S} u_1 \mathbf{w}\cdot\mathbf{n}\, d\gamma.$$

This latter equation can be further simplified assuming that the lumen is impermeable, i.e. $\mathbf{w}\cdot\mathbf{n} = 0$, and the body forces are negligible, i.e. $\bar{f}_1^b = 0$.

Moreover, simplifying the notation by denoting $u = \bar{u}_1$ and $p = \bar{p}$ and defining the mass flux across a section as $Q = Au = \int_S u_1 \, d\sigma$, we obtain the final form of the 1D model:

$$\frac{\partial A}{\partial t} + \frac{\partial Q}{\partial x} = 0 \tag{2.1.10}$$

$$\frac{\partial Q}{\partial t} + \frac{\partial}{\partial x}\left(\alpha \frac{Q^2}{A}\right) + \frac{A}{\rho}\frac{\partial p}{\partial x} + k_R \frac{Q}{A} = 0 \tag{2.1.11}$$

Since the number of unknowns (A, Q, and p) of the system (2.1.10)-(2.1.11) exceeds the number of equations, a common way to close the system is to introduce a relation between the pressure p and the vessel area A. In particular, an algebraic relationship can be derived by assuming static equilibrium in the radial direction of a cylindrical tube, i.e.,

$$p = P_{ext} + \beta\Big(\sqrt{A} - \sqrt{A_0}\Big),$$

where P_{ext} is the external pressure (assumed constant), $A_0 = A_0(x)$ the sectional area of the vessel, and

$$\beta = \frac{\sqrt{\pi} h_0 E}{(1-\nu^2)A_0}. \tag{2.1.12}$$

In equation (2.1.12), h_0 denotes the vessel thickness, E the Young modulus, and ν the Poisson ratio.

2.1.2 From 1D to 0D models

Lumped parameter models are models in which the space dependence is discretised, by splitting the cardiovascular system into a set of compartments. They are often represented in terms of hydraulic or electric networks.

We consider a single artery Ω as our domain, with length $\ell = |x_2 - x_1|$. The 0D model is derived from the 1D model by an averaging procedure. Firstly, we define the following mean quantities:

- mean flow rate over the artery

$$\hat{Q} = \frac{1}{\ell}\int_{x_1}^{x_2} Q(x)\, dx, \tag{2.1.13}$$

- mean pressure over the artery

$$\hat{p} = \frac{1}{\ell}\int_{x_1}^{x_2} p\, dx,$$

- mean area over the artery

$$\hat{A} = \frac{1}{\ell} \int_{x_1}^{x_2} A \, dx.$$

Starting from equations (2.1.10) and (2.1.11), we integrate the continuity equation along the axial direction ($x_1 \leq x \leq x_2$) to obtain

$$\ell \frac{d\hat{A}}{dt} + Q_2 - Q_1 = 0, \tag{2.1.14}$$

where $Q_1(t) = Q(t, x_1)$ and $Q_2(t) = Q(t, x_2)$.

In considering the conservation of momentum, we add two further assumptions:

- the convective term $\frac{\partial}{\partial x}\left(\alpha \frac{Q^2}{A}\right)$ can be neglected;
- the variation of A with respect to x is small compared to that of p and Q; thus, A can be replaced with a constant value A_0.

The first assumption is a good approximation to represent the peripheral circulation, where blood flow is quite slow. The second assumption is reasonable when the axial average is carried out over short segments [3]. Averaging over x of the equation representing the balance of momentum of the 1D model (2.1.11), we get

$$\int_{x_1}^{x_2} \frac{\partial Q}{\partial t} \, dx + \frac{A_0}{\rho} \int_{x_1}^{x_2} \frac{\partial p}{\partial x} \, dx + k_R \int_{x_1}^{x_2} \frac{Q}{A_0} \, dx = 0.$$

Using the definition of the mean flow rate (2.1.13) and multiplying by ρ/A_0, we obtain

$$\frac{\rho \ell}{A_0} \frac{d\hat{Q}}{dt} + \frac{\rho k_R \ell}{A_0^2} \hat{Q} + P_2 - P_1 = 0, \tag{2.1.15}$$

where $P_1(t) = P(t, x_1)$, $P_2(t) = P(t, x_2)$. Combining the equations (2.1.14) and (2.1.15), the 0D model is described by:

$$\ell \frac{d\hat{A}}{dt} + Q_2 - Q_1 = 0 \tag{2.1.16}$$

$$\frac{\rho \ell}{A_0} \frac{d\hat{Q}}{dt} + \frac{\rho k_R \ell}{A_0^2} \hat{Q} + P_2 - P_1 = 0 \tag{2.1.17}$$

Since the latter system has more unknowns than the number of equations, a common way to close the system is to introduce a relation between the pressure and the area, i.e.:

$$\frac{d\hat{A}}{dt} = k_1 \frac{d\hat{p}}{dt}, \tag{2.1.18}$$

where k_1 is a constant depending on the geometry and the material property [3]. Substituting (2.1.18) into the continuity equation (2.1.16) we obtain:

$$k_1 \ell \frac{d\hat{p}}{dt} + Q_2 - Q_1 = 0 \tag{2.1.19}$$

that, together with the momentum equation (2.1.17), represents the lumped parameter model for a vessel.

Before the introduction of performance computers, early simulations of flow for the cardiovascular system were based on the analogy between hydraulic and electric circuits. Indeed, the flow rate can be seen as a current, the pressure as voltage, blood viscosity as a resistance, and the wall compliance as a capacitance (see Table 2.1). Using this electrical analogy, we recast the system of

Hydraulic	**Electric**
Pressure	Voltage
Flow rate	Current
Blood viscosity	Resistance R
Blood inertia	Inductance L
Wall compliance	Capacitance C

Table 2.1: Analogy between hydraulic and electric networks.

equations (2.1.19) and (2.1.17) as:

$$C\frac{d\hat{p}}{dt} + Q_2 - Q_1 = 0 \tag{2.1.20}$$

$$L\frac{d\hat{Q}}{dt} + R\hat{Q} + P_2 - P_1 = 0 \tag{2.1.21}$$

where $R = \frac{\rho k_R \ell}{A_0^2}$ represents the resistance induced to the flow by the blood viscosity, $L = \frac{\rho \ell}{A_0}$ the inductance of the flow, $C = k_1 \ell$ the mass storage term in the mass conservation law, due to the compliance of the vessel. Again, the system of equations (2.1.20) and (2.1.21) has more unknowns than the number of equations; thus, boundary conditions and further assumptions are needed in order to close the system. For instance, the following four assumptions could be used to close the system:

1. given Q_1, P_2 and approximating $\hat{p} \approx P_1$, $\hat{Q} \approx Q_2$ (reasonable for a short pipe), then the system becomes

$$C\frac{dP_1}{dt} + Q_2 = Q_1 \tag{2.1.22}$$
$$L\frac{dQ_2}{dt} + RQ_2 - P_1 = -P_2 \tag{2.1.23}$$

   which corresponds to the so called $\mathcal{L}$-network (see Figure 2.2 (1));

2. given P_1, Q_2 and approximating $\hat{p} \approx P_2$, $\hat{Q} \approx Q_1$ (reasonable for a short pipe), then the system becomes

$$C\frac{dP_2}{dt} - Q_1 = -Q_2 \tag{2.1.24}$$
$$L\frac{dQ_1}{dt} + RQ_1 + P_2 = P_1 \tag{2.1.25}$$

   which corresponds to the so called $\mathcal{L}$-inverted network (see Figure 2.2 (2));

3. given P_1, P_2, then the system becomes

$$\frac{dP}{dt} - \frac{1}{C}Q_1 + \frac{1}{C}Q_2 = 0 \tag{2.1.26}$$
$$\frac{dQ_1}{dt} + \frac{2}{L}P + \frac{R}{L}Q_1 = \frac{2}{L}P_1 \tag{2.1.27}$$
$$\frac{dQ_2}{dt} - \frac{2}{L}P + \frac{R}{L}Q_2 = -\frac{2}{L}P_2 \tag{2.1.28}$$

   which corresponds to the so called $\mathcal{T}$-network (see Figure 2.2 (3));

4. given Q_1, Q_2, then the system becomes

$$\frac{dP_1}{dt} + \frac{2}{C}Q = \frac{2}{C}Q_1 \tag{2.1.29}$$
$$\frac{dQ}{dt} - \frac{1}{L}P_1 + \frac{R}{L}Q + \frac{1}{L}P_2 = 0 \tag{2.1.30}$$
$$\frac{dP_2}{dt} - \frac{2}{C}Q = -\frac{2}{C}Q_2 \tag{2.1.31}$$

   which corresponds to the so called π-network (see Figure 2.2 (4)).

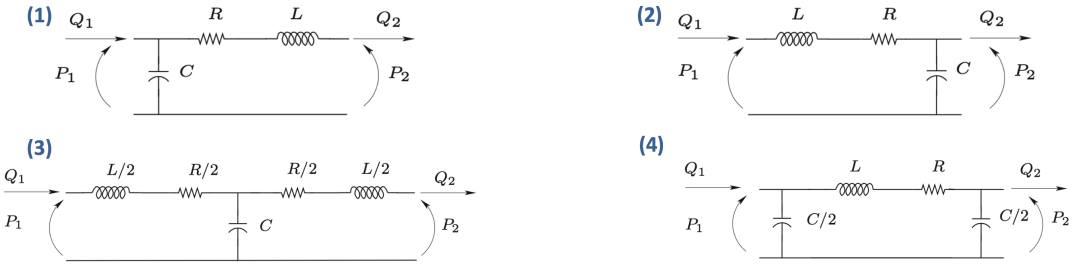

Figure 2.2: (1) $\mathcal{L}$-network; (2) $\mathcal{L}$-inverted network; (3) $\mathcal{T}$-network; (4) π-network.

2.2 0D model of systemic circulation: the Westerhof model

At the beginning of the first year of PhD program, we focused on the derivation and implementation of a lumped parameter model describing the systemic arterial tree, starting from the work written by N. Westerhof et al. in 1969 [6]. The main idea consists in representing the human arterial vascular tree by a finite number of cylindrical segments, modeled by electrical components (see Figure 2.3). In particular, each box illustrated in Figure 2.3 corresponds to a portion of the human arterial tree, whose dimensions, wall and hemodynamic properties have been useful in the parameter estimation involved in the whole electric circuit and in the type of the electric network used to represent each compartment. Indeed, the parameter values of the symmetrical π-networks, used to model each segment, have been tuned according to the radius, the length, the wall thickness, and the Young's modulus of the corresponding compartment, i.e.:

$$R_n = \frac{8\pi\eta}{S^2} n\Delta z, \qquad L_n = \frac{\rho}{S}\frac{1}{2n-1}\Delta z, \qquad C = \frac{3\pi r^2(a+1)^2}{E(2a+1)}\Delta z, \tag{2.2.1}$$

where η denotes the viscosity of the blood, $S = \pi r^2$ the section considered, Δz the length of the arterial segment, ρ the density of the blood, r the radius of the arterial segment, h the wall thickness, $a = r/h$ the ratio of the radius and the wall thickness, E the Young's modulus of the vessel wall, and $n = 1, ..., 5$ depending on the radius. The values of radii and wall thickness used by Westerhof et al. [6] in their electric circuit were taken from Noordergraaf [22] and referred to a subject with a mass of 75 kg and a height of 175 cm. The blood density and viscosity assumed by Westerhof et al. was 1.05 $g\ cm^{-3}$ and 0.03 P, respectively, according to Noordergraaf et al. [23]. Notice that the networks used to describe the segments are symmetrical π-networks, in

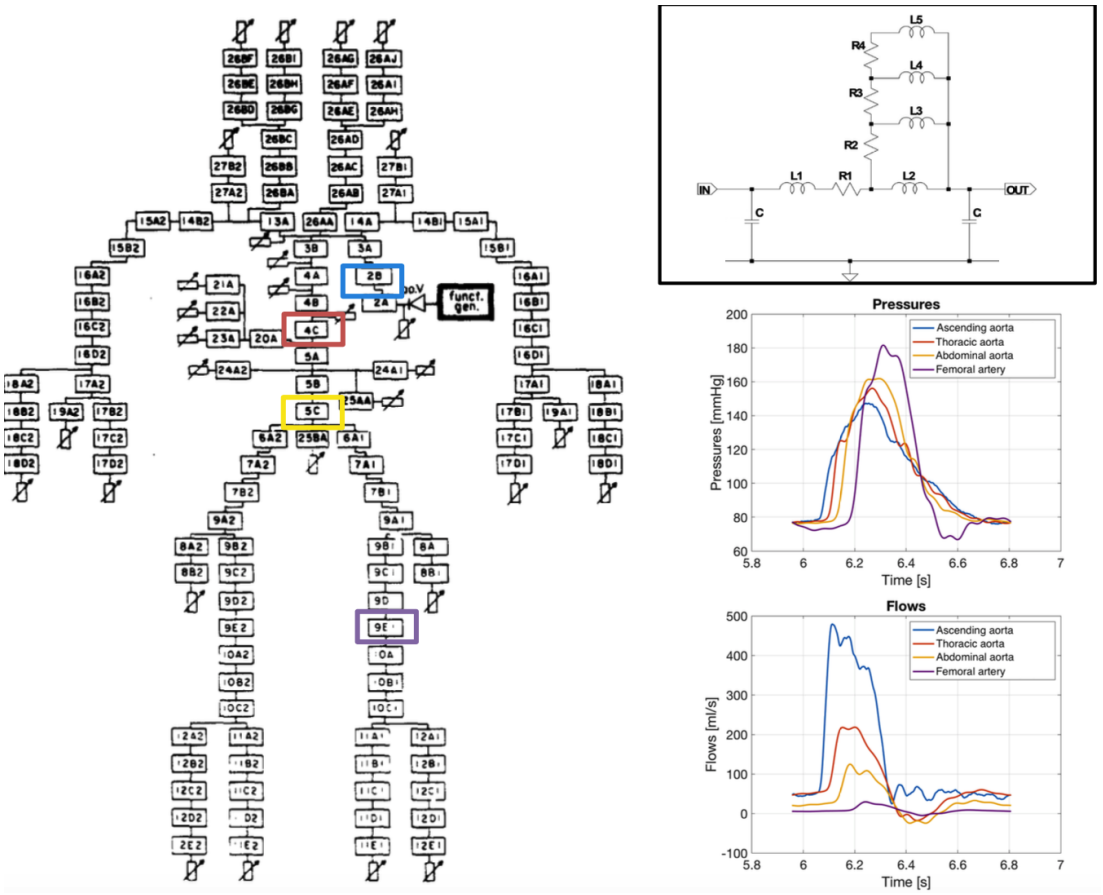

Figure 2.3: Left: scheme of electrical model of the human systemic arterial tree divided into 121 blocks, as represented in Westerhof et al. [6]. Right, top: electrical representation of a segment of artery corresponding to a block of the entire electrical model illustrated on the left. Right, bottom: pressure and flow rate waveforms obtained from the lumped parameter model reproduced in Simulink, corresponding to the segments of ascending aorta, thoracic aorta, abdominal aorta, and femoral artery.

order to reduce errors introduced by lumping at higher frequencies, with additional correction networks. This correction network, including the resistances R_2,..., R_n and the inductances L_2,..., L_n represented in Figure 2.3, stems for the so called sleeve effects, i.e. the phenomena given by the interactions between viscous and inertial forces induced by the pulsatility of blood flow [5]. The value of n can reach at most 5, depending on the radius of the specific segment, i.e. how the pulsatility impact on the hemodynamic in the arterial compartment under consideration. For example, $n = 5$ in the segments near

the heart corresponding to the ascending aorta up to the abdominal aorta, then its value decreases until $n = 3$ in the peripheral arteries, such as tibial and radial arteries. The total number of arterial segments in which the electric network has been composed by Westerhof et al. is 121. Moreover, the model includes peripheral resistances for each of the terminal segments, represented by potentiometers and illustrated by rectangles with arrows in Figure 2.3. The pumping action of the left heart is represented by a waveform synthesizer. The original electric circuit built by Westerhof et al. operates at one thousand the real frequencies, i.e. 10^3 Hz, which means that the time and all the values of inductance and capacitance correspond to 10^{-3} the real ones. This was done in order to avoid impractically and expensive large capacitance and inductance values.

While Westerhof et al. [6] built a real electric network to simulate the systemic arterial circulation, our goal is to reproduce this same model exploiting the new technology by using Simulink. We maintain the same data reported by Westerhof et al. for the parameter estimation of the model and the same frequencies. The transient inlet flow rate waveform taken from Westerhof et al. has been prescribed at the inlet. In particular, instead of using a waveform synthesizer, we extract the values of the flow rate waveform, using the software WebPlotDigitizer 4.4 (WebPlotDigitizer). Then, the data obtained by the literature waveform are interpolated using the software Matlab R2018a (The Mathworks Inc.). The resulting transient inflow waveform, shown in Figure 2.4, is imposed at the inlet of the lumped parameter model implemented in Simulink. A critical step is represented by the parameter estimation of the

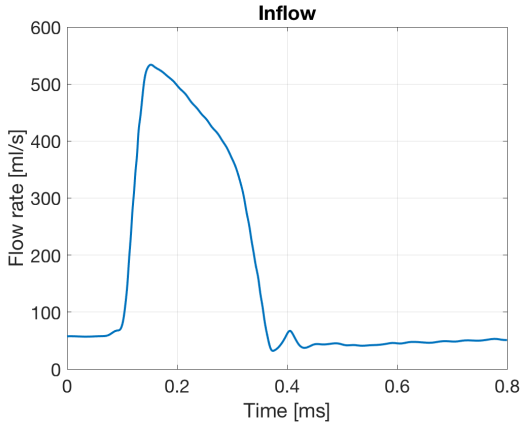

Figure 2.4: Inflow waveform taken from Westerhof et al. [6] and set at the inlet of the lumped parameter model implemented in Simulink.

peripheral resistances. Since Westerhof et al. omitted the value of the periph-

eral resistances and we have no theoretical background for a specific choice, a constant value of 25000 g cm^{-4} s^{-1} has been set empirically, in order to obtain a reliable amplitude of the pressure waveforms. We run the 0D simulation in Simulink performing 10 cardiac cycles to guarantee the repeatability of solution. Figure 2.3 on the right shows the pressure and flow rate waveforms corresponding to the ascending aorta, thoracic aorta, abdominal aorta, and femoral artery segments. The results obtained in Simulink are consistent with physiological data [24]. In particular, the pulsatile pressure is progressively attenuated by the wall elasticity of arterioles and by resistances of small arteries and arterioles, in such a way that capillary flow results stationary. The blood flow decreases from aorta to small arteries. In conclusion, this simplified model allows to reproduce reliable physiological characteristics and hemodynamic quantities with low computational cost than three-dimensional models. Moreover, the Westerhof model reproduced in Simulink could be used as a useful tool for multiscale 3D-0D simulations both in the parameter estimation of the lumped parameter model, selected as boundary condition, and as a first hemodynamic assessment (see Chapter 3).

2.3 Applications

Since 1970s, lumped parameter models have been widely treated to describe the entire cardiovascular system ([25]-[28]) or a portion of it ([29]-[31]). Burattini et al. [26] compared the behavior of two lumped parameter models, taken from literature [25], [6], representing the entire systemic arterial circulation. Authors obtained a good agreement regarding human physiology for both the models under investigation, even tough the limited number of experiments did not allow to reach a general conclusion about their validity. Canuto et al. [29] coupled 0D models of the heart, pulmonary vasculature, and peripheral vasculature to 1D models of the major systemic arteries. The multiscale model was integrated with a feedback model of the baroreflex in order to simulate the autonomic response. Kim et al. [11] implemented a lumped parameter heart model as an inflow boundary condition for 3D simulations of aortic blood flow and vessel wall dynamics. Authors proved the utility of their method by performing patient-specific simulation of an aortic coarctation.

One of the most simpler and common lumped parameter model adopted in literature is the Windkessel model.

2.3.1 0D model of peripheral circulation: the three-element Windkessel model

The Windkessel model was introduced by Otto Frank in 1899 [32] to provide a quite accurate representation of the terminal vessels. The original model includes a peripheral resistance and a compliance (see Figure 2.5), which get the following value of the impedance:

$$\zeta(\omega) = \frac{R}{1 + \sqrt{-1}\omega RC}.$$

This model was further improved with the introduction of a second resistance

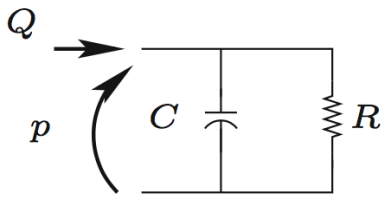

Figure 2.5: Original Windkessel model.

(see Figure 2.6), in order to better match the experimental results [6], [33]. Thus, the so called three-element Windkessel model includes two resistances,

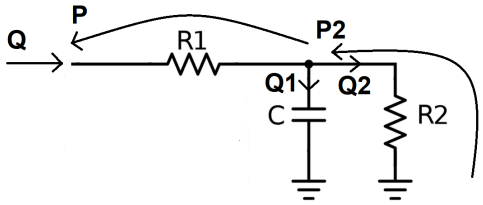

Figure 2.6: Three-element Windkessel model.

for dissipation due to viscosity of fluid motion, and a capacity, for vessel compliance. The corresponding value of the impedance is:

$$\zeta(\omega) = \frac{R_1 + R_2 + \sqrt{-1}\omega R_1 R_2 C}{1 + \sqrt{-1}\omega R_2 C}.$$

The corresponding differential system to the three-element Windkessel model

illustrated in Figure 2.6 is the following:

$$P = R_1 Q + P_2 \tag{2.3.1}$$
$$Q = Q_1 + Q_2 \tag{2.3.2}$$
$$P_2 = R_2 Q_2 \tag{2.3.3}$$
$$Q_1 = C\frac{dP_2}{dt} \tag{2.3.4}$$

Combining equations (2.3.1-2.3.3) into equation (2.3.4), this latter equation can be rewritten as:

$$Q - \frac{P_2}{R_2} = C\frac{d(P - R_1 Q)}{dt}.$$

Then, using equation (2.3.1), the proximal pressure becomes:

$$P = R_1 Q + R_2 Q - CR_2\frac{dP}{dt} + R_1 R_2 C\frac{dQ}{dt}. \tag{2.3.5}$$

Using backward Euler:

$$\frac{dP}{dt} = \frac{P_{n+1} - P_n}{\Delta t}, \qquad \frac{dQ}{dt} = \frac{Q_{n+1} - Q_n}{\Delta t},$$

into equation (2.3.5) yields to:

$$P_{n+1} = R_1 Q_{n+1} + R_2 Q_{n+1} - CR_2\frac{P_{n+1} - P_n}{\Delta t} + R_1 R_2 C\frac{Q_{n+1} - Q_n}{\Delta t}. \tag{2.3.6}$$

Rearranging the terms in the last equation (2.3.6), we obtain the following expression for the proximal pressure:

$$P_{n+1} = \frac{(R_1 + R_2 + R_1\beta)Q_{n+1} - R_1\beta Q_n + \beta P_n}{1 + \beta}, \quad \text{where } \beta = \frac{CR_2}{\Delta t}, \tag{2.3.7}$$

that can be used in numerical simulations to prescribe Neumann boundary conditions. We recall that Q_n and P_n refer to the flow and pressure, respectively, computed in the previous time-step.

2.3.2 0D model of coronary arteries

Recently, the three-elements Windkessel model is commonly used as boundary condition for the supra-aortic branches and the thoracic/abdominal outlet in CFD aortic simulations. When the 3D computational domain includes also the coronary arteries, a particular lumped parameter model could be coupled to the 3D model in order to reproduce the coronary circulation [31], [34]. In

particular, we will introduce this specific coupled 3D-0D model in Chapter 3. This coronary model consists of three resistances (R_1, R_2, R_3), two capacitances (C_1, C_2), and a voltage source (see Figure 2.7). In hydraulic analog, left ventricular pressure corresponds to the voltage source, in order to represent the intramyocardial pressure P_{im}. The corresponding differential system to the

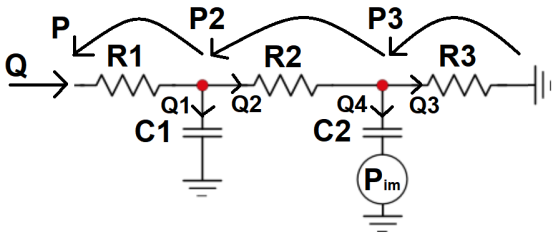

Figure 2.7: Lumped parameter coronary model.

coronary lumped parameter model is the following (see Figure 2.7):

$$P = R_1 Q + P_2 + P_3 \tag{2.3.8}$$
$$Q = Q_1 + Q_2 \tag{2.3.9}$$
$$Q_1 = C_1 \frac{d(P_2 + P_3)}{dt} \tag{2.3.10}$$
$$P_2 = R_2 Q_2 \tag{2.3.11}$$
$$Q_2 = Q_3 + Q_4 \tag{2.3.12}$$
$$Q_4 = C_2 \frac{d(P_3 - P_{im})}{dt} \tag{2.3.13}$$
$$P_3 = R_3 Q_3 \tag{2.3.14}$$

Combining equations (2.3.8), (2.3.9), (2.3.11) into equation (2.3.10), this latter equation can be rewritten as:

$$P = R_1 Q + P_3 + R_2 Q - R_2 C_1 \frac{dP}{dt} + C_1 R_1 R_2 \frac{dQ}{dt}. \tag{2.3.15}$$

Analogously, rearranging equations (2.3.8), (2.3.11), (2.3.12), (2.3.14) and substituting into equation (2.3.13):

$$R_2 Q - R_2 C_1 \frac{dP}{dt} + C_1 R_1 R_2 \frac{dQ}{dt} = \frac{R_2}{R_3} P_3 + R_2 C_2 \frac{d(P_3 - P_{im})}{dt}. \tag{2.3.16}$$

Using backward Euler:

$$\frac{dP}{dt} = \frac{P_{n+1} - P_n}{\Delta t}, \qquad \frac{dQ}{dt} = \frac{Q_{n+1} - Q_n}{\Delta t},$$
$$\frac{dP_3}{dt} = \frac{P_3^{n+1} - P_3^n}{\Delta t}, \qquad \frac{dP_{im}}{dt} = \frac{P_{im}^{n+1} - P_{im}^n}{\Delta t},$$

into equations (2.3.15), (2.3.16) yields to:

$$\begin{aligned} P_{n+1} =& R_1 Q_{n+1} + P_3^{n+1} + R_2 Q_{n+1} - R_2 C_1 \frac{P_{n+1} - P_n}{\Delta t} + \\ &+ C_1 R_1 R_2 \frac{Q_{n+1} - Q_n}{\Delta t} \end{aligned} \tag{2.3.17}$$

$$\begin{aligned} R_2 Q_{n+1} - R_2 C_1 \frac{P_{n+1} - P_n}{\Delta t} + C_1 R_1 R_2 \frac{Q_{n+1} - Q_n}{\Delta t} = \frac{R_2}{R_3} P_3^{n+1} + \\ + \frac{R_2 C_2}{\Delta t} P_3^{n+1} - \frac{R_2 C_2}{\Delta t} P_3^n - \frac{R_2 C_2}{\Delta t} P_{im}^{n+1} + \frac{R_2 C_2}{\Delta t} P_{im}^n \end{aligned} \tag{2.3.18}$$

After some algebraic manipulation, these latter equations (2.3.17), (2.3.18) become:

$$\begin{aligned} P_3^{n+1} =& \frac{\gamma}{\alpha + \gamma + \frac{\beta}{1+\beta}} P_3^n + \frac{\gamma}{\alpha + \gamma + \frac{\beta}{1+\beta}} P_{im}^{n+1} - \frac{\gamma}{\alpha + \gamma + \frac{\beta}{1+\beta}} P_{im}^n + \\ &+ \frac{1}{\alpha + \gamma + \frac{\beta}{1+\beta}} \left(\eta - \frac{\beta(R_1 + \eta)}{1+\beta} \right) Q_{n+1} + \\ &+ \frac{1}{\alpha + \gamma + \frac{\beta}{1+\beta}} \left(\frac{R_1 \beta^2}{1+\beta} - R_1 \beta \right) Q_n + \\ &+ \frac{1}{\alpha + \gamma + \frac{\beta}{1+\beta}} \left(\beta - \frac{\beta^2}{1+\beta} \right) P_n, \end{aligned} \tag{2.3.19}$$

$$P_{n+1} = \frac{\beta}{1+\beta} P_n + \frac{R_1 + R_2 + R_1 \beta}{1+\beta} Q_{n+1} - \frac{R_1 \beta}{1+\beta} Q_n + \frac{1}{1+\beta} P_3^{n+1}, \tag{2.3.20}$$

where

$$\alpha = \frac{R_2}{R_3}, \qquad \beta = \frac{R_2 C_1}{\Delta t}, \qquad \gamma = \frac{R_2 C_2}{\Delta t}, \qquad \eta = R_2 + R_1 \beta.$$

Equations (2.3.19) and (2.3.20) allow to prescribe Neumann boundary conditions at the outlets corresponding to coronary arteries.

2.3.3 3D-0D vs 0D model of thoracic aorta

In the field of aortic simulations, the refined Westerhof model implemented in Simulink could be used both as a first tool for a preliminary knowledge of the main hemodynamic features and for optimization of the parameter estimation

of the 0D models imposed as boundary conditions. For instance, we are interesting in implementing a lumped parameter model corresponding to a thoracic aorta, including the coronary arteries. We prove that the refined Westerhof model (illustrated at the center of Figure 2.8) provides reliable results comparing them to the solution of the corresponding coupled 3D-0D simulation (see the 3D-0D model in Figure 2.9). In particular, we consider the patient-

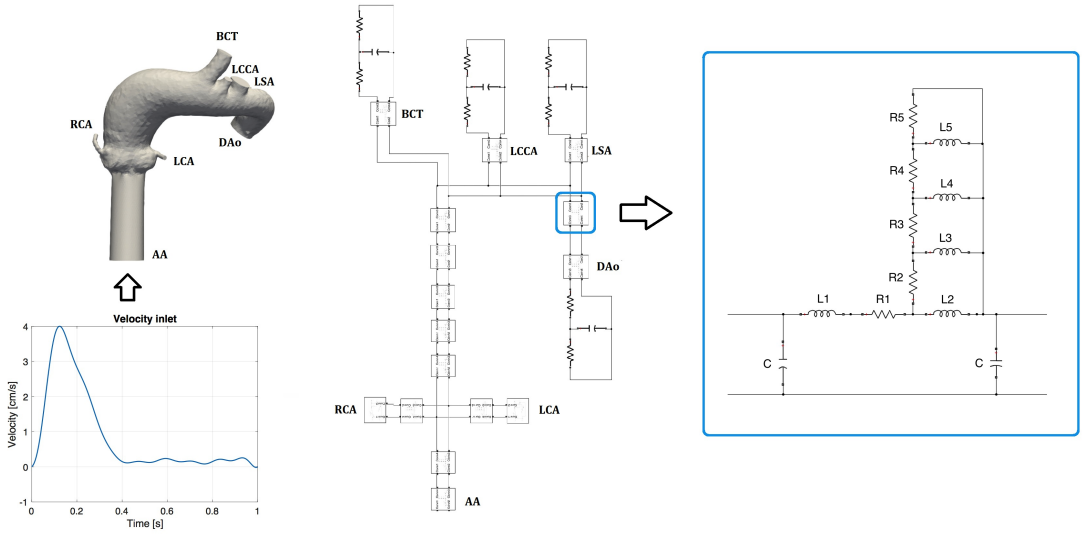

Figure 2.8: Left: computational fluid dynamics domain including a flow extension at the ascending aorta and the transient inflow wave set in the simulation. Center: lumped parameter model implementation of the pre-procedural geometry in the MATLAB toolbox Simulink. Right: electric circuit inside each block of the lumped parameter model shown in the middle. AA: ascending aorta; BCT: brachiocephalic trunk; DAo: descending aorta; LCA: left coronary artery; LCCA: left common carotid artery; LSA: left subclavian artery; RCA: right coronary artery.

specific geometry represented in Figure 2.9. We divide the 3D geometry into 14 zones, using Paraview, corresponding to the volume between the cross sections shown in Figure 2.10. In each zone the measurements of the diameter and the longitudinal length are taken in Paraview (see Figure 2.10) and used to compute the parameter values of the 0D model (see Figure 8.2 in Appendix 2), according to the equations written in (2.2.1), except for the parameter values relating to the boundary conditions. Therefore, we implement in Simulink 14 blocks corresponding to the zones selected from the 3D geometry (see Figure 2.8). Each block represents an electric network according to Westerhof et al. [6] (see Figure 2.8 on the right). The lumped parameter model described in the

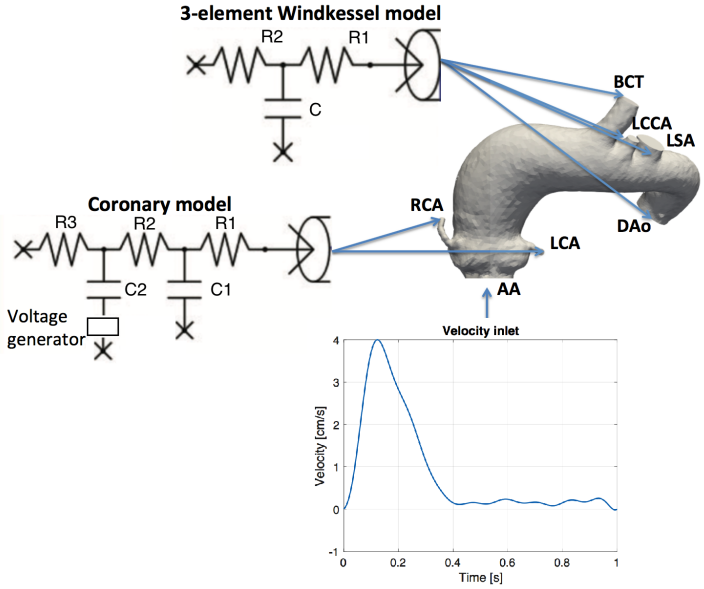

Figure 2.9: The coupled 3D-0D domain: lumped parameter models are attached to the outflow sections of the 3D computational model. Transient velocity waveform is set at the inlet.

previous section is imposed as boundary condition for the left and right coronary arteries and is included in both the blocks denoted with RCA and LCA in Figure 2.8. We maintain the same assumptions made by Westerhof et al. [6]. However, peripheral resistances were substituted by three-elements Windkessel models, used as boundary conditions for the supra-aortic branches and descending aorta (see Figure 2.8). As a preliminary test, we prescribe the inlet velocity taken from Xu et al. [18] and then rescaled (see Figure 2.8) in order to obtain a low peak Reynolds number, i.e. $Re = 424$, and avoid consequently the occurrence of numerical instabilities (see Chapter 5). The parameter values of the three-element Windkessel models (see Table 2.2) and the lumped parameter coronary model (see Table 2.3) are taken from Xu et al. [18] and Conti et al. [31], respectively. Blood is assumed as an incompressible and Newtonian fluid, with 1060 kg/m^3 density and 0.0035 Pa s viscosity [35]. We perform two simulations, one using the lumped parameter model implemented in Simulink and the other one the coupled 3D-0D model written in the open source software Fenics. In the coupled 3D-0D model, the 0D model corresponds to the boundary conditions prescribed at the outlets, i.e. three-elements Windkessel model at the supra-aortic branches and descending aorta, and the lumped coronary artery model at the left and right coronary arteries (see Figure 2.9). The equations (2.3.7) and (2.3.19)-(2.3.20), derived in the previous section, were used

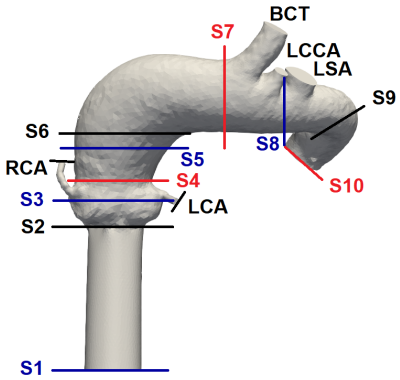

Zone	Length (cm)	Diameter (cm)
S1-S2	7.137	2.690
S2-S3	1.320	3.367
S3-S4	1.233	3.858
S4-S5	3.256	4.106
S5-S6	2.426	4.178
S6-S7	4.964	3.572
S7-S8	2.127	2.948
S8-S9	4.021	2.353
S9-S10	1.919	2.130
BCT	1.919	1.188
LCCA	0.655	0.638
LSA	0.599	1.450
RCA	1.900	0.336
LCA	1.112	0.334

Figure 2.10: Left: computational fluid dynamics domain divided into 14 zones, i.e. the regions between the cross sections $S_1, ..., S_{10}$ and the zones corresponding to the brachiocephalic trunk (BCT), left common carotid artery (LCCA), left common carotid artery (LSA), left coronary artery (LCA), and right coronary artery (RCA). Right: measure of the length and averaged diameter of each zone in which the aorta is divided.

to impose the boundary conditions at the outlets in Fenics. The parameter values involved in the 3D-0D simulation are the same of the 0D simulation, reported in Tables 2.2 and 2.3. A constant time-step size is set to 0.001 ms and 0.001 s in the 0D and 3D-0D simulation, respectively, since the Westerhof model operates at one thousand the real frequency. Six cardiac cycles were performed in both the simulations to guarantee the repeatability of solution.

We compare the flow rate and pressure waveforms at the outlets obtained from Simulink and Fenics. Figure 2.11 shows the flow rate and pressure waveforms at the supra-aortic branches and descending aorta. Figure 2.12 illustrates the flow rate and pressure waveforms at the left and right coronary arteries. We can note a good agreement with the results of the two models. In both the models, the left coronary flow rate waveform has a first peak during the early systole, then decreases to raise up again towards a second higher peak in diastole (see Figure 2.12), because the intramyocardial pressure is elevated in systole. Vice-versa, right coronary flow is higher in systole and lower in diastole, according to literature data [36]. However, we recall that all the values of

	R_1	R_2	C
BCT	0.78	2.03	0.93
LCCA	3.80	4.50	0.34
LSA	1.39	3.20	0.58
DAo	0.13	0.15	10.90

Table 2.2: Windkessel parameters taken from Xu et al. [18]. The unit of R_1 and R_2 values are in 10^3 g cm^{-4} s^{-1} and the unit of C values are in 10^{-7} g^{-1} cm^4 s^2. AA: ascending aorta; BCT: brachiocephalic trunk; LCCA: left common carotid artery; LSA: left subclavian artery; DAo: descending aorta.

	R_1	R_2	R_3	C_1	C_2
RCA	38.798	63.045	193.98	0.028	0.223
LCA	16.899	27.462	8.450	0.030	0.220

Table 2.3: Parameter values of the lumped parameter model of the coronary outlets. The unit of the resistance values are in 10^3 g cm^{-4} s^{-1} and the unit of the capacitance values are in 10^{-7} g^{-1} cm^4 s^2. RCA: right coronary artery; LCA: left coronary artery.

pressure and flow rate of the two models are not physiological, since we have considered lower values in the prescribed inflow than the physiological one, in order to avoid numerical instabilities. An acceptable mismatch is shown in both the Figures 2.11 and 2.12 in the amplitude of the curves. In particular, the amplitude of the waveforms given from Simulink appears slightly greater than the one obtained from Fenics. Possible reasons of this mismatch could be errors introduced during the measurements of the diameter and the longitudinal length of each zone in which the geometry is subdivided, and approximations assumed in the 0D model (i.e. considering the computational domain divided into a finite number of compartments is also an approximation). Moreover, while in Simulink we impose the flow rate at inlet, as the result of the same inlet velocity, used for the 3D-0D simulation, times the inlet area computed in Paraview from the 3D geometry, in the 3D-0D simulation all the flow rate curves depend on the mesh size.

The qualitative comparison between the results of 0D and 3D-0D models proved the consistency of the 0D model. Indeed, the lumped parameter model provides reliable results by both an accurate selection of the various segments, in which the original 3D computational domain should be divided, and a proper parameter estimations.

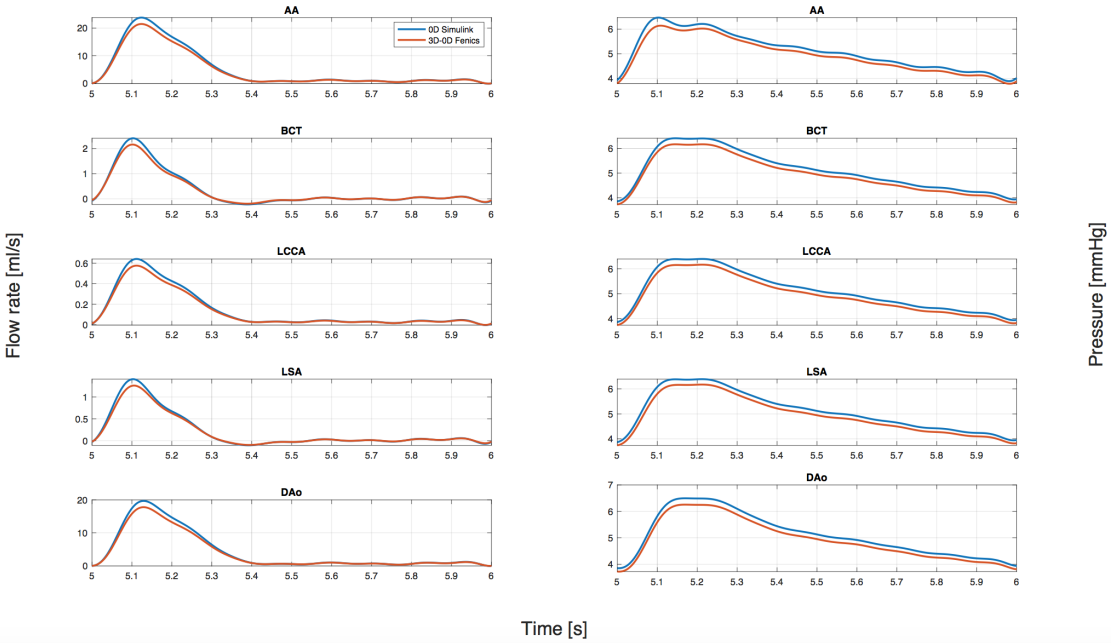

Figure 2.11: Results of 0D (in blue) and coupled 3D-0D (in red) simulations. The flow rate and pressure waveforms refer to the sixth cardiac cycle. AA: ascending aorta; BCT: brachiocephalic trunk; LCCA: left common carotid artery; LSA: left subclavian artery; DAo: descending aorta.

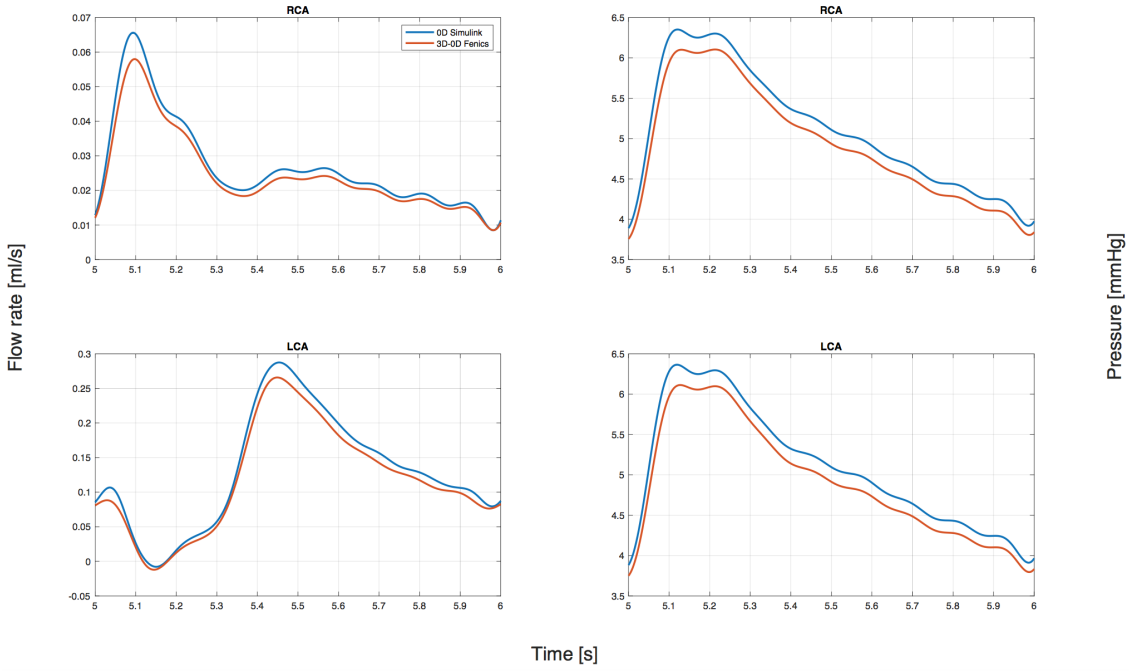

Figure 2.12: Results of 0D (in blue) and coupled 3D-0D (in red) simulations. The flow rate and pressure waveforms refer to the sixth cardiac cycle. RCA: right coronary artery; LCA: left coronary artery.

Chapter 3

3D-0D Models of Thoracic Aorta

In this Chapter, we analyze a particular coupled 3D-0D model of diseased thoracic aorta treated with transcatheter aortic root repair (TARR) [31]. The aim is to set-up a computational model of TARR in order to explore the impact of the endovascular procedure on the coronary circulation, supported by chimney grafts.

3.1 Case Study: Patient-specific Aorta Including Coronary Arteries

Transcatheter aortic valve replacement (TAVR) is a consolidated alternative to surgical aortic valve replacement for high-risk patients, valve-in-valve procedures and, recently, also for low-risk patients [37], while transcatheter endovascular arch replacement, supported by the development of new devices featuring chimneys, branches, etc. [38], is performed in very few cases, mostly when surgical treatment is highly risky [39].

In many cases, such as the presence of a degenerated bicuspid aortic valve, there is a need of replacing both the native valve and the ascending aorta, which is often dilated increasing the risk of rupture or dissection [40]. As stated earlier, both alternatives are available as separate endovascular treatments, but a transcatheter device that includes a combined replacement of the aortic valve, the root and the ascending aorta has not yet been proposed. Some of the challenges of such a procedure are the high pulsatility of the ascending portion of the aorta, its angulated anatomy and the need to keep the coronary perfusion.

Recent studies showed a high level of success of off-label use of endovascular devices in the treatment of ascending aortic diseases [41]. However, the outcome of endovascular repair can also be evaluated through virtual simulation tech-

niques. As an example, Romarowski et al. [42] proved that tailor-made devices performed much better than off-the-shelf endoprosthesis that were adapted for their use in the ascending aorta. However, these studies remained limited to the repair of the ascending aorta and did not include the replacement of the aortic root. To the best of our knowledge, only two studies have analysed the simultaneous endovascular repair of ascending aorta and aortic root. Gaia et al. [43] described the endovascular management of a patient that was considered inoperable after conventional aortic valve replacement. A customized stent attached to a transcatheter valve was deployed, thus being the first-in-human case of what they called, the *Endo-Bentall procedure*. The patient did not have any sign of myocardial infarction at a 4-month follow-up. Previous work of our group presented a preliminary test of a TARR [44] using computed tomography (CT) scan-derived 3-dimensional (3D) printed root model [45] (Figure 3.1). In particular, the authors proposed the feasibility of using chimney grafts as a way to perfuse the coronary ostia in a very simplified haemodynamic model. Given such encouraging outcomes, the goal of the present study is to set-up a proof-of-concept computational model of TARR to explore the impact of the endovascular procedure on the coronary circulation. To this aim, a patient-specific model of an aneurysmatic ascending aorta including the coronary ostia is derived from CT angiography. Computational fluid dynamics (CFD) simulation of the preprocedural cardiovascular model is performed to define a reference for the evaluation of post-procedural configuration obtained by the simulation of the TARR procedure.

Figure 3.1: In vitro deployment of a device combining an ascending aorta endograft with a temporary valve and 2 coronary chimney grafts. Left: sketch of the considered device. Right: deployment within a 3-dimensional printed model (patient-specific aortic root).

3.1.1 Medical imaging analysis and processing

CT images of a patient with dilated aortic root and ascending aorta were used for this study and informed consent for use of anonymized data was provided. A patient-specific 3D model of the preprocedural ascending aorta was obtained by image segmentation of contrast-enhanced CT scan. The model included the aortic root, coronary ostia, aortic arch and epiaortic branches (Figure 3.2 a)). The segmentation was performed using the open-source software ITK-Snap (`http://www.itksnap.org`).

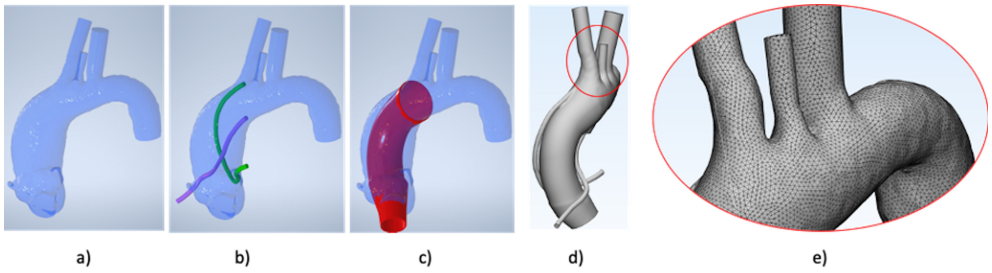

Figure 3.2: Three-dimensional model of the aortic root, ascending aorta and aortic arch. a) Pre-procedural model as derived from medical image segmentation; b) CAD elaboration to insert coronary chimney grafts; c) CAD elaboration to insert aortic endograft; d) final CAD post-procedural transcatheter aortic root repair model including the main endograft and the chimney grafts; e) computational grid (mesh) for computational fluid dynamics analysis, the image depicts the mesh in the zone of the model highlighted in d). CAD: computer-aided design.

3.1.2 TARR procedure and post-procedural aortic model

The proposed TARR procedure described in our previous work [44] implies the transcatheter deployment of one main endograft within the aortic root (28 mm diameter) and two 6-mm-diameter 10-cm-long coronary chimney grafts. The main graft features a temporary non-biologic aortic valve at its proximal side that impedes ventricular dilatation after the deployment. After completion of the TARR procedure, a commercially available low- profile TAVR valve is inserted in the main graft at the level of the temporary aortic valve.

Given these indications, we have modified the preprocedural reconstruction of the vascular model to include these devices using computer-aided design (CAD) software (Autodesk Inventor Professional 2017). For this study, the temporary aortic valve was not included in the computational model.

The model of the root endograft was drawn on the base of the aortic centreline extracted by the VMTK library (`http://www.vmtk.org`). In particular, the aortic centreline was used to mimic the longitudinal axis of the endograft, while various planes normal to the centreline were used in the lofting to define the cross sectional profile of the endograft. The first of these planes was placed at the level of the left ventricular outflow tract. The downstream planes were placed following the orientation imposed by the aortic centreline up to the end of the ascending aorta, immediately before the ostium of the brachiocephalic trunk. Using section lofting, the cylindrical solid model of the root endograft with a thickness of 1 mm was created; this model is tapered with a proximal diameter of 22 mm at the left ventricular outflow tract and a distal diameter of 36 mm at the end of the ascending aorta.

Similarly, the models of the coronary chimney grafts were drawn: (i) the intra-coronary part is sketched by inserting a flow extension (15 mm length) of the native coronary ostia to let the flow develop and avoid boundary effects from the numerical simulation [46] (Figure 3.2 b)) and (ii) the path of each graft inside the aortic root and ascending aorta were designed based on the visual inspection of the in vitro model proposed in Ferrari et al. [44] (Figure 3.2 c)). The 3D preoperative model of the aorta, the CAD model of the root endograft and the 2 models of the coronary chimney grafts were merged using CAD Boolean operations with Netfabb software (Autodesk, San Rafael, CA, USA) (Figure 3.2 d)); the resulting model describes the luminal surface of the post-TARR aorta and it was used to create a computational grid suitable for CFD as shown in Figure 3.2 e)).

3.1.3 Computational fluid dynamics analysis

CFD simulations were performed in both pre- and post- procedural geometries using the solver SimVascular [47] in a computing node with 2 Intel Xeon Gold 6148 processors and 192 GB di RAM totalizing 40 cores. Meshes were also created in SimVascular with an element length based on the local radius. As a result, the preoperative mesh featured 1.8M elements whereas the post-procedural mesh had 2.7M elements accounting for the radius-based meshing technique. Blood flow was considered laminar, homogeneous and Newtonian with a density of 1060 kg/m^3 and a viscosity of 0.0035 $Pa\ s$. Given the lack of patient-specific boundary flow conditions, we used a pulsatile inflow wave extracted from Xu et al. [18] at the origin of the ascending aorta featuring a duration of 1 s each heart cycle discretized into 1000 time-steps. Such a pulsatile blood flow, with a peak in systole and almost no flow in diastole, imitates the inflow behaviour right after the aortic valve.

The goal of our study requires particular attention to the modelling of the

coronary circulation. For this reason, we have adopted a 3D-0D modelling approach (Figure 3.3) where the 3-dimensional domain of the aorta is coupled with 0D models accounting for the peripheral circulation at the outlets of the supra-aortic branches, the descending aorta, and the coronary circulation. In

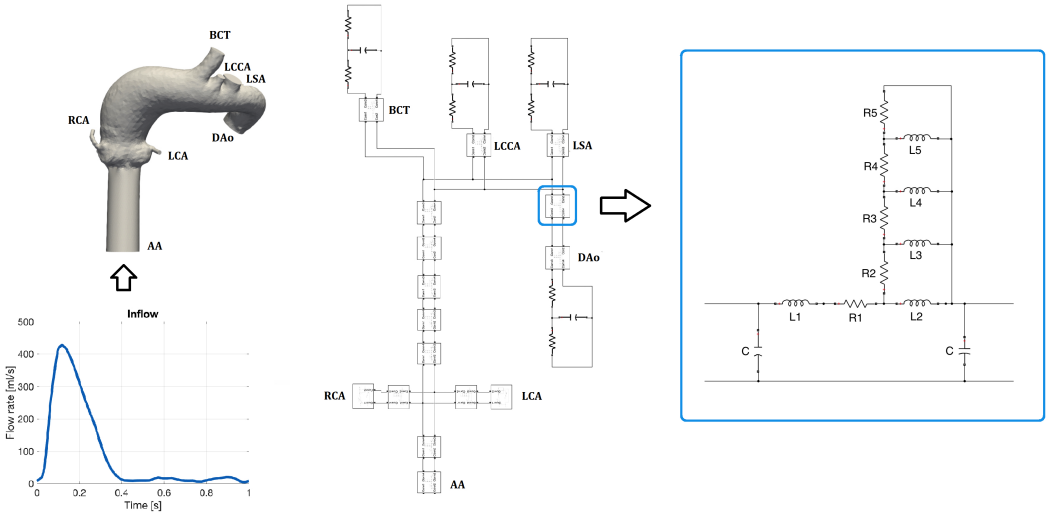

Figure 3.3: Left: computational fluid dynamics domain including a flow extension at the ascending aorta and the transient inflow wave set in the simulations taken from Xu et al. [18]. Center: lumped parameter model implementation of the pre-procedural geometry in the MATLAB toolbox Simulink. Right: electric circuit inside each block of the lumped parameter model shown in the middle. AA: ascending aorta; BCT: brachiocephalic trunk; DAo: descending aorta; LCA: left coronary artery; LCCA: left common carotid artery; LSA: left subclavian artery; RCA: right coronary artery.

the supra-aortic vessels and the descending aortic outlet, three-element Windkessel lumped circuits were attached to mimic the downstream vasculature [18]. In the coronary outlets, a lumped parameter model was used following the work by Sankaran et al. [48]. The details of parameter estimation are described in the next section.

3.1.4 Parameter Estimation for Lumped-parameter Models

As we mentioned before, we are using a coupled 3D-0D model, in which the three-dimensional domain is represented by the aorta, while the surrogate

0D model (or lumped-parameter model) accounts for the peripheral circulation at the aortic outlets (i.e., supra-aortic branches and the descending aorta) and the coronary circulation. In particular, we adopted a three-element Windkessel model to simulate the downstream circulation at the aortic outlets and a lumped-parameter model, including four resistances and two capacitances to model the coronary circulation.

A critical step when using such surrogate models is the calibration of the parameters. Regarding the three-element Windkessel model, many calibration procedures have been widely dealt with in literature [46], [49], while for the coronary model less studies are present. In particular, the main challenge in the calibration of 0D models for coronary circulation consists in modeling the out-of-phase nature of coronary flow due to the influence of ventricular contraction. Recently, lumped-parameter models have been used to simulate the coronary flow [48], [50]; however, to the best of our knowledge, there is no study in the literature that systematically addresses the procedure for estimating the parameters of lumped vascular models when the coronary circulation and the part of the peripheral aortic circulation are both present, as in our case.

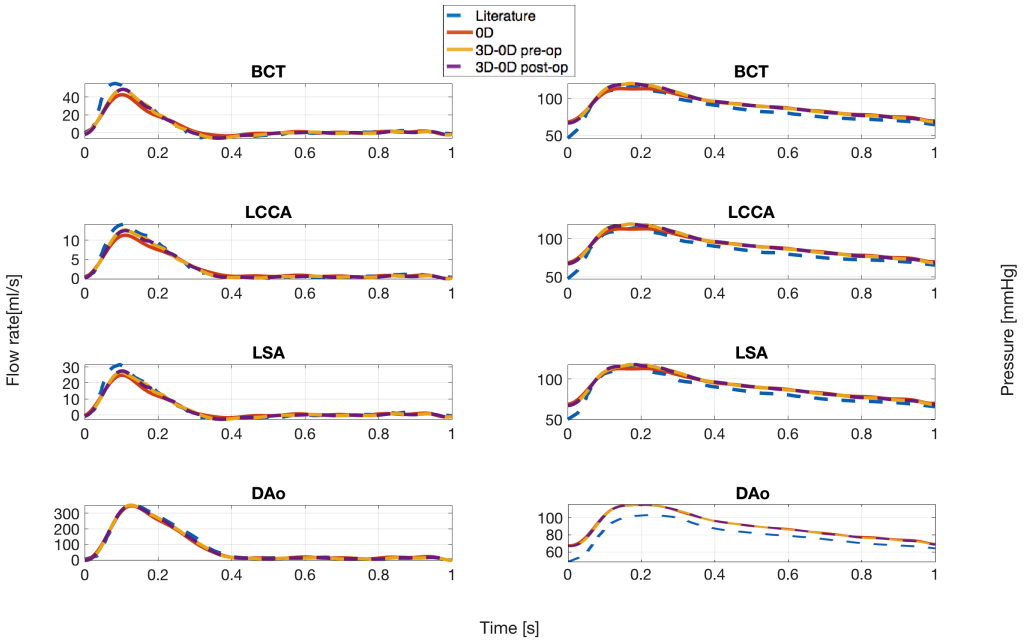

Figure 3.4: Comparison between flow and pressure waveforms taken from literature [18] (3D-0D model), computed in Simulink (0D model), and in SimVascular (3D-0D model) for both pre- and post-procedural TARR configuration. Brachiocephalic Trunk (BCT); Left Common Carotid Artery (LCCA); Left Subclavian Artery (LSA); Descending Aorta (DAo).

We have faced this problem using a lumped-parameter model representing the coronary circulation and also the aorta in order to calibrate the whole parameter set without the need of simulating the 3D aortic domain during this phase. The parameters estimated by this 0D representation have been used later in our 3D-0D model and the consistency with the two models has been proved in Figures 3.4 and 3.5.

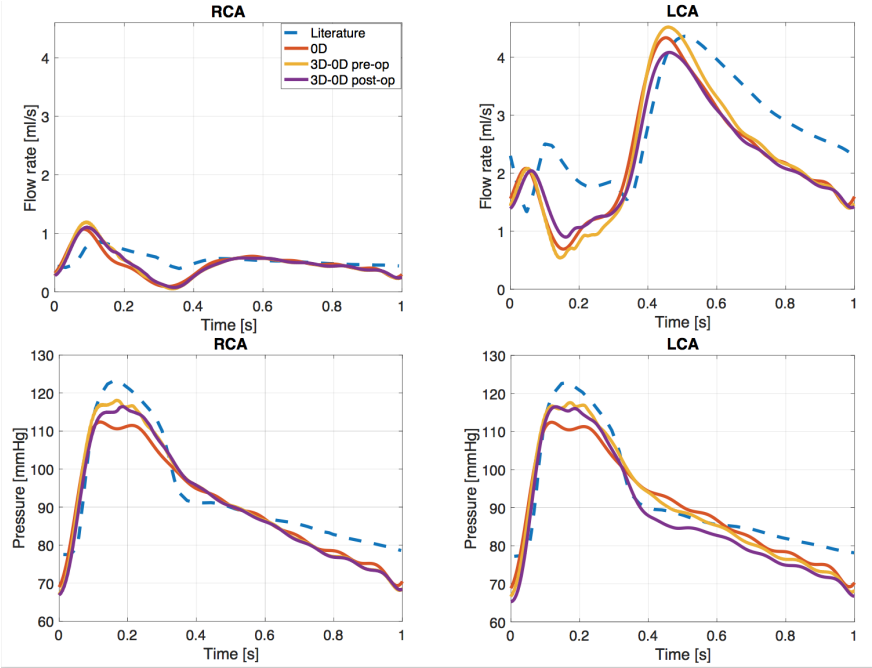

Figure 3.5: Comparison between coronary flow and pressure waveforms taken from literature [11] (3D-0D model), computed in Simulink (0D model), and in SimVascular (3D-0D model) for both pre- and post-procedural TARR configuration. Right Coronary Artery (RCA); Left Coronary Artery (LCA).

The 0D model was implemented in the Matlab toolbox Simulink R2018a (The MathWorks, Natick, MA, USA). Each cylindrical segment includes a finite number of resistances, inductances, and capacitances, which values are computed according to the Westerhof et al. [6]. In particular, our lumped-parameter model is obtained by dividing the geometry into 16 segments, and then adding three-element Windkessel models as boundary conditions on the supra-aortic and descending aorta outlets (Figure 3.2); the values of the parameters for such models are set according to Xu et al. [18].

The lumped parameter model associated to the boundary conditions on the coronary arteries, consists of four resistances (i.e., coronary arterial resistance R_a, coronary arterial microcirculation resistance $R_{a-micro}$, coronary

venous microcirculation resistance $R_{v-micro}$, coronary venous resistance R_v), two capacitances (i.e., coronary arterial compliance C_a and myocardial compliance C_{im}) and intramyocardial pressure $P_{im}(t)$, as described in Kim et al. [11]. Left ventricular pressure is used to represent the intramyocardial pressure.

We compute the values of the resistances and compliances according to Sankaran et al. [48]. In particular, the estimation procedure can be summarized as follows:

1. Calculation of total resistance R_{tot} for all the outlets according to the following relation
$$R_{tot} = \frac{P_{mean}}{Q} \tag{3.1.1}$$
where P_{mean} and Q are known and denote the mean pressure and the cardiac output, respectively.

2. Prescription of the average flow split between the coronaries and the aorta
$$Q_{cor} = \beta Q_{br} \tag{3.1.2}$$
assuming $\beta = 0.04$ [48], denoting by Q_{cor} the coronary flow, and by Q_{br} the systemic flow in the remaining outlets.

3. Recalling
$$\frac{1}{R_{tot}} = \frac{1}{R_{cor}} + \frac{1}{R_{br}} \tag{3.1.3}$$
and using equation (3.1.2), the coronary resistance is
$$R_{cor} = \frac{1+\beta}{\beta} R_{tot} \tag{3.1.4}$$

4. Flow splitting between left and right coronaries
$$Q_{cor}^{left} = \gamma Q_{cor}^{right} \tag{3.1.5}$$
considering the flow split $\gamma = 7/3$ [48] (i.e., 70-30% flow split between the left and right coronary artery [51]).

5. Using equation (3.1.5), the left and right coronary arteries resistances are respectively
$$R_{cor}^{left} = \frac{1+\gamma}{\gamma} R_{cor} \tag{3.1.6}$$
$$R_{cor}^{right} = (1+\gamma) R_{cor} \tag{3.1.7}$$

6. Recalling that for both left and right coronary resistances and dealing only with the left one, for the sake of simplicity,

$$R_{cor}^{left} = R_a + R_{a-micro} + R_{v-micro} + R_v \tag{3.1.8}$$

we choose

$$R_a = 0.32 R_{cor}^{left} \tag{3.1.9}$$
$$R_{a-micro} = 0.52 R_{cor}^{left} \tag{3.1.10}$$
$$R_{v-micro} + R_v = 0.16 R_{cor}^{left} \tag{3.1.11}$$

according to Sankaran et al. [48].

7. Calculation of the left coronary compliances

$$C_a = 0.11 C_{cor}^{left} \tag{3.1.12}$$
$$C_{im} = 0.89 C_{cor}^{left} \tag{3.1.13}$$

prescribing the total coronary compliance $C_{cor}^{tot} = C_{cor}^{left} + C_{cor}^{right}$ and recalling that $C_{cor}^{left} = C_a + C_{im}$, $C_{cor}^{right} = C_a + C_{im}$. We compute analogously the right coronary compliances, assuming the total left coronary compliance $C_{cor}^{left} = 3.6\ 10^{-5} cm^5/dyne$ and the total right coronary compliance $C_{cor}^{right} = 2.5\ 10^{-5} cm^5/dyne$, according to Wilson et al. [52].

The computed parameter values are listed in Table 2.3, where R_a, $R_{a-micro}$, and $(R_v + R_{v-micro})$ have been renamed with R_1, R_2 and R_3, respectively, and analogously C_a and C_{im} with C_1 and C_2, respectively. The resistance value $R_{v-micro} + R_v$ was tuned to achieve physiological coronary flow waveforms according to literature data [50].

We simulated six cardiac cycles to achieve periodic solutions; analogously to the multiscale model implemented in SimVascular, the viscosity and the density of blood are assumed to be 0.0035 Pa/s and 1060 kg/m^3, respectively.

In these simulations, we study flow rate and pressure waveforms at the outlets. The aim is to prove that flow rate and pressure waveforms on the boundaries given by the lumped-parameter model are physiologic and consistent with the results obtained by the coupling of 3D-0D model, and with data taken by literature. We report herein the results related only to the sixth cardiac cycle to ensure the convergence of the numerical simulation (Romarowski et al. [46]).

Figure 3.4 shows comparison between flow rate and pressure curves at the supra-aortic vessels outlet and descending aorta in the simulations performed in Simulink with 0D model, in SimVascular with 3D-0D model (for both pre-

and post-procedural configuration), and with 3D-0D model taken by Xu et al. [18].

All the computed waveforms are realistic; we can note a negligible difference between the curves in Xu et al. [18] and the results obtained using the proposed models due to the different computational domain: indeed, the lumped-parameter model has been built tuning the parameter values in order to represent the patient-specific three-dimensional domain used in the simulations performed in SimVascular (Figure 3.2). Figure 3.5 represents comparison between flow rate and pressure curves at the coronary outlets in the simulations performed in Simulink with 0D model, in SimVascular with 3D-0D model (for both pre- and post-procedural configuration), and with 3D-0D model taken by Kim et al. [50].

In each model, the left coronary flow rate curve has a first peak during the early systole, then decreases to raise up again towards a second higher peak in diastole, because the intramyocardial pressure is elevated in systole; vice-versa, right coronary flow is higher in systole and lower in diastole, according to literature data [36]. The total coronary flow represents a 3% of the cardiac output, according to Nauta et al. [53]; in particular, the left coronary and right flow represent the 83% and 17% of total coronary flow, respectively. This result deviates from the prescribed 70/30 flow split due to fine tuning of resistance value $R_{v-micro} + R_v$.

The curves obtained by the proposed models (full 0D and 3D-0D) are close to each other, consequently we were able to obtain realistic coronary flow and pressure waveforms with the lumped-parameter model implemented in Simulink and a consistent outcome with those performed using the coupling of 3D-0D models in SimVascular.

However, our results showed an acceptable mismatch with the data reported by Kim et al. [50]; such a difference can be related to the inflow rate used as boundary conditions, since we have implemented the inflow curve proposed by Xu et al. [18].

3.1.5 Post-processing

Five instants of the last cardiac cycle were considered from the inflow curve: the beginning of the systole ($t = 0s$), maximum systolic acceleration ($t = 0.06s$), systolic peak ($t = 0.18s$), maximum systolic deceleration ($t = 0.32s$) and beginning of diastole ($t = 0.4s$). The velocity field along the aorta was analysed by inspecting the streamlines using Paraview 5.8.0 (Kitware Inc., Clifton Park, NY, rates at all the outlets were compared between the pre- and post-procedural simulations, as well as coronary flow, split to quantify the differences caused by the intervention. Qualitative and quantita-

tive analyses of the bulk flow were treated in both pre- and post-procedural configuration. We expect that the TARR procedure to maintain the same bulk flow features of the preprocedural configuration. Qualitatively, we compute the local normalized helicity (LNH), which corresponds to the cosine of the angle formed between the vorticity vector and the velocity vector. It is a measure of the alignment/misalignment of the local velocity and vorticity vectors. It ranges from -1 to 1 and its sign is useful to understand the direction of helical structures. Quantitatively, we compute the h_2 helicity index, which is a bulk flow descriptor given by time-averaging the absolute value of the helicity [101], i.e.:

$$h_2 = \frac{1}{TV} \int_T \int_V |\mathbf{u} \cdot (\nabla \times \mathbf{u})| \, dV dt. \tag{3.1.14}$$

The h_2 helicity index denotes the helicity intensity in the fluid domain. Recalling that the helicity is defined by the spatial integral of the scalar product of the velocity and vorticity, the h_2 index assumes major values in the fluid domain in which velocity and vorticity vectors are aligned. The h_2 index was computed by integration over 3 volumetric fluid domains, i.e. the segment of the right coronary artery, the segment of left coronary artery (LCA) and the whole fluid domain.

Finally, as an indicator of the influence of the chimney grafts in the coronary blood supply, we estimated the pressure drop from the origin of the aorta (i.e. aortic annulus) to the distal section of the coronaries. There is also an acceleration during the systole as compared to the preprocedural geometry that can be attributed to the narrowing in the lumen caused by the new endoprosthesis. Figure 3.6 also reports a jump of 4 mmHg in the ascending aorta pressure after the TARR procedure which can also be a consequence of the presence of the endograft.

3.1.6 Numerical Results

Figure 3.7 illustrates the streamlines along the aorta during the selected five instants in both preprocedural and post-procedural TARR configuration. The major difference after the intervention is seen during t_1 and t_2 in the ascending portion of the aorta. Flow becomes more organized and less recirculation is seen at the point where the aneurysm was present.

There is also an acceleration during the systole as compared to the preprocedural geometry that can be attributed to the narrowing in the lumen caused by the new endoprosthesis. Figure 3.6 also reports a jump of 4 mmHg in the ascending aorta pressure after the TARR procedure which can also be a consequence of the presence of the endograft.

	*t*0	*t*1	*t*2	*t*3	*t*4
Pre-procedural					
P (mmHg)					
AA	66.95	95.73	117.35	103.38	96.08
RCA	67.36	95.22	117.22	103.33	95.66
LCA	67.01	95.29	117.16	102.96	93.96
Δ*P* (mmHg)					
RCA-AA	-0.42	0.50	0.13	0.06	0.42
LCA-AA	-0.07	0.44	0.18	0.42	2.13
Post-procedural (TARR system simulation)					
P (mmHg)					
AA	67.10	100.19	114.96	101.83	95.97
RCA	67.05	91.90	116.29	103.76	95.63
LCA	65.32	91.21	115.93	100.94	87.83
Δ*P* (mmHg)					
RCA-AA	0.05	8.29	-1.33	-1.94	0.33
LCA-AA	1.78	8.98	-0.97	0.89	8.13

Figure 3.6: Pressure at the selected 5 instants along the cardiac cycles in the AA and coronary outlets together with the pressure jump between points. AA: ascending aorta; LCA: left coronary artery; RCA: right coronary artery; TARR: transcatheter aortic root repair.

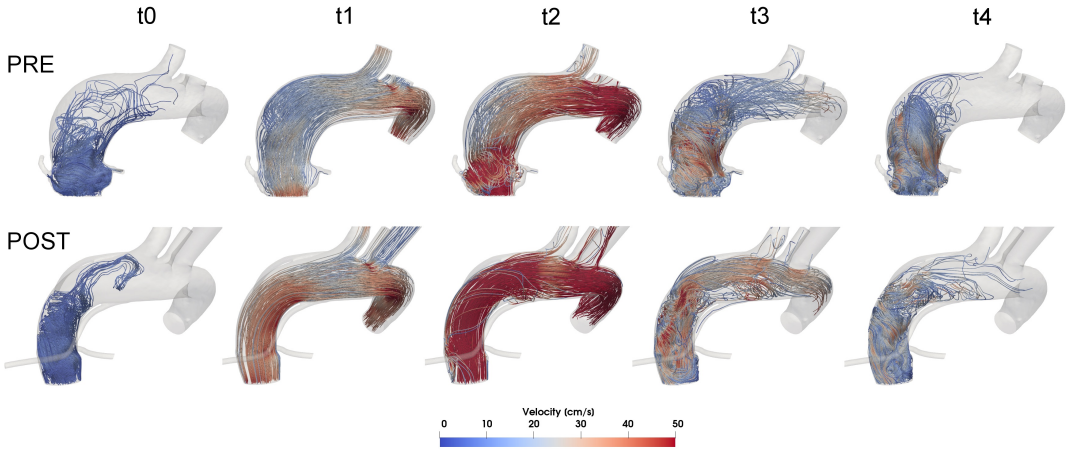

Figure 3.7: Results of computational fluid dynamics simulations. Streamlines of pre- and post-procedural transcatheter aortic root repair configurations along the selected 5 instants of cardiac cycle. The source of the streamlines is located at the aortic annulus.

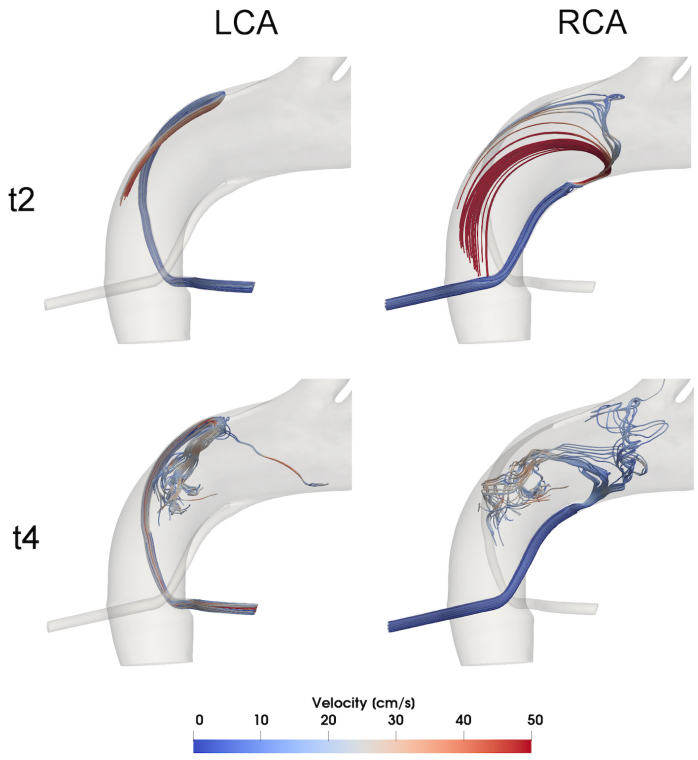

Figure 3.8: Results of computational fluid dynamics simulations. Streamlines of post-procedural configuration at systolic peak (t_2) and early diastole (t_4). The source of the streamlines is located at the outflow sections of the RCA and LCA in order to highlight the pattern of the coronary flow LCA: left coronary artery; RCA: right coronary artery.

Figure 3.8 depicts the velocity streamlines at t_2 and t_4 inside the coronary arteries after the procedure. We can observe that there are no recirculation zones at the connection to the body of the main graft. In Figure 3.9, the superposition of the flow waves in the supra-aortic vessels as well as the coronaries is shown. Negligible differences are present in the brachiocephalic trunk, left common carotid artery, left subclavian artery and descending aorta, ensuring that the systemic circulation has not been compromised with the implantation of the TARR devices.

Differences in the output flow in the coronary arteries showed negligible differences as reported in Figure 3.9. The inlet aortic flow rate was 5.43 l/min and was kept equal for both pre- and post-procedural TARR simulations. In the preprocedural configuration, the right coronary artery flow rate was 28.93 ml/min (corresponding to the 0.53% of the total aortic inflow) while the LCA

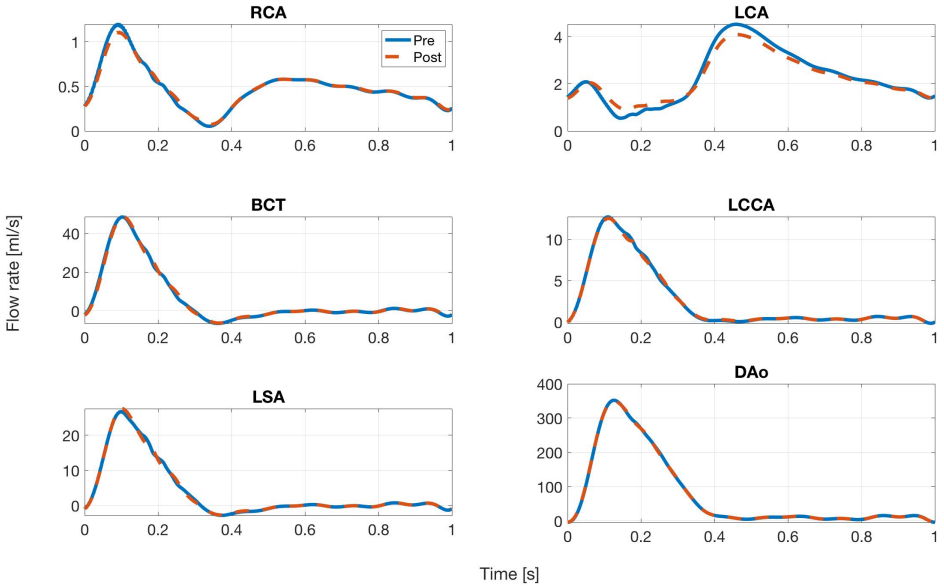

Figure 3.9: Results of computational fluid dynamics simulations. The flow rate curves at the model outlets along the cardiac cycle are reported for pre- and post-procedural transcatheter aortic root repair configurations. BCT: brachiocephalic trunk; DAo: descending aorta; LCA: left coronary artery; LCCA: left common carotid artery; LSA: left subclavian artery; RCA: right coronary artery.

flow rate was 136.94 ml/min (which correspond to the 2.52% of the total aortic inflow), totalizing a coronary supply of 3.05% of the aortic inflow. After the virtual TARR procedure, there was a very limited decrease in coronary flow circulation corresponding to RCA flow: 0.53%, LCA flow: 2.45% and a total coronary flow: 2.98% of the aortic inflow.

Regarding the bulk flow, Figure 3.10 represents helical structures given by considering LNH values with a threshold of ±0.8. The LNH was computed at the systolic peak (t_2), at maximum systolic deceleration (t_3) and beginning of diastole (t_4). The h_2 values computed in the total volume of both the configurations ($h_2^{PRE} = 5.1$ m/s^2 and $h_2^{POST} = 7.6$ m/s^2, where h_2^{PRE} and h_2^{POST} denote the values of h_2 computed in the pre- and post-procedural configuration, respectively) are in good agreement with the values reported by Morbiducci et al. [54]. Despite the value of h_2 related to the total volume is very similar in both the pre- and post-procedural configurations, significant differences characterize the coronary arteries, in particular the h_2 values related to the LCA ($h_2^{PRE,RC} = 1.3\ m/s^2$, $h_2^{POST,RC} = 0.052\ m/s^2$, $h_2^{PRE,LC} = 24.0\ m/s^2$,

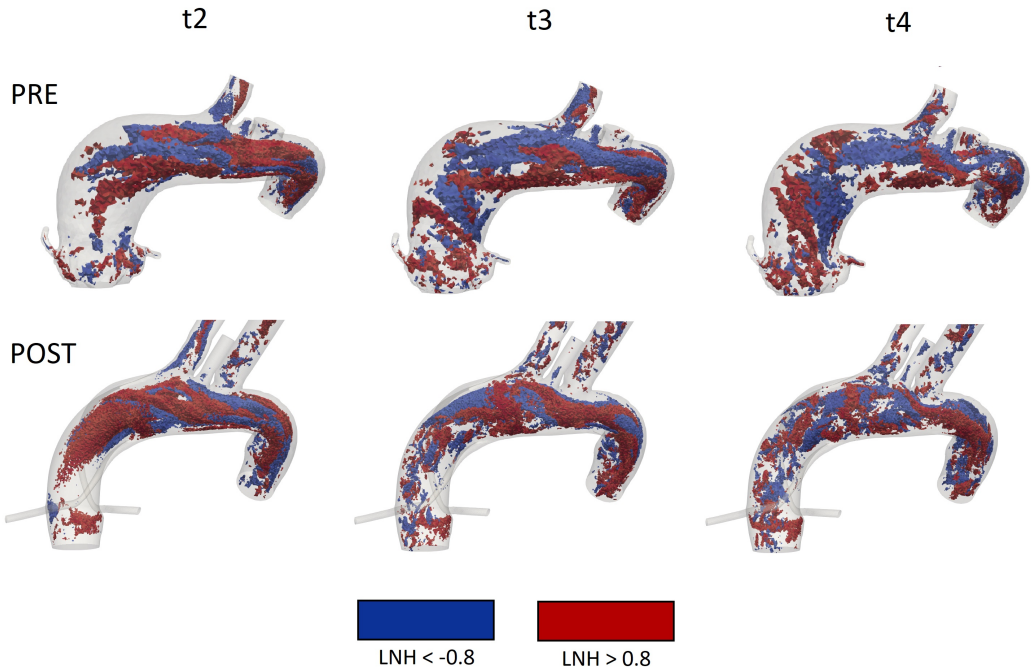

Figure 3.10: Results of computational fluid dynamics simulations. Isosurfaces of high threshold values of LNH (± 0.8) at systolic peak (t_2), maximum deceleration (t_3) and early diastole (t_4), in pre- and post-procedural configurations. LNH: local normalized helicity.

$h^{POST,LC} = 6.8\ m/s^2$, where $h_2^{PRE,RC}$ and $h_2^{POST,RC}$ denote the values of h_2 computed in the right coronary arteries in the pre- and post-procedural configuration, respectively, and $h_2^{PRE,LC}$ and $h_2^{POST,LC}$ are the values of h_2 computed in the left coronary arteries in the pre- and post-procedural configuration, respectively).

In Figure 3.6 we have reported the differences in pressure values between the coronary ostia (either the native ostia in the preprocedural geometry or the distal section of the graft in the post-procedural TARR model) and the aortic inflow section. The highest difference in the pressure jumps was found during t_1 of the post-procedural configuration, where both coronaries had an 8 mmHg difference with the aortic inlet. Conversely, this jump was negligible in the preprocedural model. From Figure 3.6, we can see that this jump was caused by the concomitant increase in the aortic input and a decrease in the coronary outflow.

3.1.7 Hemodynamic and Clinical Assessment

The present study proposes a patient-specific computational fluid dynamic analysis of a new TARR technology, an endovascular procedure consisting of the simultaneous replacement of the aortic valve, the aortic root and the proximal part of the ascending aorta. To the best of our knowledge, this study is the first computational study in this emerging field; indeed, literature only recalls a proof-of-concept experimental test of TARR proposed by Ferrari et al. [44], who used a CT-based 3D-printed root model to deploy the TARR components (endografts). In our previous article, we proved that the deployment of the endografts is feasible and also analysed the coronary flow, although in a very simplistic in vitro setting using water and neglecting coronary circulation and coronary resistances. In the present study, the coronary perfusion is implemented by the coupling of the 3D model of the aortic root, coronary ostia, ascending aorta and supra-aortic branches with a lumped parameter model (0D) of the coronary circulation [11]. The modelling of the coronary flow is of paramount importance for the development of any new TARR technology and we need reliable bench-test models to guarantee interpretable results when tests on coronary perfusion are performed. Our simulation results show that there is a negligible difference between preprocedural and post-procedural coronary perfusion, encouraging further analysis of the proposed TARR procedure towards its clinical implementation. However, at the same time, our results indicate an increase of the pressure drop between the coronary ostia and the aortic inflow section; we can attribute such an increase to the hydraulic resistance induced by the long chimney graft used in the post-procedural TARR configuration, in concomitance with the pressure increase at the aortic inlet, due to the reshaping of the aortic root and ascending aorta determined by the presence of the main endograft.

The increase in pressure can be interpreted as a downside of the intervention that has already been described as increasing post-procedural afterload in patients undergoing thoracic endovascular aortic repair [55]. Even though our simulation was performed within a rigid wall model, the native aorta becomes stiffer due to the higher rigidity of the stent graft compared to the native tissue [56]. Recent literature analysing the haemodynamics in chimney grafts associated high pressure drops to mid-term failure of the intervention in both the thoracic and the abdominal aorta [57], [58]. However, being this study he first in its type and without postoperative data of the patient, we cannot conclude whether the pressure jump that was found in the simulations is predictive of the failure of the coronary grafts.

The post-procedural reshaping of the dilated root and dilated ascending aorta produced, in our simulations, a flow that is more organized when com-

pared with the preprocedural one. This result confirms the phenomenon, already reported in patients with an aneurysm in the ascending aorta, where the postoperative configuration features less flow recirculation, which is known to be a factor triggering aneurysmal growth [59].

It is worth noting that our model proposes an idealization of the inlet cross-sectional sections of the chimney grafts, which can be elliptical due to compression induced by the main endograft, as shown in Figure 3.1 depicting the in vitro model. Moreover, we are neglecting gutters, which can be present between chimney grafts and the main endograft as long as the circumference of the main endograft is linear [60]. Nevertheless, this issue can be addressed using a pre-shaped main aortic endograft that presents the opposite incisures at the distal side that partially inglobe the chimney coronary grafts. As we mentioned earlier, the ascending aorta is a hostile environment in terms of biomechanics and future studies may require extending the distal part of the endograft to improve fixation. If that would be the case, the analysis of cerebral perfusion should be reconsidered to ensure that there are no deficits.

Regarding the study of helicity, Figure 3.10 highlights positive (in red) and negative (in blue) LNH values, corresponding to left- handed and right-handed rotating fluid structures along the flow direction in both the configurations, respectively. Therefore, even if the post-TARR configuration shows more helical structures than the pre-TARR configuration, the rotating flow structure has been maintained. The good agreement of the h_2 values between the two configurations, when considering the total volume, denotes that the post-procedural aortic model slightly affects the bulk flow, as we expected it. However, the gap obtained in coronary arteries should be analysed and studied in the next work, in which we will investigate more cases with different sizes and lengths of the grafts. Moreover, to the best of our knowledge, a comparison of the values of h_2 with a pre-operative and post-operative configuration in a patient-specific aorta is still missing in literature.

The last point to be mentioned, the model did not present a virtual aortic valve within the proximal portion of the main endograft. However, we believe that the valve does not interfere in the coronary bloodstream during TARR because the coronary inflows are displaced from the Valsalva Sinuses to the distal ascending aorta. Nevertheless, the presence of a temporary or a definitive aortic valve has to be taken into consideration in further simulations, in vitro or in vivo studies.

Limitations

Our results should be interpreted in the context of some limitations. First,

the results of our simulations should be validated against an in vitro model to test whether the results are comparable to reality. A further step could be a validation against post-procedural imaging [e.g. phase-contrast magnetic resonance imaging (MRI)] [61] if the TARR procedure with chimney grafts will be executed in animals or a real patient. Furthermore, this study has been conceived as a proof-of-concept to evaluate the feasibility of TARR using computational tools and therefore cannot be extrapolated to a wider population. To this aim, at least a retrospective study using more patients would be required. Secondly, the choice of the configuration of the main body of the prosthesis and the coronary grafts was fixed to follow our previous work [44]. Further work may include variations in the design suited for every single patient as well as different materials to modulate the rigidity of the grafts. This would avoid kinking that may compromise perfusion in the long term.

Thirdly, we assumed that the wall compliance is negligible, thus imposing a rigid wall condition according to Auricchio et al. [39] and Sankaran et al. [48]. In particular, Mendez et al. [62] proved that a stiff aneurysmal wall in the ascending aorta reduces differences in the shear stress predictions between a fluid structure interaction analysis and a CFD simulation.

In fourth place, a well-known limitation of such retrospective studies is the lack of patient-specific preoperative flow in the aorta to be used as boundary conditions. Having such data (i.e. extracted from PC-MRI) would enrich the simulation set-up and give more reliable results for each patient.

Finally, we are not accounting for long-term cardiac remodelling that can occur after endovascular aortic repair as we are using the same haemodynamic boundary conditions for pre- and post-procedural configuration; this aspect can be investigated in future developments of the present study implementing a lumped-parameter heart model calibrated with the pre- and post-TEVAR (thoracic endovascular repair) data as proposed by van Bakel et al. [34].

3.1.8 Clinical Message

Endovascular repair of the aortic root is certainly a challenging technological aim and has been addressed only by few authors. The focus of the work was to quantify with various haemodynamic indicators the impact on coronary circulation. With the proposed CAD modeling embedded into a reconstruction patient-specific dilation of the ascending aorta, we can conclude that the configuration proposed in our work does not significantly affect the coronary perfusion. A validation step has yet to be addressed as well as a less idealized representation of the coronary grafts. In particular, an in vivo study should be performed to confirm our in-silico results and provide clinically relevant conclusions.

Chapter 4

Turbulence Models: A Focus on Large-Eddy Simulation Models

Direct Numerical Simulation (DNS) is a simulation in the field of CFD in which the Navier-Stokes equations are numerically solved without any turbulence model, i.e. without averaging or approximating other than numerical discretizations, whose errors can be estimated and controlled [63]. In DNS the whole range of spatial and temporal scales of all of the motions must be resolved, from the smallest scale (Kolmogorov scale) up to the integral one, associated to the physical domain or the largest turbulent eddy. Such simulations require a certain number of mesh points, depending on Reynolds number, and growing very fast by Reynolds number increasing. Moreover, the time-step must be set small enough in order to satisfy the Courant number [63]. Therefore, the computational cost of a DNS is very high when considering turbulent flow (i.e. large Reynolds number flows over complex geometry). An alternative approach is called Large-Eddy Simulation (LES), in which the large scale motions are computed directly, while the small ones are modeled via low-pass filtering. LES models allow one to use coarser mesh and larger times-step sizes, resulting in a significance reduction in computational cost compared to DNS. The main idea of LES models arises from the following two considerations:

- the turbulent structures of intermediate scales are generated by the non-linear instability of large structures, they are also unstable, as characterized by still relatively high Reynolds numbers, they have the function of transferring the produced turbulent kinetic energy to small vortices, and received, by the large ones;

- small-scale turbulent structures arise from non-linear interactions between large and intermediate ones, are stable since they are characterized by low Reynolds numbers (of the order of unity), have a dissipative

nature and convert into heat, through viscosity, the turbulent kinetic energy transmitted to them by the intermediate eddies, have a much shorter average life than the other eddies and decay with an exponential law, have very short characteristic times and consequently a dynamics practically independent from that of large eddies and average motion, have relative dimensions compared to those of the large eddies which depend almost exclusively on the Reynolds number of the current.

For these reasons, LES models differentiate from RANS, in which there is no distinction between small and large scales and, hence, the effects of the entire spectrum of the spatial dimensions of turbulent scales, which could not be universal because they depend on geometry, should be simulated.

4.1 Definition and Properties of LES Filter

We consider, for the sake of simplicity, isotropic filters, i.e. filters applied to an unbounded domain with a constant and identical in all directions of space cutoff scale. The filtering is represented in physical space as a convolution product. The resolved part $\bar{\phi}(\boldsymbol{x},t)$ of a space-time variable $\phi(\boldsymbol{x},t)$ is defined by the relation:

$$\bar{\phi}(\boldsymbol{x},t)=\int_{-\infty}^{+\infty}\int_{-\infty}^{+\infty}\phi(\boldsymbol{\xi},t')G(\boldsymbol{x}-\boldsymbol{\xi},t-t')\,dt'd^3\boldsymbol{\xi},$$

where G is the convolution kernel, which is characteristic of the filtered used and associated with the cutoff scales in space and time, $\bar{\Delta}$ and $\bar{\tau}_c$, respectively. The dual definition in the Fourier space is obtained by multiplying the spectrum $\hat{\phi}(\boldsymbol{k},\omega)$ of $\phi(\boldsymbol{x},t)$ by the spectrum $\hat{G}(\boldsymbol{k},\omega)$ of the kernel $G(\boldsymbol{x},t)$:

$$\bar{\hat{\phi}}(\boldsymbol{k},\omega)=\hat{\phi}(\boldsymbol{k},\omega)\hat{G}(\boldsymbol{k},\omega), \tag{4.1.1}$$

where k and ω are the spatial wave number (i.e. the number of waves per unit distance) and time frequency, respectively. The function $\hat{G}$ is the transfer function associated with the kernel G. The unresolved part of $\phi(\boldsymbol{x},t)$, denoted by $\phi'(\boldsymbol{x},t)$, is defined as:

$$\begin{aligned}\phi'(\boldsymbol{x},t)&=\phi(\boldsymbol{x},t)-\bar{\phi}(\boldsymbol{x},t)\\&=\phi(\boldsymbol{x},t)-\int_{-\infty}^{+\infty}\int_{-\infty}^{+\infty}\phi(\boldsymbol{\xi},t')G(\boldsymbol{x}-\boldsymbol{\xi},t-t')\,dt'd^3\boldsymbol{\xi}.\end{aligned}$$

Using equation (4.1.1), the corresponding form in spectral space is:

$$\hat{\phi}'(\boldsymbol{k},\omega)=\hat{\phi}(\boldsymbol{k},\omega)-\bar{\hat{\phi}}(\boldsymbol{k},\omega)=\Big(1-\hat{G}(\boldsymbol{k},\omega)\Big)\hat{\phi}(\boldsymbol{k},\omega).$$

In order to write the Navier-Stokes equations, after applying a filter, we need the following properties associated to the filter:

1. Conservation of constants:
$$\bar{a} = a \iff \int_{-\infty}^{+\infty} \int_{-\infty}^{+\infty} G(\boldsymbol{\xi}, t')\, d^3\boldsymbol{\xi} dt' = 1.$$
2. Linearity:
$$\overline{\phi + \psi} = \bar{\phi} + \bar{\psi}.$$
3. Commutation with derivation:
$$\frac{\overline{\partial \phi}}{\partial s} = \frac{\partial \bar{\phi}}{\partial s}, \qquad s = \boldsymbol{x}, t.$$

We can now define the differential filters, which are realized by solving suitable partial differential equations linked to the physics of the problem. The name differential filter stresses the differences with the standard LES filtering, already described, which is made by space-averaging. More precisely, these filters are such that the kernel G is the Green's function associated to an inverse linear differential operator F:

$$\phi = F(\bar{\phi}) = \bar{\phi} + \theta \frac{\partial \bar{\phi}}{\partial t} + \overline{\Delta}_l \frac{\partial \bar{\phi}}{\partial x_l} + \overline{\Delta}_{lm} \frac{\partial^2 \bar{\phi}}{\partial x_l \partial x_m} + ...,$$

where θ and $\overline{\Delta}_l$ are some time and space scales, respectively. A filter is said to be elliptic (resp. parabolic or hyperbolic) if F is an elliptic (resp. parabolic, hyperbolic) operator. An elliptic filter is given by:

$$\phi = \bar{\phi} - \overline{\Delta}^2 \frac{\partial \bar{\phi}}{\partial x_l^2}.$$

This particular filter depends only on space. The convolutional integral form is:

$$\bar{\phi} = \frac{1}{4\pi \overline{\Delta}^2} \int \frac{\phi(\xi, t)}{|x - \xi|} \exp\left(-\frac{x - \xi}{\overline{\Delta}}\right) d\xi,$$

which satisfies the three basic properties described before.

Three classical filters for LES are the box (or top-hat), the Gaussian, and the spectral (or sharp cutoff) filter. We present only the filter used in Ansys Fluent for running the simulations, i.e. the box filter. In the mono-dimensional case, for a cutoff length $\overline{\Delta}$, the box filter is defined as:

$$G(x - \xi) = \begin{cases} \frac{1}{\overline{\Delta}} & \text{if } |x - \xi| \leq \frac{\overline{\Delta}}{2} \\ 0 & \text{otherwise} \end{cases}$$

$$\hat{G}(k) = \frac{\sin(k\overline{\Delta}/2)}{k\overline{\Delta}/2}.$$

Figure 4.1 represents the convolution kernel G (on the left) and the transfer function $\hat{G}$ (on the right).

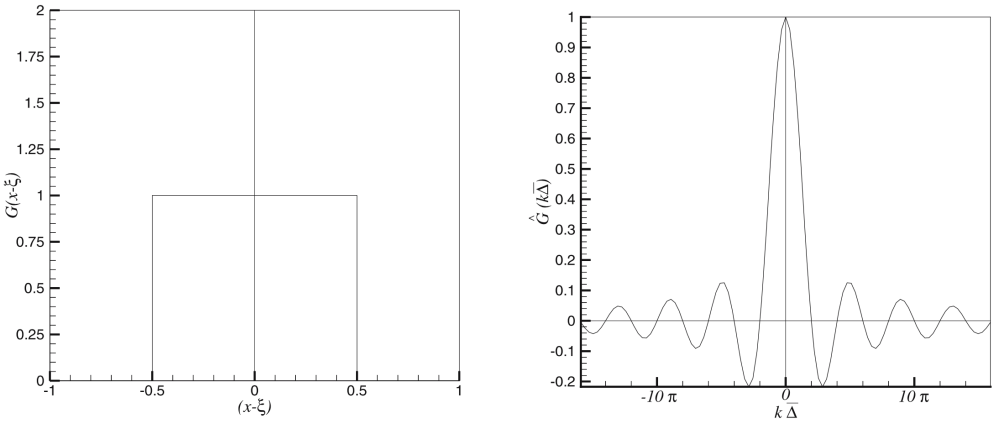

Figure 4.1: Box filter. Left: Convolution kernel in the physical space normalized by $\overline{\Delta}$. Right: Associated transfer function.

4.1.1 Filtered Navier-Stokes Equations

Firstly, we recall the incompressible Navier-Stokes equations, governing the motion of an incompressible Newtonian fluid. In the physical space, they are written as:

$$\frac{\partial u_i}{\partial t} + \frac{\partial (u_i u_j)}{\partial x_j} = -\frac{\partial p}{\partial x_i} + \nu \frac{\partial}{\partial x_j}\left(\frac{\partial u_i}{\partial x_j} + \frac{\partial u_j}{\partial x_i}\right), \qquad i = 1, 2, 3, \tag{4.1.2}$$

$$\frac{\partial u_i}{\partial x_i} = 0, \tag{4.1.3}$$

where $\boldsymbol{u} = (u_1, u_2, u_3)$ is the velocity field expressed in a reference Cartesian coordinate system $\boldsymbol{x} = (x_1, x_2, x_3)$, $p = P/\rho$ is the static pressure, ρ the density, and ν the uniform kinematic viscosity. Applying a filter to equations (4.1.2) and (4.1.3), and recalling the commutation with derivation, then:

$$\frac{\partial \bar{u}_i}{\partial t} + \frac{\partial (\overline{u_i u_j})}{\partial x_j} = -\frac{\partial \bar{p}}{\partial x_i} + \nu \frac{\partial}{\partial x_j}\left(\frac{\partial \bar{u}_i}{\partial x_j} + \frac{\partial \bar{u}_j}{\partial x_i}\right), \qquad i = 1, 2, 3, \tag{4.1.4}$$

$$\frac{\partial \bar{u}_i}{\partial x_i} = 0, \tag{4.1.5}$$

where $\bar{p}$ is the filtered pressure. In order to solve the system, we have to express the non-linear term $\overline{u_i u}_j$ as a function of the unknowns $\overline{\boldsymbol{u}}$ and $\boldsymbol{u'}$, where:

$$\boldsymbol{u'} = \boldsymbol{u} - \overline{\boldsymbol{u}}.$$

Leonard [76] decomposed the non-linear term in the following summation:

$$\begin{aligned}\overline{u_i u}_j &= \overline{(\bar{u}_i + u'_i)(\bar{u}_j + u'_j)} \\ &= \overline{\bar{u}_i \bar{u}_j} + \overline{\bar{u}_i u'_j} + \overline{u'_i \bar{u}_j} + \overline{u'_i u'_j}.\end{aligned}$$

Using Leonard's decomposition and defining the subgrid tensor as:

$$\begin{aligned}\tau_{ij} &= \overline{u_i u}_j - \overline{\bar{u}_i \bar{u}_j} \\ &= \overline{\bar{u}_i u'_j} + \overline{u'_i \bar{u}_j} + \overline{u'_i u'_j},\end{aligned} \tag{4.1.6}$$

we can write the filtered momentum equation (equation 4.1.4) as:

$$\frac{\partial \bar{u}_i}{\partial t} + \frac{\partial(\overline{\bar{u}_i \bar{u}_j})}{\partial x_j} = -\frac{\partial \bar{p}}{\partial x_i} + \nu \frac{\partial}{\partial x_j}\left(\frac{\partial \bar{u}_i}{\partial x_j} + \frac{\partial \bar{u}_j}{\partial x_i}\right) - \frac{\partial \tau_{ij}}{\partial x_j}, \qquad i = 1, 2, 3. \tag{4.1.7}$$

In particular, the subgrid scale can be expressed as:

$$\begin{aligned}\tau_{ij} &= (\overline{\bar{u}_i u'_j} + \overline{u'_i \bar{u}_j}) + \overline{u'_i u'_j} \\ &= C_{ij} + R_{ij},\end{aligned}$$

where the cross-stress tensor $C_{ij} = \overline{\bar{u}_i u'_j} + \overline{u'_i \bar{u}_j}$ represents the interactions between large and small scales, and the Reynolds subgrid tensor $R_{ij} = \overline{u'_i u'_j}$ the interactions between subgrid scales. Since the term $\overline{\bar{u}_i \bar{u}}_j$ can not be calculated directly, because it requires a second application of the filter, Leonard introduced a second decomposition:

$$\begin{aligned}\overline{\bar{u}_i \bar{u}}_j &= (\overline{\bar{u}_i \bar{u}}_j - \bar{u}_i \bar{u}_j) + \bar{u}_i \bar{u}_j \\ &= L_{ij} + \bar{u}_i \bar{u}_j\end{aligned} \tag{4.1.8}$$

by adding and subtracting the term $\bar{u}_i \bar{u}_j$. The Leonard stress tensor L represents the interactions among large scales. Including the Leonard stress tensor in the definition of the subgrid tensor τ, the latter takes the following form:

$$\begin{aligned}\tau_{ij} &= L_{ij} + C_{ij} + R_{ij} \\ &\overset{(4.1.6)}{=} L_{ij} + \overline{u_i u}_j - \overline{\bar{u}_i \bar{u}_j} \\ &= \overline{\bar{u}_i \bar{u}}_j - \bar{u}_i \bar{u}_j + \overline{u_i u}_j - \overline{\bar{u}_i \bar{u}_j} \\ &= \overline{u_i u}_j - \bar{u}_i \bar{u}_j.\end{aligned} \tag{4.1.9}$$

Using equations (4.1.8) and (4.1.9), the filtered momentum equation (4.1.7) becomes:

$$\frac{\partial \bar{u}_i}{\partial t} + \frac{\partial(\bar{u}_i\bar{u}_j)}{\partial x_j} = -\frac{\partial \bar{p}}{\partial x_i} + \nu\frac{\partial}{\partial x_j}\left(\frac{\partial \bar{u}_i}{\partial x_j} + \frac{\partial \bar{u}_j}{\partial x_i}\right) - \frac{\partial \tau_{ij}}{\partial x_j}, \qquad i = 1, 2, 3.$$

Therefore, the final form of the filtering governing equations for an incompressible fluid can be written as:

$$\frac{\partial \bar{u}_i}{\partial t} + \frac{\partial(\bar{u}_i\bar{u}_j)}{\partial x_j} = -\frac{\partial \bar{p}}{\partial x_i} + \nu\frac{\partial}{\partial x_j}\left(\frac{\partial \bar{u}_i}{\partial x_j} + \frac{\partial \bar{u}_j}{\partial x_i}\right) - \frac{\partial \tau_{ij}}{\partial x_j}, \qquad i = 1, 2, 3, \tag{4.1.10}$$

$$\frac{\partial \bar{u}_i}{\partial x_i} = 0. \tag{4.1.11}$$

Using the first decomposition in equation (4.1.6), the equation for the resolved kinetic energy $q_r^2 = \frac{1}{2}\bar{u}_i\bar{u}_i$ (multiplying the filtered momentum equation by $\bar{u}_i$) is:

$$\begin{aligned}\frac{\partial q_r^2}{\partial t} = &\underbrace{\overline{\bar{u}_i\bar{u}_j}\frac{\partial \bar{u}_i}{\partial x_j}}_{I} + \underbrace{\tau_{ij}\frac{\partial \bar{u}_i}{\partial x_j}}_{II} - \underbrace{\nu\frac{\partial \bar{u}_i}{\partial x_j}\frac{\partial \bar{u}_i}{\partial x_j}}_{III} - \underbrace{\frac{\partial(\bar{u}_i\bar{p})}{\partial x_i}}_{IV} \\ &+ \underbrace{\frac{\partial}{\partial x_i}\left(\nu\frac{\partial q_r^2}{\partial x_i}\right)}_{V} - \underbrace{\frac{\partial}{\partial x_j}(\bar{u}_i\overline{\bar{u}_i\bar{u}_j})}_{VI} - \underbrace{\frac{\partial(\bar{u}_i\tau_{ij})}{\partial x_j}}_{VII}.\end{aligned}$$

Each term involves the exchange of kinetic energy at the resolved scales:

- I: production
- II: subgrid dissipation
- III: dissipation by viscous effects
- IV: diffusion by pressure effect
- V: diffusion by viscous effects
- VI: diffusion by interaction among resolved scales
- VII: diffusion by interaction with subgrid tensor.

The subgrid kinetic energy q_{gsgs}^2 is defined as the half-trace of the subgrid tensor:

$$q_{gsgs}^2 = \frac{1}{2}\tau_{kk} = \frac{1}{2}\overline{u_i'u_i'} + \overline{\bar{u}_iu_i'}$$

Notice that, if the filter is not positive, can admit negative values locally.

As we have already pointed out, in order to reduce the complexity of the solution in space and time, LES resolves directly the large scales, while the small ones have been modeled. In particular, the terms involving the small scales, i.e. $\boldsymbol{u'}$ in the physical space and $(1-\hat{G})$ in the spectral one, can not be calculated directly and all the information concerning the small scales is lost. The subgrid modeling is performed by approximation of the terms, starting from the information contained in the resolved scales. Moreover, it must take into consideration the physical (i.e. conservation of Galilean invariance, asymptotic behaviors,...) and numerical constraints (i.e. acceptable algorithmic cost, no destabilization of the numerical simulation,...). The subgrid modeling can be grouped in two modeling strategies [66]:

1. *Structural modeling* of the subgrid term, which consists in making the best approximation of the tensor τ by constructing it from an evaluation of $\overline{\boldsymbol{u}}$ or a formal series expansion. This strategy consider a relation of the form $\boldsymbol{u'} = \mathcal{H}(\overline{\boldsymbol{u}})$ or $\tau = \mathcal{H}(\overline{\boldsymbol{u}})$. The knowledge of the nature of the inter-scale interaction is not require; however, a drawback consists in a sufficient knowledge of the structure of the small scales of the solution in order to be able to determine one of the relations $\boldsymbol{u'} = \mathcal{H}(\overline{\boldsymbol{u}})$ or $\tau = \mathcal{H}(\overline{\boldsymbol{u}})$.

2. *Functional modeling*, which consists in modeling the action of the subgrid terms on the quantity $\overline{\boldsymbol{u}}$ and not the tensor τ itself, i.e. introducing a dissipative or dispersive term. This approach uses a relation of the form $\nabla \cdot \tau = \mathcal{H}(\overline{\boldsymbol{u}})$.

In the present work we focus only on the functional modeling, and, in particular, on the subgrid scale models.

The subgrid scale models consists in considering information directly related to the subgrid scales. Thanks to the Boussinesq hypothesis [67], the subgrid scale models compute the subgrid-scale turbulent stresses from:

$$\tau_{ij} - \frac{1}{3}\tau_{kk}\delta_{ij} = -2\nu_{sgs}\overline{S}_{ij}. \tag{4.1.12}$$

The term $\overline{S}_{ij}$ is the rate-of-strain tensor for the resolved scale defined by:

$$\overline{S}_{ij} = \frac{1}{2}\left(\frac{\partial \bar{u}_i}{\partial x_j} + \frac{\partial \bar{u}_j}{\partial x_i}\right). \tag{4.1.13}$$

The isotropic part of the subgrid-scale stresses τ_{kk} is not modeled, but added to the filtered static pressure term, i.e. $\bar{p}^* = \bar{p} + \frac{1}{3}\tau_{kk}\delta_{ij}$. Then, equations (4.1.12) and (4.1.13), and the particular subgrid scale model selected lead to the closure problem. In the next section we introduce the most common subgrid models.

4.2 Common LES models

As many subgrid models can be found in literature, we briefly describe the main used subgrid models:

- **Smagorinsky-Lilly model:** It is the model that we adopt to perform aortic patient-specific simulations (see Chapter 5). A detailed description is reported in the next section.

- **Wall-Adapting Local Eddy Viscosity (WALE) model:** Developed by Ducrous et al. [68], it allows to incorporate the appropriate behavior near the wall into the eddy viscosity expression, i.e.

$$\nu_{sgs} = (C_W \overline{\nabla})^2 D_W,$$

where the differential operator D_W is defined as

$$\frac{(S^d_{ij} S^d_{ij})^{3/2}}{(\overline{S}_{ij}\overline{S}_{ij})^{5/2} + (S^d_{ij} S^d_{ij})^{5/4}},$$

and

$$S^d_{ij} = \frac{1}{2}(g^2_{ij} + g^2_{ji}) - \frac{1}{3}\delta_{ij} g^2_{kk}, \qquad g_{ij} = \frac{\partial \bar{u}_i}{\partial x_j}, \qquad g^2_{ij} = g_{ik} g_{kj}.$$

Typical value of C_W set in literature is $C_W = 0.325$ [69], [70]. This model is also well suited for LES in complex geometries because only local information is required to build the eddy-viscosity.

- **Algebraic Wall-Modeled LES (WMLES) model:** In this model, presented by Piomelli et al. [71], the grid spacing is chosen to scale with the local boundary-layer thickness. The eddy viscosity is modeled as

$$\nu_{sgs} = (C_{smag} \overline{\nabla})^2 S \left(1 - \exp\left(-\left(\frac{y^+}{25}\right)^3\right)\right),$$

where

$$\overline{\nabla} = \min(\max(C_w d_w; C_w h_{max}, h_{wn}); h_{max}),$$

d_w denotes the wall distance, $C_w = 0.15$ and $C_{smag} = 0.2$ constants, y^+ the normal to the wall inner scaling, h_{max} the maximum edge length for a rectilinear hexahedral cell, and h_{wn} the wall normal grid spacing.

- σ **model:** Including a constant, $C_\sigma \approx \frac{3}{2}$ it was introduced by Toda et al. [72]. The eddy viscosity is modeled as

$$\nu_{sgs} = (C_\sigma \overline{\nabla})^2 D_\sigma,$$

where D_σ is a differential operator incorporating the suitable wall behavior and some other related effects, i.e.

$$D_\sigma = \frac{\sigma_3(\sigma_1 - \sigma_2)(\sigma_2 - \sigma_3)}{\sigma_1^2}.$$

$\sigma_1 \geq \sigma_2 \geq \sigma_3 \geq 0$ are the singular values of the gradient tensor [72].

- **Dynamic Kinetic Energy Transport (KET) model:** It was proposed by Yoshizawa and Horiuti [73], in order to account for the subgrid-scale kinetic energy k_{SGS} in the expression for the eddy viscosity, instead of some differential operator function, i.e.

$$\nu_{sgs} = C_k \overline{\nabla} k_{SGS}^{1/2},$$

where

$$k_{SGS} = \frac{1}{2}(\overline{u_i u_i} - \bar{u}_i \bar{u}_i)$$

is the subgrid-scale kinetic energy. In particular, the kinetic subgrid-scale energy can be computed from the transport equation:

$$\frac{\partial k_{SGS}}{\partial t} + \bar{u}_j \frac{\partial k_{SGS}}{\partial x_j} = -\tau_{ij} \frac{\partial \bar{u}_i}{\partial x_j} - C_\epsilon \frac{k_{SGS}^{3/2}}{\overline{\nabla}} + \frac{\partial}{\partial x_j}\left(\frac{\nu_T}{\sigma} \frac{\partial k_{SGS}}{\partial x_j}\right),$$

where $\sigma = 1$. C_k and C_ϵ can be implemented as two constants or with a dynamic computation.

4.2.1 The Smagorinsky model

The Smagorinsky model was developed firstly by Smagorinsky in 1963 [74], and then by Lilly [75] and Leonard [76]. Deardorff used this model for the first time in numerical CFD simulations at large Reynolds numbers [77, 78]. The Smagorinsky model is characterized by a length scale term, a differential operator, and a dimensionless contstant C_S, called Smagorinsky coefficient. As for the length scale term, the idea is to related it with the filter cutoff scale $\overline{\Delta}$ and to represent it by applying some function of the mesh size as the general length scale term. A widely applied choice [79] consists in considering:

$$\overline{\Delta} = V_{cell}^{1/d},$$

where V_{cell} denotes the area/volume of a computational cell or element, and d corresponds to the geometrical dimension of the problem. The differential operator involved in the Smagorinsky model is the magnitude of the strain rate tensor, computed as:

$$|\overline{S}(\boldsymbol{x},t)| = \sqrt{(2\overline{S}_{ij}\overline{S}_{ij})}.$$

Then, the subgrid viscosity derived by dimensional arguments results in:

$$\nu_{sgs} = (C_S\overline{\Delta})^2|\overline{S}(\boldsymbol{x},t)|,$$

Therefore, the model produces less sub-grid scale turbulent viscosity as the mesh gets finer, approaching to a DNS. The Smagorisky coefficient C_S can be interpreted as a scaling factor of the turbulent eddies. In literature a rather wide range of recommended values for C_S can be found, often obtained by calibrating the model by comparison with solutions given by DNS. Reasonable values ranges from 0.065 (Moin et al. [65]), 0.1 (Deardorff [77]), 0.15 (Pope [80]), 0.17 (McMillan et al. [81] and Lilly [75]), to 0.185 and 0.23 (Lilly [82]). The default value of C_S set in Ansys Fluent is 0.1.

The Smagorinsky model is the oldest and simplest LES model; for this reason it was widely used in literature. In particular, Tan et al. [83] and Pal et al. [84] proved that this stable and robust LES model provides a good agreement to DNS, by comparing the results given by the CFD simulations of an idealized stenotic blood vessel. For these reasons we use the Smagorinsky model to perform CFD simulations in the next Chapter.

However, the Smagorinsky model has some drawbacks, that are summarized as follows:

- The value of the Smagorinsky coefficient needs to be calibrated, since it is not universal but depends on the spatial discretization, on the type of the filter used, and on the flow under consideration.
- The Smagorinsky model becomes too dissipative near the wall due to a large value of turbulence viscosity arising from the mean shear [65].
- Since C_S is a strictly positive constant, the eddy viscosity does not vanish for a laminar flow, and so the model damps the growth of small perturbation.

In order to reduce the excessive dissipation of the model, Ansys Fluent adopts the mixing length for subgrid scales L_S, defined as:

$$L_S = \min(kd, C_S\overline{\Delta}),$$

where k denotes the von Karman constant, and d the distance to the closest wall. Using this mixing length scale, the subgrid viscosity computed by Ansys Fluent becomes:

$$\nu_{sgs} = L_S^2 |\overline{S}(\boldsymbol{x}, t)|.$$

Chapter 5

Large-Eddy Simulation Models for Aortic Diseases

Aneurysm and dissections are the principal aortic diseases [85]. In particular, a thoracic aortic aneurysm is a permanent, localized dilatation of the thoracic aorta (see Figure 5.1). Detailed information and comprehension of the local hemodynamic is possible with computational fluid dynamic (CFD) simulations, which could facilitate the understanding of the disease progression for such aortic diseases.

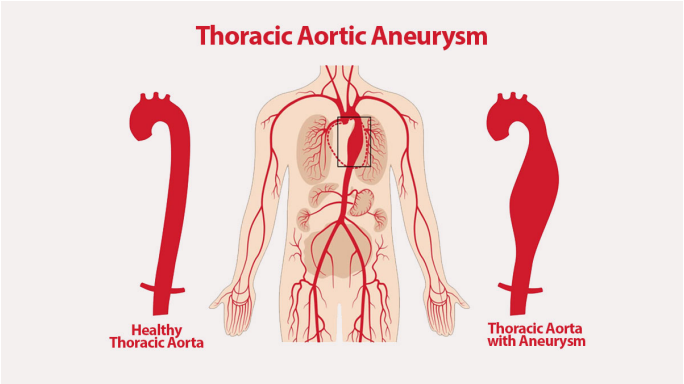

Figure 5.1: Sketch of a healthy (on the left) and aneurysmatic (on the right) thoracic aorta [86].

Aortic simulations are characterized by disturbed nature of the blood flow, induced by moderate/large values of Reynolds number and complex geometries, also caused by pathologies. The Reynolds number is a dimensionless number, depending on the density ρ, the diameter of the vessel D, the mean

blood velocity u, and the dynamic viscosity μ of the blood:

$$Re = \frac{\rho D u}{\mu}.$$

In a straight pipe, the flow remains stable and is called *laminar* if it is at most of the order of 2300, *transient* if it ranges between 2300 and 4000, *turbulent* if it exceeds the order of 4000 [87]. In general, the diameter of the human ascending aorta is about 25 mm, while typical values of blood velocity at the systolic peak and the corresponding Reynolds number are 1.0 cm/s and 4000, respectively [3]. Therefore, turbulent flow may occur at the exit of the aortic valve in correspondence to the systolic peak and when departing from physiological conditions due to physical exercise or some pathologies.

Patient-specific aortic simulations are particularly challenging for two main reasons. Firstly, DNS requires to solve in the computational mesh all the scales of motion, from the smallest dissipative scales, called Kolmogorov scales:

$$\eta = \left(\frac{\nu^3}{\varepsilon}\right)^{1/4} \tag{5.0.1}$$

up to the largest ones, called integral scales, L, containing most of the kinetic energy. In equation (5.0.1), ν is the kinematic viscosity and ε the rate of kinetic energy dissipation. Since the rate of kinetic energy dissipation can be approximated as $\varepsilon \propto u^3/L$ [88], the Kolmogorov scale becomes:

$$\eta = \left(\frac{\nu^3}{\varepsilon}\right)^{1/4} \propto \left(\frac{\nu^3 L}{u^3}\right)^{1/4} = L\left(\frac{\nu^3}{L^3 u^3}\right)^{1/4} = LRe^{-3/4}. \tag{5.0.2}$$

Using this latter equation (5.0.2), the number of points along to a spatial direction should be:

$$N_{\Delta x} = \frac{L}{\eta} \propto Re^{3/4}.$$

Hence, the computational cost of a DNS grows very fast with the increasing value of the Reynolds number. For example, if we consider typical values of diameter and peak velocity reported before, a common (three-dimensional) aortic DNS should require a number of mesh points of the order of 3000000, with standard values of blood density and viscosity. Therefore, aortic simulations are significantly expensive also for performing clusters. Alternative approaches are represented by RANS equations and LES. RANS models reduce significantly the computational cost compared to DNS and LES but also decrease the solution accuracy. Catalano et al. [89] investigated the viability

and accuracy of both LES and RANS simulations of the flow around a cylinder at high Reynolds numbers. Despite of the good agreement at the boundary layer, the LES solution was significantly more accurate than the RANS results. The same conclusion was achieved by Johari et al. [90], who simulated the disturbed flow in a patient-based stenosed carotid artery bifurcation. RANS-based SST-Tran model agree well with LES and experimental results at low and moderate Reynolds number; however, more accurate results were obtained with the LES model especially when the Reynolds number exceeded 2000. Therefore, in the present work we select a LES model to perform patient-specific aortic simulations. In particular, we adopt the Smagorinsky model for the advantages explained in the previous section, i.e. more simple and robust than the others LES models. However, the choice of a LES model implies a further challenge, i.e. the parameter estimation involved in the selected LES model. In particular, focusing on the Smagorinsky model, this latter requires the calibration of the Smagorinsky coefficient C_S in order to obtain accurate and stable solution. Meyers et al. [91] presented a theoretical analysis on the dependence of the Smagorinsky coefficient on the ratio of the LES filter width to the Kolmogorov scale $\overline{\Delta}/\nu$, the ratio of the integral length scale to the LES filter width $L/\overline{\Delta}$, and the type of the LES filter. Moreover, they introduced the following estimate of the Smagorinsky coefficient:

$$C_S^* = \frac{C_{S,\infty}}{\gamma}\sqrt{\max\left\{1 - \left(\frac{\gamma\eta}{C_{S,\infty}\Delta}\right)^{4/3}, 0\right\}}$$

where $C_{S,\infty} \approx 0.17$ denotes the Smagorinsky coefficient estimated by Lilly [75], and γ is a factor depending on the type of the filter. In particular, γ is defined as:

$$\gamma = \frac{\left(\frac{4}{3}\int_0^\infty k^{1/3}\big(G(k)\big)^2\,dk\right)^{3/4}}{\pi/\Delta}.$$

However, the estimate C_S^* does not take into account the choice of the boundary conditions enforced.

Proper boundary conditions should be considered in patient-specific CFD simulations to get reliable results. Dirichlet boundary conditions are usually affected by noise and are rarely available. In the last few years, Neumann boundary conditions are commonly adopted at the outlets with traction or pressure data, that are often derived from surrogate models. These surrogate models, such as the three-element Windkessel model [98], are tuned with patients' data and allow to get patient-specific values of flow and pressure at the boundaries. However, Neumann boundary conditions could induce numerical instability in presence of reverse flow, i.e. backflows or incoming flow. The reverse flow occurs when the blood flow is decelerating and together with the

prescription of Neumann boundary conditions leads to the so called backflows instabilities, due to the energy injection caused by the convective term in the energy estimate. The suppression of the backflows instabilities is particularly challenging, despite the use of very fine meshes. Xu et al. [18] proved theoretically and numerically, with idealized geometries and a single realistic case, that a particular deconvolution-based LES model, i.e. the Leray model with an Evolve-Filter-Relax scheme, implemented in open-source codes, is able to control the occurrence of the backflow instability. However, at the best of our knowledge, there is no study investigating on the suppression of the backflow instabilities with more classical LES models by tuning the LES parameters and using commercial software.

5.1 Large-Eddy Simulations for Thoracic Aortic Aneurysms

In literature, only few recently studies can be found on patient-specific simulations for thoracic aorta using LES models (Lantz et al. [92], Lantz et al. [17], Andersson et al. [93], Zakaria et al. [94], Xu et al. [18], and Manchester et al. [69], see Table 5.1). In particular, both the works of Lantz et al. [92] and Zakaria et al. [94] retrieved the geometry used in the simulations from the CT scan of healthy thoracic aorta, characterized by less complex geometry and less disturbed nature of flow. Moreover, unrealistic outlet boundary conditions with relative static pressure of 0 Pa at all four outlets were imposed in the study of Zakaria et al. [94]. Focusing on the simulations for thoracic aortic diseases, in the further study of Lantz et al. [17] the flow features in a thoracic aortic coarctation were analyzed, using the WALE model in the simulations. Dirichlet boundary conditions were imposed in all the outlets, excepts for the one corresponding to the descending aorta, in which a Neumann boundary condition was prescribed, thus restricting the possible occurence of backflow instabilities. A further step has been performed by Andersson et al. [93] only on the investigation of the properties of a new parameter, called transverse wall shear stress, computed accounting for the phase-average component of the wall shear stress (WSS) and the wall normal and time-average wall shear stress (TAWSS) direction. The same decomposition of the WSS into the phase-average and fluctuating component has been adopted by Manchester et al. [69]. The authors analyzed the turbulence effects in an aortic valve stenosis performing the simulations with the open source software OpenFoam. Patient-specific boundary conditions have been imposed at all the outlets by a proper estimation of the three-element Windkessel parameters. However, the parameter

ID	Protocol
Lantz et al. [92]	AIM: Investigation on the WSS in a human thoracic aorta using a LES turbulence model and measured velocity profiles as boundary conditions. METHODS: MRI acquisition was performed on a young healthy male. 4.8 million cells mesh was used in the simulations. Physiological inlet boundary condition; mass flow rates were specified on each of the three arteries in the aortic arch; in the descending aorta a three-element Windkessel model was imposed. The subgrid-scale eddy viscosity was modeled with the wall-adapted local eddy-viscosity (WALE) LES model ($C_{WALE} = 0.5$). The simulations were performed with ANSYS CFX 13.0, using a time-step of 1e-4 s.
Lantz et al. [17]	AIM: Study of the flow features in a thoracic aortic coarctation, and comparison on the kinetic and turbulent kinetic energy obtained in the numerical simulations to MRI measurements. METHODS: The simulations were carried out using ANSYS CFX 14.0, with the WALE model. velocity profiles measured by MRI were prescribed in the ascending aorta; measured mass flow rates were specified in the two vessels leaving the aortic arch; a pressure boundary condition was set in the descending aorta. The mesh sizes were on the order of 7 million anisotropic hexahedral cells.
Andersson et al. [93]	AIM: Investigation on the transverse wall shear stress (transWSS) properties in flows subjected to different pathological turbulent flow conditions, governed by a patient-specific model of a thoracic aortic coarctation pre and post balloon angioplasty. METHODS: The equations were solved in ANSYS CFX using a central difference and second-order backward Euler scheme for the spatial and temporal gradients. WALE subgrid model was used. The inflow of the ascending aorta was set by the 2D PC-MRI blood flow measurement, whereas a square law governed the vessels in the aortic arch.
Zakaria et al. [94]	AIM: Analyses of the blood clot potential in the patient specific aorta, through LES formulation on open source software OpenFOAM. METHODS: The CT scan of the thoracic aorta was obtained from the anatomical model of a healthy male 71 year old Malaysian subject. Transient inlet velocity waveform, and relative static pressure of 0 Pa at all 4 outlets. LES $k-\omega$ eddy viscosity model was used.
Xu et al. [18]	AIM: Provide a proof on both idealized and realistic cases that a particular LES model implicitly stabilizes the backflow instability. METHODS: A patient-specific aorta with an abdominal aneurysm is considered. Patient inlet velocity waveform, and 3-element Windkessel model for the outlets. The software LifeV was used for computation.
Manchester et al. [69]	AIM: Detailed analysis of turbulence effects in aortic valve stenosis. METHODS: Numerical simulations were performed using OpenFOAM, with WALE model ($C = 0.325$). 3-element Windkessel model was imposed at the three branch and descending thoracic aorta outlets. Mesh with 7.4 million cells was generated.

Table 5.1: Literature review on LES simulations for patient-specific thoracic aortic simulations.

estimation of the LES model was not motivated and investigated in correlation to the flow features and the fine mesh size adopted (7.4 million cells). Xu et al. [18] proved that a particular LES model, based on the Evolve-Filter-Relax scheme, implicitly stabilizes the backflow instability with a judicious selection of the parameters. A single patient with thoracic aortic aneurysm has been involved for the simulations performed using LifeV.

The aim of this work is to prove that the Smagorinsky model both provides accurate solution and stabilizes the backflow instability, even with relatively coarse meshes, thanks to a proper selection of the Smagorinsky coefficient. Note that decreasing the mesh size, also reduces the computational cost. In order to reach this goal, we consider three patient-specific geometries of aortic aneurysms, we impose boundary conditions using patients' data, and we vary the mesh size and the value of the corresponding Smagorinsky coefficient. In Figure 5.2 is represented the workflow of the present study. Due to the high computational cost, a DNS is performed only for the simplest and stablest case, in order to assess by comparison the results obtained by LES simulations.

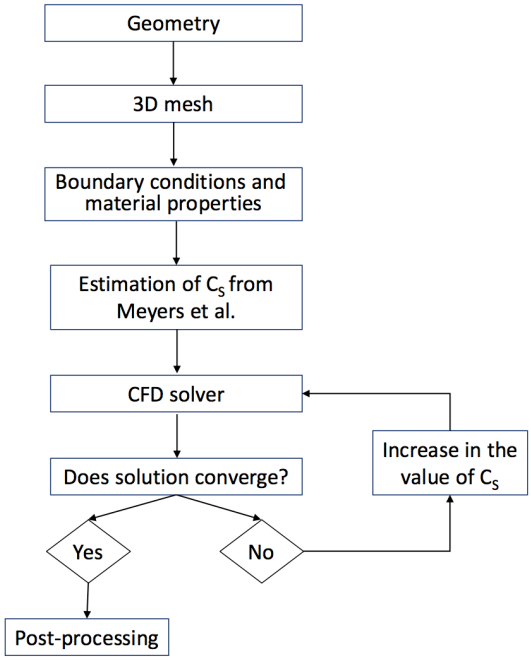

Figure 5.2: Block diagram corresponding to the workflow adopted for the present study.

5.1.1 Patient-Specific Geometries and CFD Setting

Data Acquisition

Three patients with an aneurysm in the vicinity of the aortic arch were selected from the framework of a Computer-Aided Clinical Trial, called iCardioCloud [95, 96]. The iCardioCloud project was developed thanks to a collaboration between the University of Pavia, the medical research hospital IRCCS Policlinico San Donato of Milan and the Department of Mathematics and Computer Science of Emory University. The trail collects 21 patients with different aortic diseases, such as thoracic aortic aneurysm, dissection, and coarctation. The computational domains, represented in Figure 5.3, were retrieved from the previous study of Romarowski et al. [46], who performed a level-set segmentation procedure using the software VMTK [97] from the contrast enhanced CT images. Moreover, flow extensions were added by the Authors to the computational domains at both the inlet and outlets, using VMTK. According to the label used in Figure 5.3, from now on we call Patient 1 the patient with the simplest geometry involved also to perform the DNS, Patient 2 the one with the most complex geometry and Patient 3 the remaining one.

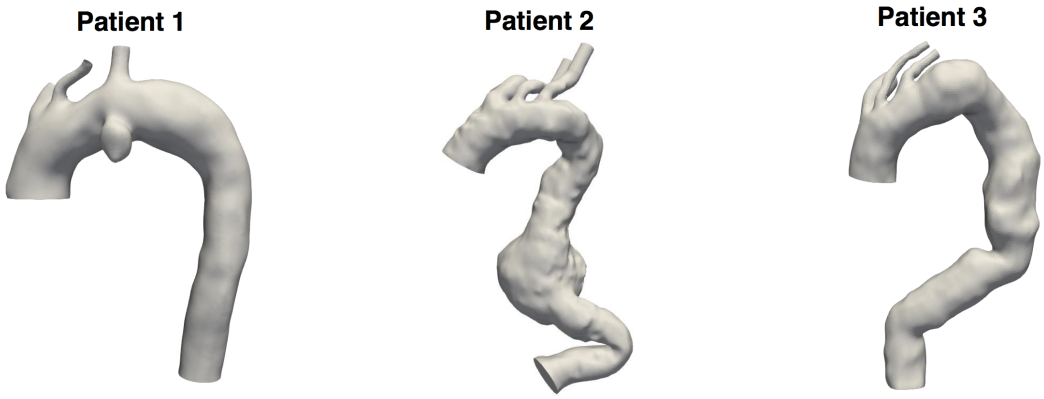

Figure 5.3: Computational domains used for the simulations in three aneurysmatic patients: left, patient 1; center, patient 2; and right, patient 3.

Spatial and Temporal Discretization

We generate three tetrahedral meshes (two for LES simulations and one for the DNS) related to Patient 1, and two tetrahedral meshes for both Patients 2 and 3. The meshes are generated using the software Netgen and ranges from 775996 to 2705272 elements. In Table 5.2 we report the number of elements of each mesh.

A time-step sensitivity analysis was conducted only on the coarsest mesh

Mesh	Patient 1			Patient 2		Patient 3	
	C_1	M_1	F_1	C_2	M_2	C_3	M_3
# nodes	136231	289827	468278	149206	341340	152084	319771
# tetrahedra	775996	1667209	2705272	806069	1962122	865365	1835887

Table 5.2: Details of the meshes used for Patient 1, 2, and 3. In particular C_1, C_2, C_3 denote the coarsest mesh generated for LES simulations corresponding to Patient 1, 2, and 3, respectively. M_1, M_2, M_3 are the finest mesh generated for LES simulations corresponding to Patient 1, 2, and 3, respectively. F_1 indicates the mesh used for the DNS corresponding to Patient 1.

of Patient 2 and two time-steps of $1e-3$ and $1e-4$ were considered. We found that the time-step $1e-3$ is suitable, with errors less than 1% relative to the smallest time-step. Concerning the other meshes, we maintain the same fix time-step of $1e-3$ after computing throughout the cardiac cycle the mean Courant-Friedrichs-Lewy (CFL) number, ensuring that this latter is less than 1.

Computational Model and Numerical Method

We report for clarity the spatially filtered Navier-Stokes equations for an incompressible fluid derived in the previous section (equations (4.1.10), (4.1.11)):

$$\frac{\partial \bar{u}_i}{\partial t} + \frac{\partial(\bar{u}_i\bar{u}_j)}{\partial x_j} = -\frac{\partial \bar{p}}{\partial x_i} + \nu\frac{\partial}{\partial x_j}\left(\frac{\partial \bar{u}_i}{\partial x_j} + \frac{\partial \bar{u}_j}{\partial x_i}\right) - \frac{\partial \tau_{ij}}{\partial x_j}, \qquad i = 1,2,3,$$
$$\frac{\partial \bar{u}_i}{\partial x_i} = 0.$$

To close the problem we select the Smagorinsky model, then

$$\nu_{sgs} = L_S^2|\overline{S}(\boldsymbol{x},t)|,$$

where L_S is defined in Ansys Fluent as $L_S = \min(kd, C_S\overline{\Delta})$. The Smagorinsky coefficient C_S was tuned for each simulation according to the mesh size and the amount of reverse flow (see Section 5.1.4. for more details). The transient CFD simulations were performed using Intel Xeon W-2123 computing workstation (3.6 GHz, 32 GB RAM) with the commercial software FLUENT (v.2020 R2, ANSYS Academic Research). We assume blood as an incompressible and Newtonian fluid, with a density of 1060 kg/m^3 and a dynamic viscosity of 0.0035 Pa s. Semi-implicit method for pressure linked equations (SIMPLE) was used to solve the Navier-Stokes equations. Second order scheme for both pressure and momentum spatial discretization were adopted. We performed the simulations until the sixth cardiac cycle, in order to achieve periodic solutions.

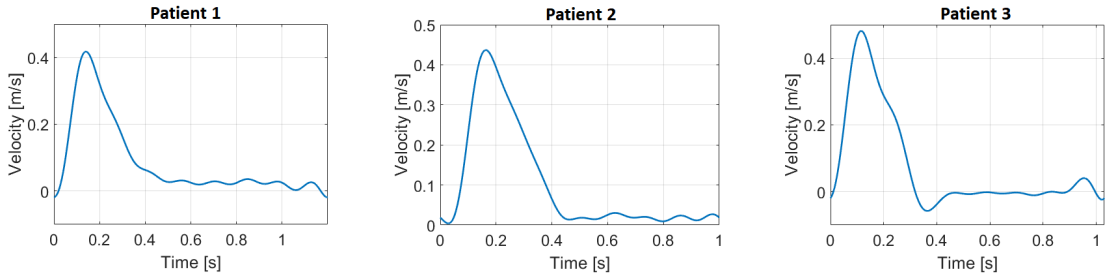

Figure 5.4: Inlet velocity waveforms over a cardiac cycle imposed in the simulations at the inlet of the patients: left, Patient 1; center, Patient 2; and right, Patient 3.

Transient inlet velocity waveform extracted from PC-MRI of each patient was imposed at the corresponding ascending aorta by writing a user defined function (UDF) to be interpreted in Ansys Fluent. The inlet velocity waveforms used in the simulations are shown in Figure 5.4. The peak Reynolds number at the ascending aorta is 4295, 4578, 4772 in Patient 1, 2, and 3, respectively. A three-element Windkessel model [98] was imposed at the three supra-aortic branches and descending thoracic aorta outlet. The values of the Windkessel parameters were taken from Romarowski et al. [46], who tuned the model parameters with patients' data (i.e. the same patients enrolled in this study). The parameter values set for each patient are summarized in Table 5.3. In particular, R_1 and R_2 represent the viscous dissipation in the proximal and distal region of the outflow, and C denotes the deformation of the arteries. Assuming rigid the vessel wall, the no-slip boundary condition was enforced at the wall.

	Patient 1			**Patient 2**			**Patient 3**		
	R_1	R_2	C	R_1	R_2	C	R_1	R_2	C
BCT	430	8930	1.06	841	22736	1.02	1091	12017	0.67
LCCA	4390	46736	0.15	3767	40660	0.39	3475	57727	0.16
LSA	1556	34083	0.42	1311	33240	3.39	701	27431	0.47
DA	73	1158	9.72	142	1423	11.95	43	1767	8.59

Table 5.3: Three-element Windkessel parameter values for each patient applied at the outlets: BCT, brachiocephalic trunk; DA, descending aorta; LCCA, left common carotid artery; LSA, left subclavian artery; DA descending aorta. The unit of the resistance values are in dynes s/cm^5, while the unit of the capacitance values are in 10^{-4} cm^5/dynes.

Post-processing For Patient 1, we perform both a qualitative and quantitative analysis comparing the results obtained from DNS and LES simulations. Qualitatively, velocity streamlines, velocity contours and vectors, flow rate and pressure waveforms at the boundaries, TAWSS, and oscillatory shear stress (OSI) are evaluated. In particular, velocity streamlines, contours and vectors are analyzed from the inlet velocity waveform in two instants of the last cardiac cycle, corresponding to: the systolic peak velocity ($t_{peak} = 0.140s$, $t_{peak} = 0.143s$, and $t_{peak} = 0.115s$ for Patient 1, 2, and 3, respectively), and the minimum velocity ($t_{min} = 1.198s$, $t_{min} = 0.143s$, and $t_{min} = 0.009s$ for Patient 1, 2, and 3, respectively). TAWSS represents the shear load over time that is subjected to the arterial wall, while OSI describes the changes of WSS over a cardiac cycle. TAWSS and OSI are computed, respectively, according to the following definitions:

$$TAWSS = \frac{1}{T}\int_0^T |WSS|\, dt \tag{5.1.1}$$

$$OSI = 0.5\left(1 - \frac{|\int_0^T WSS\, dt|}{\int_0^T |WSS|\, dt}\right) \tag{5.1.2}$$

where T is the cardiac period and |WSS| the norm of the WSS vector. In particular, we compute the WSS by the meaning of the tangential component of the normal stress, i.e.:

$$WSS = \mathbf{w} - (\mathbf{w}\cdot\mathbf{n})\mathbf{n}, \tag{5.1.3}$$

where the normal stress for a Newtonian fluid is

$$\mathbf{w} = p\mathbf{n} - \mu\left(\nabla\mathbf{u} + \nabla\mathbf{u}^T\right)\cdot\mathbf{n}. \tag{5.1.4}$$

For a DNS, μ in equation (5.1.4) denotes, as written before, the dynamic viscosity; however, in LES simulations the turbulent viscosity, μ_{turb}, plays a pivotal role, that we should account also in the calculation of the WSS. Therefore, for LES simulations we analyze the WSS computed both using the equation (5.1.3) and including the turbulent viscosity, i.e.:

$$\mathbf{w}_{turb} = p\mathbf{n} - (\mu + \mu_{turb})\left(\nabla\mathbf{u} + \nabla\mathbf{u}^T\right)\cdot\mathbf{n}, \tag{5.1.5}$$

$$WSS_{turb} = \mathbf{w}_{turb} - (\mathbf{w}_{turb}\cdot\mathbf{n})\mathbf{n}. \tag{5.1.6}$$

WSS and WSS_{turb} are calculated with ParaView, an open-source visualization framework [99]. Ansys Fluent allows to export the WSS computed during the simulation, but it calculates the WSS in two ways, depending on the size of the mesh considered, i.e.:

$$\mathbf{w} = \mu\frac{\overline{\mathbf{u}}}{y}$$

if the mesh is fine enough to resolve the laminar sublayer [100], otherwise

$$\mathbf{w} = \rho \left(\frac{\overline{\mathbf{u}}\ k}{\ln\left(\frac{E\rho\sqrt{\mathbf{w}/\rho}\ y}{\mu}\right)} \right)^2,$$

where y is the wall-normal distance calculated at the cell centers and $E = 9.793$ an empirical constant obtained for the surface roughness and the flat wall surfaces. Therefore, in order to perform a consistent comparison between DNS and LES simulations, we compute the WSS in ParaView using equations (5.1.3) and (5.1.6) for each simulation. Quantitatively, the percentage area of high OSI (> 0.3), the h_2 index, and the percentage area of low ($< 25^{th}$ percentile) and high TAWSS ($> 75^{th}$ percentile) are compared between the results obtained from DNS and LES simulations. In particular, the h_2 index is a measure concerning the bulk flow, given by time-averaging the absolute value of the helicity [101]:

$$h_2 = \frac{1}{TV} \int_T \int_V |\mathbf{u} \cdot (\nabla \times \mathbf{u})|\, dV dt,$$

where V is the arterial volume. The h_2 index expresses the helicity intensity in the fluid domain, irrespective of direction. In order to facilitate the comparison and to evaluate the impact of the LES model in specific regions, the computational domain is divided into 5 zones (see Figure 5.5): (1) ascending aorta, (2) aortic arch, (3) aneurysm, (4) thoracic aorta, and (5) descending aorta.

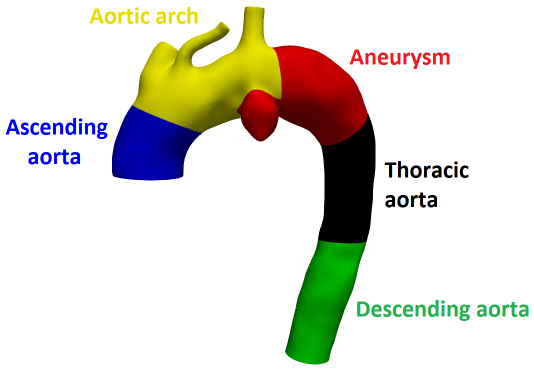

Figure 5.5: Thoracic aorta of Patient 1 colored according to the five zones under investigation: ascending aorta, aortic arch, aneurysm, thoracic aorta, descending aorta.

Concerning Patients 2 and 3, we assess the results of the LES simulations focusing on the calibration of the Smagorinsky coefficient and the flow features, in order to understand how they correlates. We calculate the velocity vectors at the outlets, the amount of antegrade/retrograde flow, and the ejection fraction (EF) at the corresponding inlet and outlets. Reverse flow is a physiologic phenomenon occurring at relative large branches, i.e. the supra-aortic branches [102] and descending abdominal aorta [103], in both healthy and diseased subjects. It is present often during blood flow deceleration, at late systole and early diastole. Therefore, reproducing reverse flow, by suppressing the backflow instabilities, is fundamental for realistic simulations. The ejection fraction is a measurement of the percentage of blood ejected from a chamber with each heartbeat. In particular, in the present study it is computed both at the inlet and the outlets, as an indicator of the amount of blood flow incoming into the ascending aorta and outgoing the supra-aortic branches and the descending aorta, respectively. It is defined as:

$$EF[\%] = \frac{\text{Antegrade flow}}{\text{Total flow}} \times 100,$$

thus, an ejection fraction of 100% means that no reversal flow occurs at the considered inlet/outlet.

5.1.2 Numerical results

Comparison Between DNS and LES simulations in Patient 1

In order to evaluate and prove the accuracy of the solution given by LES simulations, we first compare the results obtained from DNS with those from LES simulations performed with Patient 1. Figures 5.6 and 5.7 show the velocity streamlines along the aorta (top), velocity contours and vectors (bottom) at the time instant corresponding to the peak systole, t_{peak}, and the minimum velocity, t_{min}, respectively. We report the results relating to the two outlets where more reverse flow occurs and more differences can be noted, i.e. left common carotid and left subclavian arteries. At the systolic peak the stabilized velocity from all the simulations are qualitatively consistent, even if the results obtained with the fine mesh match better the results given by the DNS, especially at the left common carotid artery. At the time instant corresponding to the minimum velocity, the results from all the simulations capture the reverse flow at the left common carotid and left subclavian arteries. However, the velocity magnitude is more uniform in the simulation performed with the coarse mesh.

Figure 5.8 represents the TAWSS and OSI, both computed according to equations ((5.1.1)-(5.1.4)). The distribution of the magnitude of TAWSS ob-

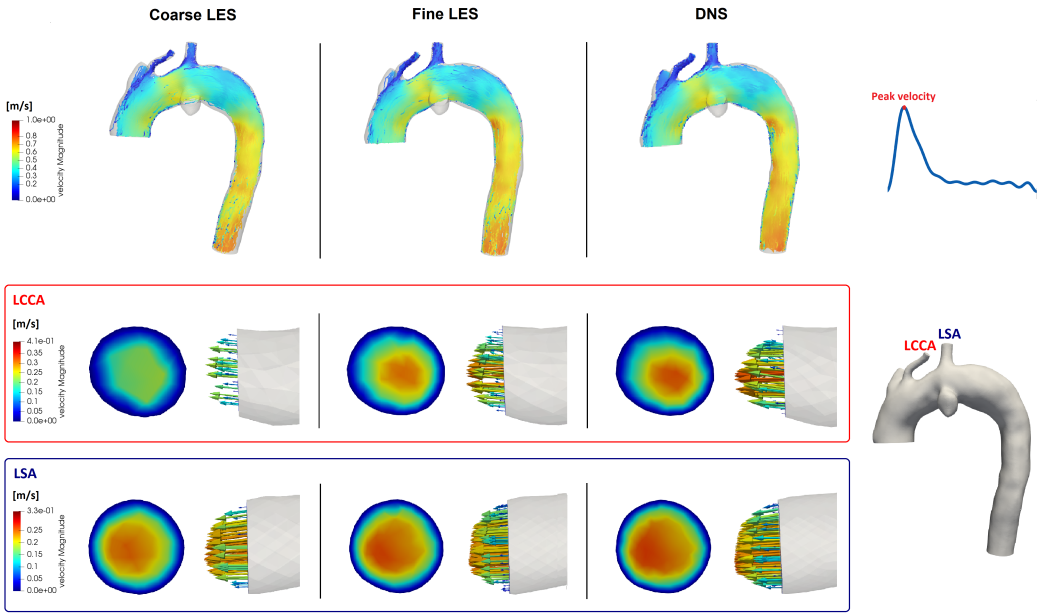

Figure 5.6: Qualitative comparison of velocity streamlines (top), contours, and vectors (bottom) with the two *LES* simulations and the DNS at the peak systole. The velocity contours and vectors illustrated corresponds to the plane in the left common carotid artery (LCCA) and left subclavian artery (LSA).

tained from the coarse mesh appears underestimated compared to the DNS, while the magnitude of TAWSS with the fine mesh agrees well with the DNS one. Analogously, the distribution of OSI in the Fine LES simulation is more consistent with the DNS results than in the Coarse LES one, in which OSI assumes lower values. Figure 5.9 illustrates the TAWSS and OSI computed taking into account the turbulent viscosity, according to equations (5.1.5-5.1.6). The magnitude of TAWSS is overestimated in both *Coarse LES* and *Fine LES* respect to the DNS. Conversely, the distribution of OSI is underestimated than the one of DNS.

Qualitative and quantitative comparison of the area exposed to low ($< 25^{th}$ percentile of DNS) and high ($> 75^{th}$ percentile of DNS) TAWSS, computed without accounting the turbulent viscosity, is shown in Figure 5.10. Qualitatively, the area exposed to low/high TAWSS in the *Fine LES* is consistent to the DNS; on the contrary, the results of the *Coarse LES* do not match the distribution of the DNS. The luminal surface exposed to low TAWSS in the *Coarse LES* is greater than the one of the DNS, while the area exposed to high TAWSS is almost absent. These latter considerations are corroborated by the quantitative analysis. The percentage area exposed to high TAWSS is

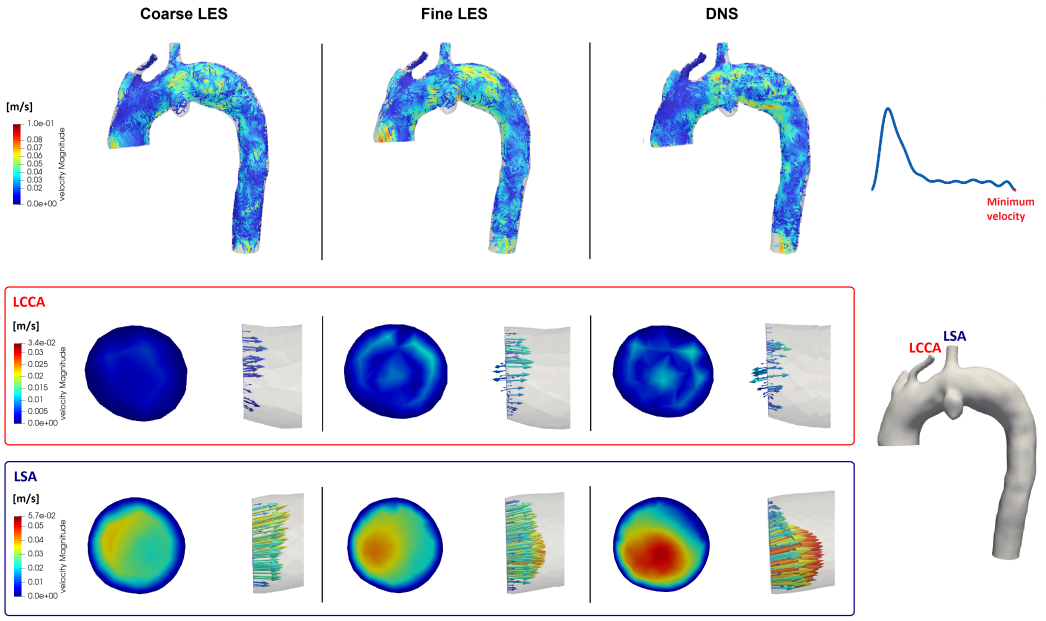

Figure 5.7: Qualitative comparison of velocity streamlines (top), contours, and vectors (bottom) with the two *LES* simulations and the DNS at late diastole, corresponding to Patient 1. The velocity contours and vectors illustrated corresponds to the plane in the left common carotid artery (LCCA) and left subclavian artery (LSA).

significantly lower in the *Coarse LES*, in which appears only in the zones corresponding to the thoracic and descending aorta (area of high TAWSS is 0.05% and 0.11% in thoracic and descending aorta, respectively). The surface exposed to low TAWSS is grater than the DNS results in each zone, with a maximum difference of +40.3% in the region of aneurysm. Qualitative and quantitative comparison of the area exposed to low ($< 25^{th}$ percentile) and high ($> 75^{th}$ percentile) TAWSS including the turbulent viscosity is represented in Figure 5.11. The results are qualitatively and quantitatively consistent, even if the area exposed to high TAWSS is greater in the zones corresponding to the thoracic and descending aorta respect to the DNS. Moreover, the distribution of the area exposed to low $TAWSS$ is more uniform in the *Coarse LES* and *Fine LES* than the DNS. Figure 5.12 reports the area exposed to high OSI ($>$ 0.3), computed without taking into account the turbulent viscosity, and the h_2 index corresponding to each zone into which the aorta has been divided. Both the LES simulations well agree with the results of the DNS; in particular, a better matching can be noted for the *Fine LES* to the DNS. Figure 5.13 shows the area exposed to high OSI (> 0.3), computed with $TAWSS_{turb}$, in

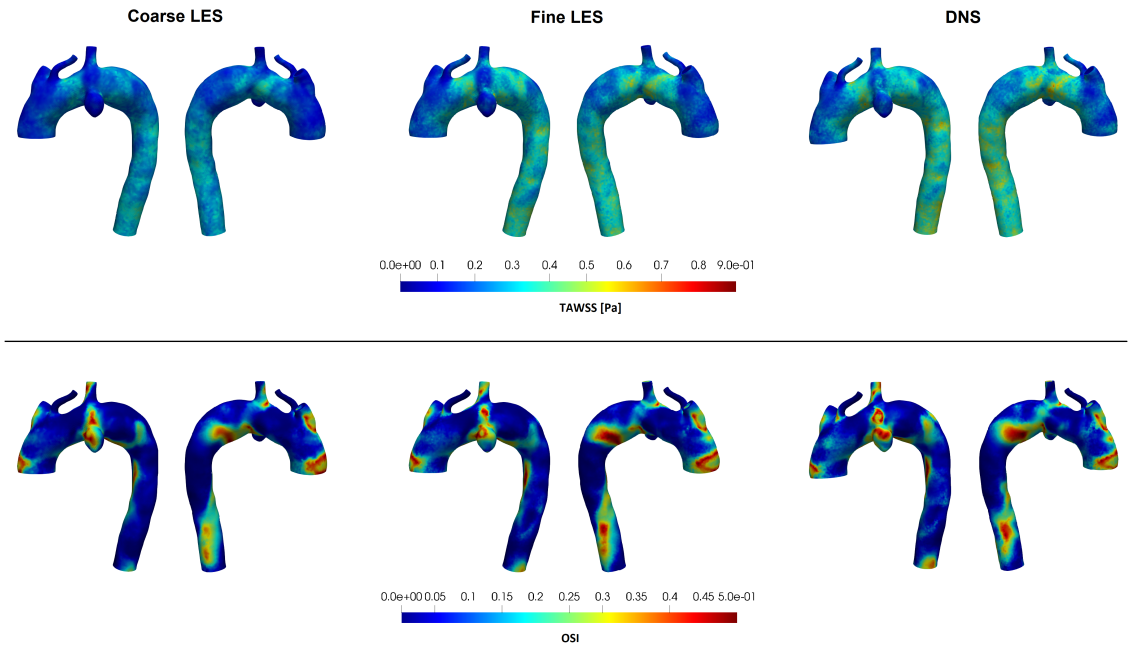

Figure 5.8: Qualitative comparison of TAWSS (top) and OSI (bottom) with the two *LES* simulations and the DNS, corresponding to Patient 1. TAWSS and OSI are computed in Paraview according to equations ((5.1.1)-(5.1.4)).

each zone. More differences are highlighted in the zones corresponding to the aneurysm, thoracic and descending aorta, in which the area exposed to high OSI is significantly lower in both the LES simulations than the one given by the DNS.

5.1.3 Hemodynamic and Clinical Assessment

The main purpose of the present study is to compare the performed LES simulations, corresponding to Patient 1, with: (1) the DNS, in order to prove that the LES model allows to obtain accurate results with lower computational cost; and (2) other LES simulations, corresponding to two aneurysmatic patients, in order to demonstrate that with a proper selection of the parameter value C_S, depending on the mesh size and the flow features, all the LES simulations performed well controls the numerical instabilities.

We assess the first comparison with the DNS by computing the velocity streamlines and vectors, TAWSS, and OSI. The parameter selection is then investigated by focusing on the flow features of the three patients, i.e. calculating the amount of antegrade/retrograde flow, the velocity vectors at the outlets,

and the ejection fraction.

Velocity streamlines, contours, and vectors

At systolic peak, fairly organized flow patterns occur in the whole computational domain (see Figure 5.6). In Figure 5.6, the velocity streamlines, contours, and vectors appear in good agreement especially with the fine mesh and the DNS. Few differences can be captured with the coarse mesh at left common carotid artery, in which a lower and more uniform velocity results. This inconsistency could be due to an excessive dissipation introduced by the LES model and/or the mesh size, not fine enough to guarantee the accuracy of the solution. Analogue pattern, but less evident than the previous one at the left common carotid artery, occurs at the left subclavian artery with the coarse mesh. Indeed, focusing on the velocity contours, the velocity magnitude obtained with the coarse mesh appears slightly lower in the center of the outlet than the others.

At the late systole, the blood flow is decelerating and consequently results in a combination of helical and recirculating secondary flows, especially in the aneurysmatic zones, according to literature [18], [104]. Concerning Patient 1,

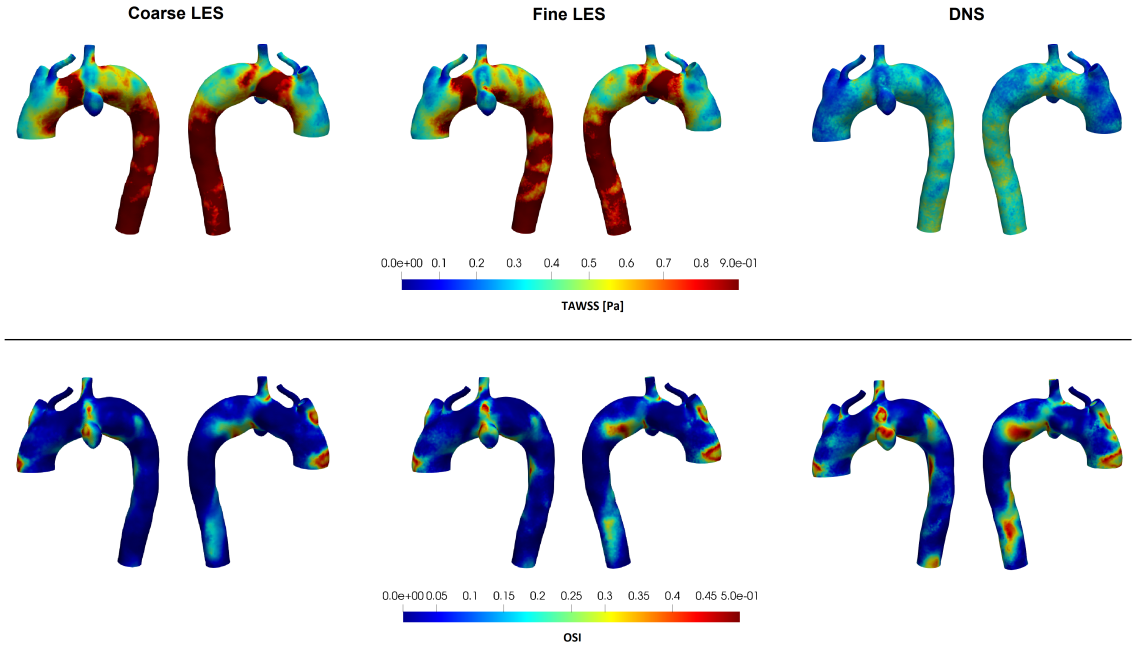

Figure 5.9: Qualitative comparison of TAWSS (top) and OSI (bottom) with the two *LES* simulations and the DNS, corresponding to Patient 1. TAWSS and OSI are computed in Paraview according to equations (5.1.5-5.1.6).

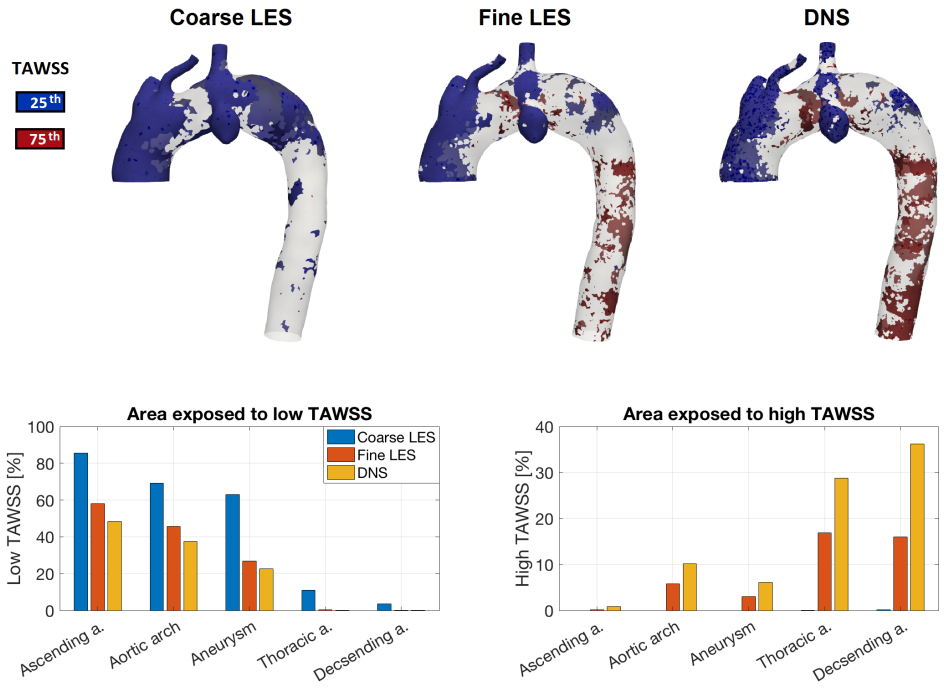

Figure 5.10: Top: qualitative comparison of the area exposed to low ($< 25^{th}$ percentile of DNS) and high ($> 75^{th}$ percentile of DNS) TAWSS, computed according to equations ((5.1.1), (5.1.3)-(5.1.4)), with the two LES simulations and the DNS, corresponding to Patient 1. Bottom: bar plots of the percentage area exposed to low and high TAWSS in the five zone under investigation (ascending aorta, aortic arch, aneurysm, thoracic aorta, descending aorta) of Patient 1.

this vortical flow pattern remains also during diastole in the whole computational domain (see the velocity streamlines at the top of Figure 5.7). Retrograde flow occurs both at left common carotid and left subclavian arteries (see Figure 5.7). In particular, at the time instant corresponding to the minimum velocity, the flow is completely retrograde with all the meshes at the left subclavian artery, looking for the velocity vectors in Figure 5.7. Low antegrade flow is present only at the center of the section corresponding to the left common carotid artery with the fine and DNS meshes, while with the coarsest one no antegrade flow occurs. Focusing on the velocity contours represented in Figure 5.7), the velocity appears increasingly lower as the mesh size decreases, compared to that obtained from the DNS at both the outlets illustrated in Figure 5.7). Moreover, the velocity is more uniform with the coarse mesh, resulting almost zero at the whole section corresponding to the left common carotid

artery. A more uniform velocity was observed at the brachiocephalic trunk also by Xu et al. [18], who argued that the more uniform velocity field than the expected physiological one [105]-[107] is due to an excessive stabilization, like an effect of the penalization on the velocity gradient introduced at the boundary.

Time-Averaged Wall Shear Stress

TAWSS is one of the quantities of clinical relevance in understanding the arterial disease progression [108]. According to Malek et al. [109], the area exposed to low TAWSS (i.e. ascending aorta and aneurysm) is more prone to atherosclerosis, while high level of TAWSS (i.e. present in descending aorta) could be induced endothelial quiescence and an atheroprotective gene expression profile. Figure 5.8 (at the top) shows the TAWSS distributions, computed without accounting to the turbulent viscosity, for the three simulations. Low

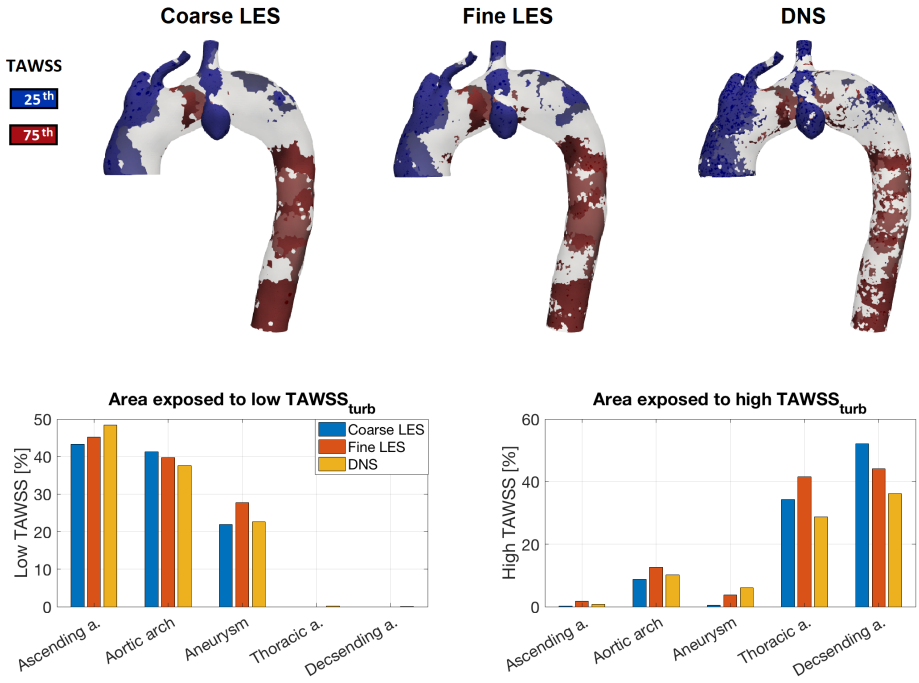

Figure 5.11: Top: qualitative comparison of the area exposed to low ($< 25^{th}$ percentile of DNS) and high ($> 75^{th}$ percentile of DNS) TAWSS, computed according to equations (5.1.5-5.1.6), with the two *LES* simulations and the DNS, corresponding to Patient 1. Bottom: bar plots of the percentage area exposed to low and high TAWSS in the five zone under investigation (ascending aorta, aortic arch, aneurysm, thoracic aorta, descending aorta) of Patient 1.

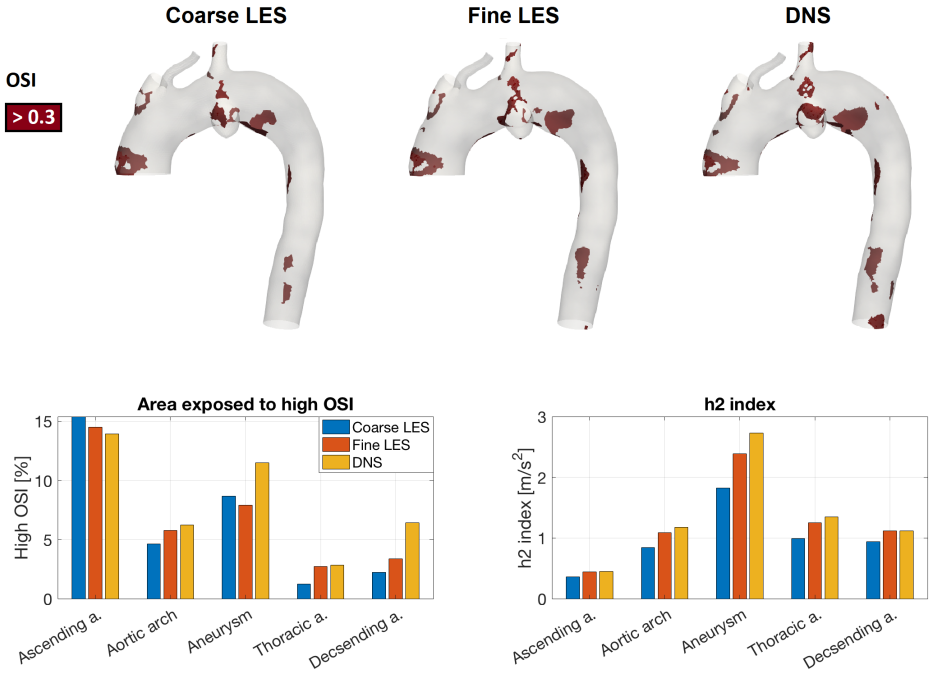

Figure 5.12: Top: qualitative comparison of the area exposed to high OSI ($>$ 0.3), computed according to equations ((5.1.2)-(5.1.4)), with the two *LES* simulations and the DNS, corresponding to Patient 1. Bottom: bar plots of the percentage area exposed to high OSI (left) and helicity (h_2 index) in the five zone under investigation (ascending aorta, aortic arch, aneurysm, thoracic aorta, descending aorta) of Patient 1.

TAWSS occurs in the zones corresponding to the ascending aorta, supra-aortic branches, and aneurysm. Viceversa, higher values of TAWSS result in the descending aorta region. Comparing the magnitude of TAWSS computed from the three simulations, the distribution of TAWSS is qualitatively consistent. However, lower values of TAWSS are observed along the aorta with the coarsest mesh. The same distribution of TAWSS but with different intensities, except for the DNS, is highlighted in Figure 5.9 at the top, in which TAWSS is computed also taking into account the subgrid viscosity. Indeed, the TAWSS computed from the coarse and fine meshes is characterized from significantly higher values than the ones represented in Figure 5.8, due to the additional subgrid viscosity in the TAWSS calculation (equation (5.1.6)). The TAWSS obtained from the DNS corresponds to that one shown in Figure 5.8, since a DNS is not affected to the turbulent viscosity.

In order to quantify the low/high values of TAWSS and provide a clinical message, the percentage area exposed to TAWSS lower than the 25^{th} percentile

and higher than 75^{th} percentile of the TAWSS magnitude, given by the DNS, is calculated. Firstly, we compare the percentage area exposed to low/high TAWSS computed without the turbulent viscosity (see Figure 5.10) from the three simulations. The results given by the three simulations show a predominant area exposed to low TAWSS in the zones corresponding to the ascending aorta, aortic arch, and aneurysm. However, while with the coarse mesh the area exposed to high TAWSS is almost absent in the entire aortic wall, Figure 5.10 shows zones with high TAWSS especially at descending aorta with the fine and DNS meshes. In particular, comparing to the DNS, the area exposed to low TAWSS is overestimated with the coarse mesh but consistent with the fine mesh. The maximum difference between the percentage area exposed to low TAWSS in the DNS and the other two simulations is 40.3% in the zone corresponding to the aneurysm in the coarse mesh and 9.6% in the region corresponding to the ascending aorta of the fine mesh. Viceversa, the area ex-

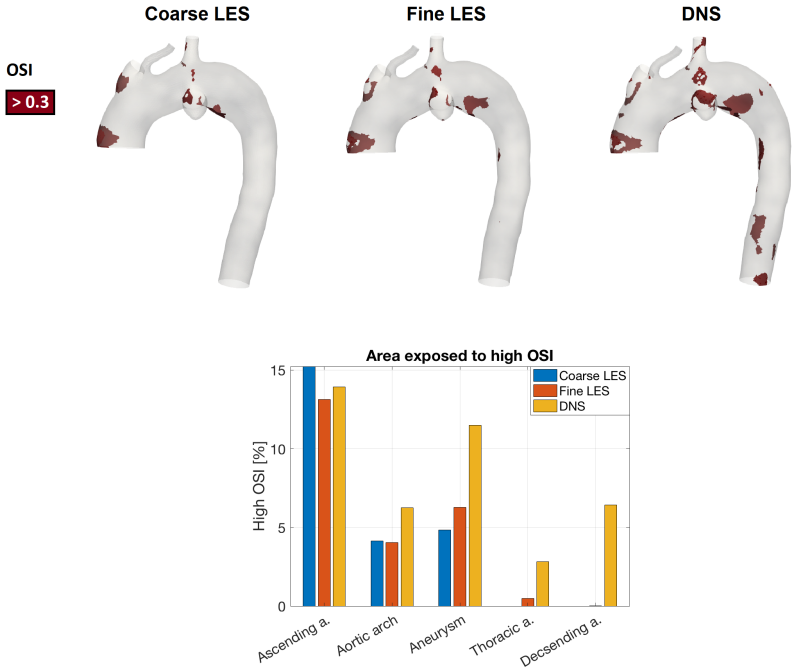

Figure 5.13: Top: qualitative comparison of the area exposed to high OSI ($>$ 0.3), computed according to equations (5.1.2, 5.1.5-5.1.6), with the two *LES* simulations and the DNS, corresponding to Patient 1. Bottom: bar plot of the percentage area exposed to high OSI in the five zone under investigation (ascending aorta, aortic arch, aneurysm, thoracic aorta, descending aorta) of Patient 1.

posed to high TAWSS is underestimated by the LES simulations comparing to the DNS; the difference is more evident with the coarse mesh. Indeed, the maximum difference between the percentage area exposed to high TAWSS in the DNS and the other two simulations is 36.0% in the coarse mesh and 20.1% with the fine mesh, referring both to the zone corresponding to the descending aorta.

Analogously, we compare the area exposed low/high TAWSS computed taking into account the turbulent viscosity (see Figure 5.11). Calculating the 25^{th} and 75^{th} percentile of the TAWSS magnitude for each simulation, the results are more consistent to the previous ones, computed without turbulent viscosity and using the 25^{th} and 75^{th} percentile of the DNS as the threshold for the LES results. In particular, the maximum difference between the percentage area exposed to low TAWSS in the DNS and the other two simulations is 5.1% in the zone corresponding to the ascending aorta in the coarse mesh and 5.2% in the region corresponding to the aneurysm of the fine mesh, respectively. Focusing on the high TAWSS, the maximum difference between the percentage area exposed to high TAWSS in the DNS and the other two simulations is 16.0% in the zone corresponding to the descending aorta in the coarse mesh and 12.81% in the region corresponding to the thoracic aorta of the fine mesh. Therefore, the 25^{th} and 75^{th} percentile, computed from the TAWSS magnitude of each LES simulation and used as a threshold to quantify the area exposed to low/high TAWSS, provides consistent results comparing to the DNS ones.

Oscillatory Shear Index

OSI is a relevant index of the temporal oscillations of the WSS. Ranging between 0 and 0.5, it denotes the sites where the direction of the WSS vector changes from the main blood flow direction during a cardiac cycle [108]. Therefore, the greater the OSI values are, the more the WSS oscillates in relation to the predominant direction.

Figure 5.8 (at the bottom) shows the qualitative comparison of OSI, computed without the turbulent viscosity, with the two LES simulations and the DNS. The results of the LES simulations are in good agreement with the OSI obtained from the DNS. However, lower values of OSI can be captured in the coarse mesh, especially in the zones corresponding to the aortic arch and descending aorta.

High OSI values occur at the outer wall of the ascending aorta and in some localized areas of the left subclavian artery, aneurysm, and descending aorta in each simulation, because of the oscillation of the flow direction and the WSS vector during the cardiac cycle. Note that these zones characterized by high OSI values corresponds to the areas exposed to low TAWSS and low

velocities (see Figures 5.6 and 5.8). Low WSS distribution associated with low velocity and high OSI was found in literature to be a useful index to quantify the hemodynamics alterations and predict the disease progression [110], [111], [112], [113], [114]. The two latter studies [113], Zhu et al. [114] argue that the regions with high values of OSI and low values of WSS are more prone to rupture. In particular, Alimohamadi et al. [113] proved the rupture risk of aneurysm highlighting the interaction of two vortices counter-rotating in their results.

Focusing on the quantitative analysis (see Figure 5.12), the area exposed mostly to high values of OSI is localized at the wall of ascending aorta (13.9% obtained from the DNS), while the area exposed to lower values of OSI occurs at the wall of the thoracic aorta (2.8% obtained from the DNS). The results given by the LES simulations are consistent with the ones of the DNS. In particular, LES results agree better with the DNS with mesh refining, except in the zone corresponding to the aneurysm, in which the difference between the percentage area exposed to low TAWSS in the DNS and the other two simulations is lower with the coarse mesh (2.8% and 3.6% with the coarse and fine mesh, respectively). The maximum difference between the percentage area exposed to high OSI in the DNS and the other two simulations is 4.2% in the zone corresponding to the descending aorta in the coarse mesh.

Helicity

As for the characterization and quantification of helical flow, the h_2 index is computed in each zone in which we subdivided the aorta (see Figure 5.5). Figure 5.12, at the bottom, shows the results obtained from the three simulations. The h_2 index computed from the LES results is consistent with the DNS ones, denoting a maximum difference of 0.9 m/s^2 with the coarse mesh in the zone corresponding to the aneurysm. This latter zone represents the region with the higher values of the h_2 index, i.e. about 2% respect to 1% at the aortic arch, thoracic, and descending aorta, and 0.5% at the ascending aorta. Since the h_2 index indicates the total amount of helical flow in the fluid domain without considering the direction of the rotation of the fluid structures [115], we argue that the aneurysmatic zone is the region characterized mostly by helical flow, according to literature [116].

5.1.4 Parameter Estimation of the LES model

After discussing the comparison between DNS and LES, now we focus on the second aim of this work, consisting in proving with three patient-specific geometries that the Smagorinsky model is able to suppress the backflows instabilities. In particular, we demonstrate that the Smagorinsky model well

controls the backflows instabilities by a proper selection of the Smagorinsky coefficient, even involving coarser meshes than the one necessary for DNS.

To the best of our knowledge, no study investigated the parameter estimation of the Smagorinsky model in relation to the mesh size, the Reynolds number, and the flow features, when Neumann boundary condition are imposing. Indeed, among the studies cited in the state of the art at the beginning of the chapter, the values of the LES coefficient is not reported [17], or patient-specific Neumann boundary conditions are not prescribed [17], [94], or the the default value of the LES parameter is used with very fine meshes, without analyzing the flow features [69], [93]. Only Xu et al. [18] performed an extensive sensitivity analysis of the role of the LES parameter; however, the authors used a particular LES scheme (i.e. Evolve-Filter-Relax scheme with deconvolution filter), implemented in the open-source software LifeV and not included in the commercial one Ansys Fluent.

Since a sensitivity analysis on the parameter estimation of the Smagorinsky coefficient is missing in literature, we need to consider an empirical calibration. In Patient 1, we first set the default value in Ansys Fluent (i.e. $C_S = 0.1$) and then we increase its value until reaching the solution convergence for both the meshes used in the LES simulations. Table 5.4 reports the minimum value of the Smagorinsky coefficient found in each LES simulation, in order to guarantee the convergence of the solution. Note that in Patient 1 the value of

	C_S	
	Coarse mesh	Fine mesh
Patient 1	0.20	0.20
Patient 2	0.34	0.39
Patient 3	0.36	0.40

Table 5.4: Minimum values of the Smagorinsky coefficient to attain stability in each patient-specific simulation with coarse and fine mesh.

the Smagorinsky coefficient with both the meshes is lower than the other two patients (i.e. differs by 0.14 and 0.16 with the coarse mesh, and by 0.19 and 0.2 with the fine mesh for Patients 2 and 3, respectively). Moreover, while in Patient 1 the Smagorinsky coefficient remains constant in both the meshes, in Patients 2 and 3 it increases by refining the mesh. We try to find a relation between the flow characteristics and the value of the Smagorinsky coefficient in order to explain the differences found in the Smagorinsky parameter estimation obtained. Figure 5.14 shows the flow rate in each inlet and outlet of the three patients considered, highlighting the amount of antegrade and retrograde flow, the computed ejection fraction and the peak backflow. Patient 1

is characterized by very few backflows at the inlet and in all the outlets (the largest amount of retrograde flow is 0.58 ml in the outlet corresponding to the descending aorta), and thus a high ejection fraction (the lowest is 95.3% in the outlet corresponding to the left subclavian artery). Patient 2 presents backflows only in two outlets (i.e. brachiocephalic trunk and left subclavian artery); however in these two outlets the ejection fraction is particularly low, reaching 74% in the left subclavian artery. In Patient 3, retrograde flow occurs at the inlet and all the outlets; in particular, the amount of retrograde flow corresponds to 11.21 ml with the ejection fraction of 87% at the descending aorta. Thus, lower ejection fraction occurs in Patient 2 and lower retrograde flow in Patient 3. Therefore, from the comparison between the Smagorinsky coefficient estimation and the flow features of the patients considered, it seems that the more backflows there are, the more it is necessary to increase the value of the Smagorinsky coefficient to obtain the solution convergence. In particular, the amount of retrograde flow seems more relevant in the choice of the Smagorinsky coefficient with respect to the ejection fraction. Finally, looking at differences between the meshes of each patient, the Smagorinsky coefficient becomes more sensitive to the mesh size when a large amount of retrograde flow occurs.

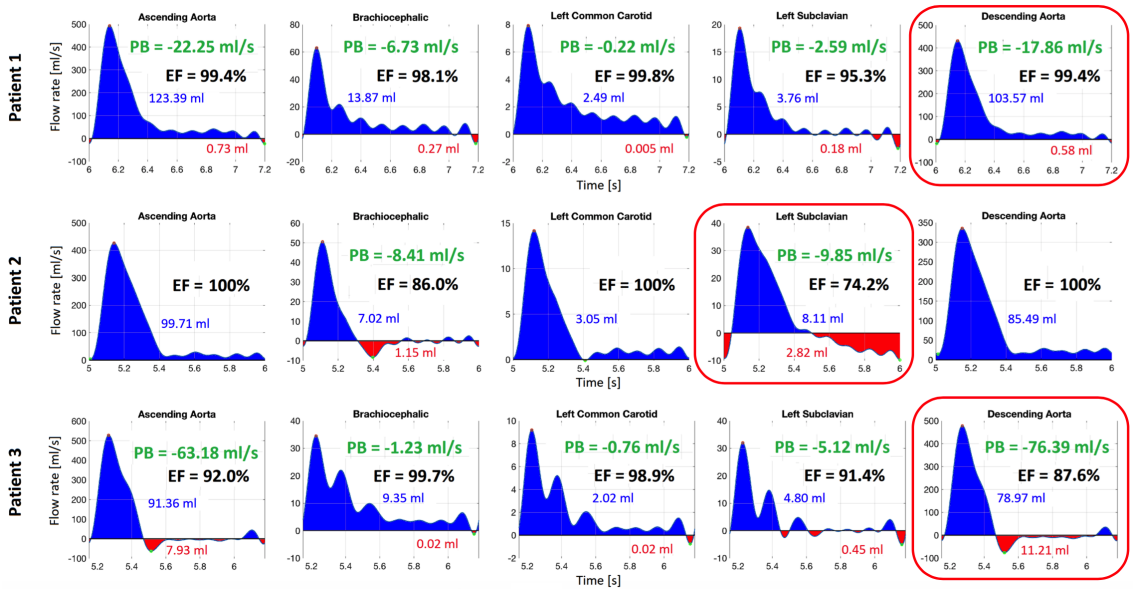

Figure 5.14: Comparison of the computed flow rate at each inflow and outflow boundary over time. The amount of antegrade (in blue) and retrograde flow (in red), the computed ejection fraction (EF) and the peak backflow (PB) are reported.

5.1.5 Conclusions

In this study we analyze the advantages brought by a LES model, i.e. the Smagorinsky model, in patient-specific aortic simulations, comparing it with the DNS and studying how to calibrate the coefficient in relation to the flow rate and the mesh size. In particular, we consider 3 patients with aortic aneurysms: one with aortic arch aneurysm (i.e. Patient 1), the other two with thoracic aneurysms (i.e. Patient 2 and 3). We chose Patient 1, characterized by a simpler geometry and a more organized flow, to perform both the DNS and LES simulations (using two coarser meshes than the one used for the DNS). From the qualitative and quantitative analysis, we observe that the LES model provides accurate results with coarser meshes and therefore with lower computational costs. Indeed, the LES takes about 3 and 7 days to calculate the solution with the coarse and fine mesh, respectively, compared to the 14 days of the DNS. Moreover, by a proper calibration of the Smagorinsky coefficient, the LES model is able to control the numerical instabilities that can be generated when Neumann boundary conditions are imposed in presence of backflows. To the best of our knowledge, this is the first study that provides instructions for both performing accurate patient-specific simulations and stabilizing the backflow instabilities, using coarser meshes than DNS and the Smagorinsky model implemented in the simple commercial software Ansys Fluent setting. In particular, no study has analyzed how to estimate the Smagorinsky coefficient in relation to the flow rate and the mesh size. Comparing the flow features of the three patients considered and the values of the Smagorinsky coefficient obtained to achieve convergence, we noticed that the value of the Smagorinsky coefficient must be set with higher values in such patients with a significant amount of retrograde flow in ascending aorta and/or at the supra-aortic branches and/or descending aorta (i.e. the inlet and outlets of the computational domain). Moreover, in presence of a large amount of retrograde flow, the value of the Smagorinsky coefficient must be increased by about 0.5 in the fine mesh than the coarse one adopted for the same patient under consideration. Conversely, the results obtained with Patient 1, characterized by low amount of retrograde flow and high value of ejection fraction ($> 95\%$) on the inlet and all the outlets, suggest that the Smagorinsky coefficient is less sensitive to the size of the mesh. Indeed, the same value of the Smagorinsky coefficient, $C_S = 0.2$, has been found to achieve convergence for both the meshes adopted for Patient 1.

Chapter 6

Conclusions and Future Research

In the last two decades mathematical and numerical modeling of cardiovascular system has been progressively developed and used in medical investigation, thanks to high performance computing hardware and a better accuracy of mathematical models and numerical methods. The use of sophisticated simulations provide support for both basic medical research and clinical practice in the preliminary phase of therapeutic and/or surgical treatment. For example, they could be extremely useful in predicting aneurysm progression and its risk of rupture, helping the understanding of local hemodynamic, and optimizing the design of a stent or a particular implant. Moreover, numerical simulations are less invasive than in vivo experiments and potentially more accurate and flexible than in vitro ones.

In this context, the aim of this thesis consists in providing a set of tools and a clear workflow to perform accurate and efficient simulations with acceptable computational cost on healthy and especially diseased aortic patients, in which higher Reynolds number occurs.

In the following, specific conclusions are drawn for each presented chapter, except for Chapter 4 that is mainly theoretical.

Chapter 2 focuses on the study, implementation, and validation of lumped parameter models, particularly useful to impose reliable boundary conditions, coupling it with 3D models. Moreover, they could be used as a first tool to assess the parameter estimation of a 0D model, selected, for example, as boundary condition of a 3D model. The qualitative comparison between the results of 0D and 3D-0D models proved the consistency of the 0D model. Indeed, the lumped parameter models provide reliable results with an accurate selection and parameter estimations of the various segments in which the original 3D computational domain should be divided. The main advantage of the 0D models is the lower computational cost than 3D models.

Chapter 3 treats a coupled 3D-0D model of thoracic aorta, including coro-

nary arteries, to investigate the impact of transcatheter aortic root repair procedure on coronary perfusion. To the best of our knowledge, this work is the first computational study on a new endovascular procedure consisting of the simultaneous replacement of the aortic valve, the aortic root and the proximal part of the ascending aorta. We both proved that the deployment of the endografts is feasible and also analyzed the coronary flow, concluding that the proposed configuration does not significantly affect the coronary perfusion.

Chapter 5 is based on an application of the coupled 3D-0D and LES model to patient-specific thoracic aortic simulations. The main novelty consists in providing the instructions for both performing accurate patient-specific simulations and stabilizing the backflow instabilities, using coarser meshes, and consequently lower computational cost, than DNS. In particular, the LES simulation takes about 3 and 7 days to calculate the solution with the coarse and fine mesh, respectively, compared to the 14 days of the DNS. Concerning the LES parameter estimation, the Smagorinsky coefficient must be set with higher values in such patients with a significant amount of retrograde flow at the computational inlet and/or outlets. Moreover, in order to control the backflow instability and achieve numerical convergence, our results suggest that: (i) the value of the Smagorinsky coefficient must be increased by about 0.5 in the fine mesh with respect to the coarse one adopted for the same patient under consideration, in presence of a large amount of retrograde flow; (ii) the Smagorinsky coefficient is less sensitive to the size of the mesh, when low amount of retrograde flow and high value of ejection fraction ($> 95\%$) occur. In the latter case, a value of $C_S = 0.2$ seems to be sufficient to suppress the numerical instabilities.

Appendix 1 concerns a further application of CFD simulations for popliteal arterial aneurysms in order to evaluate the impact of leg bending and geometrical features on the local hemodynamic of two patients treated with endovascular stent-graft placement. The results suggest that the overlapping of the stent-grafts induces a severe discontinuity of lumen diameter, dividing the region treated with endovascular stent-graft into two zones. The first one, i.e. the proximal part, where thrombosis is located, is characterized by low tortuosity, low velocity, low helicity, low TAWSS, and high OSI. The second one, i.e. the distal part, presents higher tortuosity, higher velocity, higher helicity, higher TAWSS, and lower OSI. Leg bending induces significant hemodynamic differences compared to the straight leg configuration for both the patients under consideration. In particular, our results show a significant variation of tortuosity between the two configurations, accentuated in the distal stent zone, where the tortuosity is greater in the bent-leg configuration. Finally, the helical form of intra-stent thrombosis suggests the involvement of flow helicity in the onset

and progression of thrombosis.

6.1 Future Work

The main future developments for the present work consist in the implementation of more accurate boundary conditions for the coupled 3D-0D models and a deeper investigation on the best LES model to adopt. In particular, a lumped parameter model able to simulate the cardiac injection flow from the heart to ascending aorta could be implemented and imposed as inlet boundary condition of coupled 3D-0D model. According to Bakel et al. [38], the heart model should include diodes and inductors to represent the mitral and the aortic valves, a pressure source representing the left atrial pressure, and a volume-tracking pressure chamber representing the left ventricle. For example, by imposing this 0D model instead of Dirichlet velocity boundary condition at the inlet, we no longer need the MRI data of the specific patient.

Finally, a large cohort of patients should be involved in order to validate our conclusions. In particular, we are interesting in finding the relation that links the model parameters of LES together with the mesh size, the Reynolds number, and the amount of retrograde flow.

Chapter 7

Appendix 1

We now focus on a particular application of CFD simulations, not related to multiscale models, but of clinical relevance. Indeed, it is part of the PERFEKT project led by Dr. B. Pane, Dr. G. Salsano (San Martino Hospital, Genova) and Prof. M. Conti, and funded by the Italian Ministry of Health. The study deals with intra-stent thrombotic apposition that can occur during follow-up in patients undergoing endovascular treatment for popliteal arterial aneurysm.

7.1 CFD simulations for popliteal arterial aneurysms

Popliteal arterial aneurysms (PAA) are common peripheral aneurysms. Although in the last few years endovascular treatment of the femoro-popliteal artery (FPA) has become a valuable therapeutic option, its efficacy remains controversial due to the relatively high rate of complications, such as stent occlusion, intra-stent thrombosis or even stent fracture [118]. All these drawbacks could be related to the intrinsic morphology of the FPA segment that presents unique characteristics in terms of extreme mobility and biomechanical forces and severe loading conditions due to repetitive leg flexion during daily activities [119]. If on the one hand the stent fracture can be traced back almost exclusively to repeated bending of the stented leg, on the other the mechanisms that lead to intra-stent thrombosis are not fully understood even if hemodynamics is suspected of playing an important role in this process [120].

Computational fluid dynamics (CFD) analyses are increasingly exploited to quantify the blood flow inside the FPA and evaluate the changes on hemodynamic patterns due to the combination of endovascular stenting and leg movements. Blood flow patterns, and in particular low shear stress, prominent secondary flows or huge variations of arterial wall shear stress (WSS) are indeed known to correlate with pathological conditions [121]-[123], as briefly

resumed in the following.

First studies investigating flow patterns in patient-specific superficial femoral arteries date back to 2006 by Wood et al. [123], who combined magnetic resonance imaging and CFD to assess the relation between curvature and tortuosity of superficial femoral arteries and flow patterns as function of sex and age. More recently, the study of Desyatova et al. [124], who investigated the effects of aging on mechanical stresses, deformations, and hemodynamics, has identified the popliteal artery as the location with greatest intramural stresses along the leg arteries. Moreover, the association of vessel restenosis with hemodynamical markers derived from blood flow has been investigated by Gogkol et al. [120], in patients undergoing endovascular treatment for peripheral artery diseases (PAD). However, the proposed work was based on vessel geometries reconstructed from 2D angiographic images thus idealizing the lumen cross-sections. This limitation was overcome by Colombo et al. [125], who presented a fully patient-specific computational framework based on geometric reconstructions from Computed Tomography (CT) images and boundary conditions taken from Doppler ultrasound images. However, despite the proposed innovations, only the straight-leg configuration has been studied, thus neglecting the analysis of the effects of leg bending on the geometry and hemodynamics of the stented area. In a more recent study led by Colombo et al. [126], knee flexion and complete movement of walking have been assessed in an idealized model of FPA. Finally, the impact of leg bending on geometrical and hemodynamic features have been investigated in our previous work, where patient-specific CFD simulations have been performed on a single patient, using literature boundary conditions [19] and Newtonian model for blood rheology. Although it is known that blood is a non-Newtonian fluid [127], literature review about CFD modeling of the actual rheology of blood is controversial. While the assumption of treating blood as a Newtonian fluid is widely accepted [128], it still represents a pivotal issue in case of small or mid arteries. Moreover, while some studies highlighted the importance of the non-Newtonian rheology [129], others found that the use of a Newtonian blood model represents a good approximation [130], [131]. In particular, focusing on modeling of the FPA, most of the studies [120], [123], [35] assumed a constant viscosity, even if Colombo et al. [125] adopted the Carreau model to describe the non-Newtonian viscosity of blood.

According to the literature, CFD provides a useful tool for understanding and predicting disease progression and hemodynamic-related post-stent complications. However, literature studies about patient specific CFD of popliteal stenting are scarce; in particular, many of them involve idealized geometry [120], [126] and literature boundary conditions [120], [19], without any infor-

mation regarding the follow-up intra-stent thrombosis. Moreover, morphological variations during knee flexion in the FPA could significantly influence the local hemodynamic [126], [19]. To the best of our knowledge, a complete computational study including all these aspects is still missing.

Based on such considerations, we performed patient- specific CFD simulations in order to assess the impact of leg bending and the interplay among geometrical features on the local hemodynamic of two patients treated with endovascular stent-graft placement for PAA, experiencing intra-stent thrombosis. Moreover, we deepened and improved our previous study [19] by investigating the impact of the different inlet boundary conditions on the solution (in a similar way to Hua et al. [132]), and assessing the hypothesis of non-Newtonian behavior of blood (using the Carreau model), in comparison with the usual approximation of blood as a Newtonian fluid.

7.2 Patient-Specific Geometries and CFD Setting

Signed informed consent was obtained from the patients and all procedures were performed in accordance with the Declaration of Helsinki and submitted to the local institutional medical ethics committee. Two patients with PAA and endovascularly treated at Vascular and Endovascular Surgery Unit of University Hospital of Genoa were enrolled for an imaging study with double CT acquisition at straight- and bent-leg. More details of the imaging acquisition protocol were provided in a previous study [147].

A 78-year old man (Patient 1) with PAA in the left leg was successfully treated with two Viabahn devices (W.L. Gore & Associates, Flagstaff, AZ, USA) sized 9 mm $\times$ 150 mm (proximal stent) and 7 mm $\times$ 150 mm (distal stent). At 12 months follow-up, post-operative CT showed partial stent thrombosis in the transition zone between the two partially overlapped devices. The second enrolled patient (Patient 2) was a 68 year-old man treated in the left leg for PAA with two Viabahn devices sized 10 mm$\times$100 mm (proximal stent) and 9 mm $\times$ 150 mm (distal stent). In this patient, intra-stent thrombosis was revealed already by 1 month follow-up CT scan.

Postoperative CT images were anonymized and transferred to a workstation for image processing. Segmentation of the vessel lumen from the femoral artery bifurcation to the popliteal artery bifurcation, intra-stent thrombosis, leg bones, and the implanted stent-graft(s) was performed by means of Vascular Modeling ToolKit (VMTK) libraries [134]. A surrogate pre-thrombotic model of the lumen was derived by virtually removing the thrombosis during

the image segmentation in order to correlate hemodynamic with thrombosis onset. Rigid registration of bent-leg structures on their corresponding straight counterparts was automatically performed by means of the Iterative Closest Point algorithm implemented in VMTK. Centerline vessel was automatically extracted, smoothed and resampled by 0.5 mm by means of VMTK libraries [135]. Centerline tortuosity was then computed: it represents an important factor in different cardiovascular diseases, i.e., atherosclerosis, abdominal aortic aneurysm, and, in particular, in thrombus initiation [136]. Tortuosity T is measured as follows: given the centerline length (L) and the shortest distance between the two centerline endpoints (ED), $T = L/ED - 1$; therefore, with this definition, the tortuosity of a straight line is 0.

Transient CFD analyses were performed using Intel Xeon W-2123 computing workstation (3.6 GHz, 32 GB RAM) with the commercial software FLUENT (v.19.2, ANSYS Academic Research). We considered the two patients in both straight- and bent-leg configurations in order to assess the effects of leg bending and the impact of inlet boundary condition on the flow solution. Uniform meshes were generated using VMTK, ranging from 648879 and 1471373 number of tetrahedral elements, according to the previously performed mesh sensitivity analysis. In particular, the mesh was refined until the difference in the luminal area exposed to TAWSS < 0.62 Pa between successive grids was $< 1\%$. Geometry and boundary conditions are the main features affecting the CFD simulations in hemodynamics. We evaluated the impact of the inlet boundary conditions on the numerical solution by considering two literature waveforms (boundary conditions A and B) with three different scenarios, i.e., with or without flow extension and varying the velocity profile (flat or parabolic). In particular, the flow extensions that we used in the simulations have been chosen in order to reduce the effect of the arbitrary choice of the velocity profile. They were modeled using VMTK, with a length corresponding to 3.5 times the dimension of the inlet diameter, according to Colombo et al. [125]. The following inlet boundary conditions were tested:

- A1: velocity inlet waveform taken from Wood et al. [123] (see Figure 7.1) with a flat velocity profile.
- A2: equivalent to the boundary condition A1with the flat velocity profile set at the flow extension of the inlet of the patient-specific models (see Figure 7.2).
- A3: equivalent to the boundary condition A2 with a parabolic velocity profile set at the inlet of the flow extension.
- B1: inflow waveform taken from Nichols et al. [36] (see Figure 7.1) with a flat velocity profile.

- B2: equivalent to the boundary condition B1 but with the flat velocity profile set at the inlet of the flow extension.
- B3: equivalent to the boundary condition B2 but with a parabolic velocity profile set at the inlet of the flow extension.

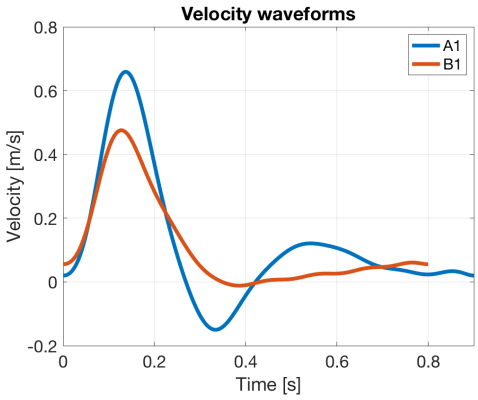

Figure 7.1: Inlet velocity waveforms in m/s colored according to: the literature inlet velocity taken from Wood et al. [123] and imposed at the inlet boundary in scenario A1 (and analogously in A2, A3); the inlet velocity computed from the literature inflow taken from Nichols et al. [36] and used in scenario B1 (and analogously in B2, B3).

Hence, we are imposing the same velocity waveform when using the boundary conditions A1, A2, and A3, while the same inflow waveform when adopting the boundary conditions B1, B2, and B3, thus implying slightly different inlet velocity waveforms according to the inlet radius of our computational domain. For example, in Figure 7.1 the velocity waveforms corresponding to the boundary conditions A1 (equivalent to A2, A3) and B1 for Patient 1 in straight-leg configuration are represented. In particular, we extracted the values of the velocity waveform, taken from [123] (and analogously for the inflow waveform [36]), using the software WebPlotDigitizer 4.4 (WebPlotDigitizer). Then, the data obtained by the literature waveform were interpolated with an 8^{th} order Fourier series by using the Curve Fitting App, given by the software Matlab R2018a (The Mathworks Inc.). The transient inlet velocity waveform was defined in FLUENT by the meaning of a user defined function (UDF). Therefore, the inlet boundary conditions with a flat velocity profile (i.e., scenarios A1, A2, B1, B2) were given by

$$u_{flat} = a_0 + \sum_{i=1}^{8} [a_i \cos(i\omega t) + b_i \sin(i\omega t)], \tag{7.2.1}$$

	Infinite shear rate viscosity (kg/m s)	Zero shear rate viscosity (kg/m s))	Time constant λ (s)	Power low index n
Value	0.0035	0.056	3.313	0.3568

Table 7.1: Fundamental frequency used in UDF inlet waveform - equation (7.2.1); parameters of the Carreau model - equation (7.2.2).

where ω is the fundamental frequency, t the simulation time, and a_0, a_i, b_i for $i = 1, 2, ..., 8$, the values of the Fourier parameters given by the Curve Fitting App. The inlet boundary conditions with a parabolic velocity profile (i.e., scenarios A3 and B3) were prescribed as

$$u_{parabolic} = 2u_{flat}\left[1 - \left(\frac{r}{R}^2\right)\right],$$

where r denotes the distance between a point on the constrained surface and the center of the surface, and R is the radius of the constrained surface.

The proposed six boundary conditions were imposed on the patient-specific model of the two patients for both straight- and bent-leg configurations, therefore we performed 24 simulations (six boundary conditions for two patients for two leg configurations).

Firstly, blood was assumed as an incompressible and Newtonian fluid, with 1060 kg/m^3 density and 0.0035 $Pa\ s$ viscosity [35]. Then, in order to evaluate the impact of the non-Newtonian behavior of blood, we chose the boundary conditions A1 and B1, i.e., two velocity waveforms with a flat velocity profile, running 8 simulations (two boundary conditions per two patients per two leg configurations). The viscosity was modeled using the Carreau model described in the following equation:

$$\eta = \eta_\infty + (\eta_0 - \eta_\infty)(1 + \lambda^2\dot{\gamma}^2)^{\frac{n-1}{2}}, \tag{7.2.2}$$

where η is the effective viscosity, η_∞ the infinite shear rate viscosity, η_0 the zero shear rate viscosity, λ the natural time, $\dot{\gamma}$ the shear rate, and n the power law index. The parameter values were set according to Quanyu et al. [137] and listed in Figure 7.1. In each simulation we prescribed the no-slip condition on the wall of the artery. Regarding the outlets, the following flow splits were assigned as percentages of the FPA output, according to Crawford et al. [138]: the anterior tibial artery 20%, posterior tibial artery 40%, and peroneal artery 40%. The flow was assumed in laminar regime since the maximum Reynolds number among all the simulations was 1328 at systolic peak (occurring with A1, A2, and A3 conditions). Semi-implicit method for pressure linked equations (SIMPLE) was used to solve the Navier-Stokes equations. Second order

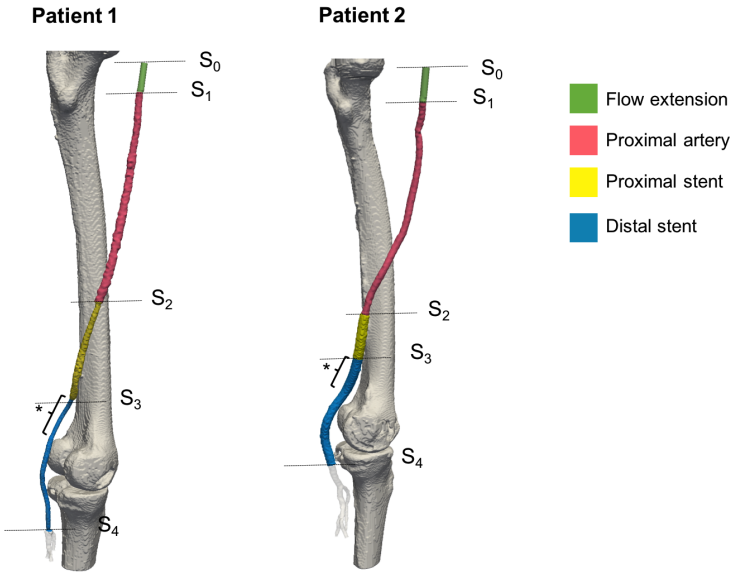

Figure 7.2: Femoro-popliteal artery of the two patients considered in the CFD simulations in the straight-leg configuration. Both are colored according to the flow extension, added to our computational domains in scenarios A2, A3, B2, B3, and to the three zones under investigation (proximal artery, proximal stent, and distal stent). Moreover, the sections considered in the post processing S_0,S_1,...,S_4 are represented. The region marked with asterisk denotes the overlapping zone of the two stents in both the patients.

scheme for both pressure and momentum spatial discretization was adopted. After a sensitivity analysis, a constant time-step size was set to 0.001 s and three cardiac cycles were performed for each simulation to guarantee the repeatability of solution.

In order to evaluate the impact leg bending on the local hemodynamics of FPA, with a focus on the stented and thrombotic regions, the FPA segments of both the patients were divided into 3 zones (see Figure 7.2): (1) proximal artery, i.e., lumen of the artery above the proximal end of the proximal stent (excluding the flow extension); (2) proximal stent, i.e., the lumen of the proximal stent, excluding the overlapping zone; (3) distal stent, i.e., the lumen of the distal stent including the overlapping zone. We performed both a qualitative and quantitative analysis comparing the results of the two patients in straight- and bent-leg configurations obtained from the CFD simulations. Firstly, to evaluate the impact of boundary conditions, we focused on the velocity streamlines, the vectors of velocity magnitude, and the velocity profiles at the following cross sections corresponding to: the flow extension inlet, S_0; FPA

inlet, S_1; proximal stent inlet, S_2; distal stent inlet, S_3; distal stent outlet, S_4 (see Figure 7.2). The velocity streamlines, the vectors of velocity magnitude, and the velocity profiles were reported at the systolic peak.

We computed the time-averaged wall shear stress (TAWSS) and oscillatory shear index (OSI), regarding the near wall flow features, and local normalized helicity (LNH) and helicity intensity (h_2 index), relating to the bulk flow. TAWSS and OSI were computed as follow:

$$TAWSS = \frac{1}{T}\int_0^T |WSS|\, dt,$$
$$OSI = 0.5\left(1 - \frac{|\int_0^T WSS\, dt|}{\int_0^T |WSS|\, dt}\right),$$

where T is the cardiac period and $|WSS|$ the norm of the WSS vector. WSS is defined as follows

$$WSS = \boldsymbol{\sigma} n - [(\boldsymbol{\sigma} n) \cdot n]n,$$

where $\boldsymbol{\sigma}$ is the Cauchy stress tensor and n the normal vector to the surface. In particular, in an incompressible fluid, the Cauchy stress tensor is defined as follow

$$\boldsymbol{\sigma} = \eta(\nabla \mathbf{u} + \nabla \mathbf{u}^T) - p\mathbf{I},$$

where $\mathbf{u}$ is the velocity vector, p the pressure, and $\mathbf{I}$ the identity matrix. TAWSS plays a pivotal role in the development of arterial stenosis and in prediction of the risk of wall rupture and thrombus deposition. According to Malek et al. [109], we calculated the luminal surface exposed to low and high values of TAWSS, i.e., ranging between 0 and 0.4 Pa and above 1.5 Pa, respectively. OSI measures the temporal oscillations of the WSS. In particular, high values of OSI denote sites where the WSS deviates from the main flow direction in a large fraction of the cardiac cycle [139]. According to Gokgol et al. [120], luminal area exposed to high OSI (> 0.3) was computed. Regarding the bulk flow, qualitatively, we computed the LNH, which corresponds to the cosine of the angle formed between the vorticity vector and the velocity vector

$$LNH = \frac{(\nabla \times \mathbf{u}) \cdot \mathbf{u}}{|\nabla \times \mathbf{u}| \cdot |\mathbf{u}|} = \cos\alpha,$$

where α is the angle formed between the vorticity vector $(\nabla \times \mathbf{u})$ and velocity vector $\mathbf{u}$. It is a measure of the alignment/misalignment of the local velocity and vorticity vectors. LNH ranges from -1 to +1, and its sign indicates the direction of helical structures. Quantitatively, we computed the h_2 helicity,

that is an index regarding the bulk flow: it is given by time-averaging the absolute value of the helicity [140]:

$$h_2 = \frac{1}{TV} \int_T \int_V |\mathbf{u} \cdot (\nabla \times \mathbf{u})| \, dV dt,$$

where V is the arterial volume. The h_2 helicity index expresses the helicity intensity in the fluid domain, irrespective of direction. Recalling that the helicity is defined by the spatial integral of the scalar product of the velocity and vorticity, we assume h_2 index has higher values in the fluid domain in which velocity and vorticity vectors are aligned.

7.3 Numerical results

Firstly, we reported the results obtained by the 24 simulations performed with constant viscosity. Figures 7.3 and 7.4 show the results of CFD simulations for the straight- and bent-leg configurations of both the patients in the six scenarios that have been tested (A1, A2, A3 and B1, B2, B3 in Figures 3 and 4, respectively), reporting streamlines, velocity profiles, and velocity vectors colored according to the velocity magnitude at the systolic peak. These two figures prove that only the imposed waveform at the inlet (taken from Wood et al. [123] or Nichols et al. [36]) significantly affects the solution. Indeed, each scenario has similar velocity profiles and contours in the cross-sections of the stented regions, by fixing the inlet waveform. Therefore, from now on we consider only the results relating to the scenarios A1 and B1 for both the patients in straight- and bent-leg configurations. However, the figures including all the scenarios relating to the Newtonian model are contained in the Supplementary Materials and Methods section.

Figure 7.5 highlights the arterial lumen colored according to low (ranging from 0 to 0.4 Pa) and high TAWSS (higher than 1.5 Pa). The results suggest that the distal part of the artery is exposed to high TAWSS in both straight- and bent-leg configuration with a limited influence of inflow boundary conditions; such a result is particularly evident in the case of Patient 1, while for Patient 2 the B1 scenario is resulting in physiological TAWSS in most of the whole artery for both configurations. Figure 7.6 shows the arterial lumen colored according to high OSI (> 0.3) is represented. High OSI are located for all the cases under considerations in the proximal part of artery irrespective to the adopted boundary conditions.

Helical blood flow structures developing into the endoprostheses are represented in Figure 7.7 using iso-surfaces of LNH at the systolic peak with a threshold of $\pm$ 0.25, according to Colombo et al. [125], for both the patients in

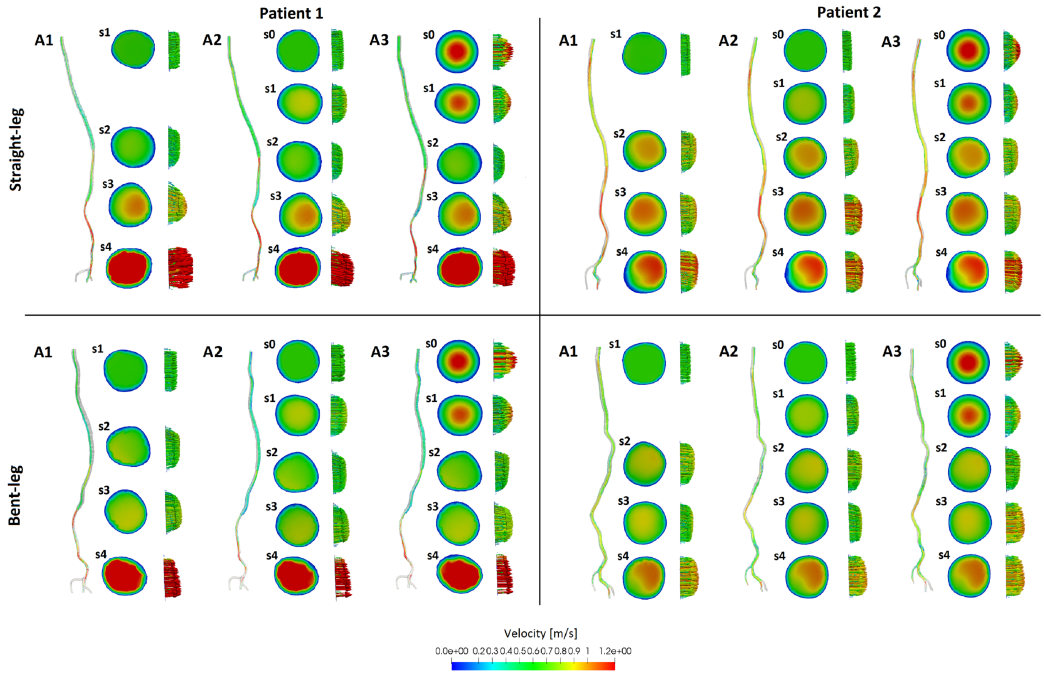

Figure 7.3: Streamlines, contours, and velocity vectors colored according to velocity magnitude at systolic peak, corresponding to the scenarios A1, A2 and A3, in both straight- and bent-leg configurations of the two patients.

straight-leg configuration, relating to the scenario A1. The results show that the bulk flow in the artery for both patients is characterized by two counter-rotating helical structures and in particular the helical shape of the thrombosis seems to flow the path of the negative LNH region.

Figure 7.8 reports the bar-plots of the value of h_2 index, tortuosity, and the percentage of luminal surface exposed to low and high TAWSS, and high OSI corresponding to each zone (proximal artery, proximal stent, and distal stent) for both the patients in straight- and bent-leg configurations. The results show that leg bending induces a difference of the computed hemodynamics indices for Patient 1 with both A1 and B1 boundary conditions. Indeed, a percentage difference above 50% between the two configurations is present for each hemodynamic quantity that we computed in all the tested scenarios, except for the percentage difference relating to the luminal area exposed to high OSI in Patient 2 (with a maximum percentage difference of 24% in the distal stent region). In particular, our results show a significant variation of tortuosity between the two configurations, accentuated in the distal stent zone, where the tortuosity is greater in the bent-leg configuration.

Finally, we treated the blood as a non-Newtonian fluid and we assessed

the results, comparing them with the previous analyses, obtained using the Newtonian model. Figure 7.9 shows the arterial lumen of both patients colored according to TAWSS magnitude, low (ranging from 0 to 0.4 Pa) and high TAWSS (higher than 1.5 Pa), based on both the Carreau (non-Newtonian) and Newtonian models. Figure 7.9 represents only the results relating to the scenario B1, which provides greater differences between the two models under consideration and allows us a wider discussion, as we will introduce in the next section. Figures 7.10 and 7.11 represent the bar-plots of the value of h_2 index, and the percentage of luminal surface exposed to low and high TAWSS, and high OSI corresponding to each zone (proximal artery, proximal stent, and distal stent) for both the patients. In particular, Figure 7.10 refers to the straight-leg configuration, while Figure 7.11 to the bent-leg one.

7.4 Hemodynamic and Clinical Assessment

In this study, we have evaluated the local hemodynamic and the interplay among geometric features in two patients endovascularly treated for PAA,

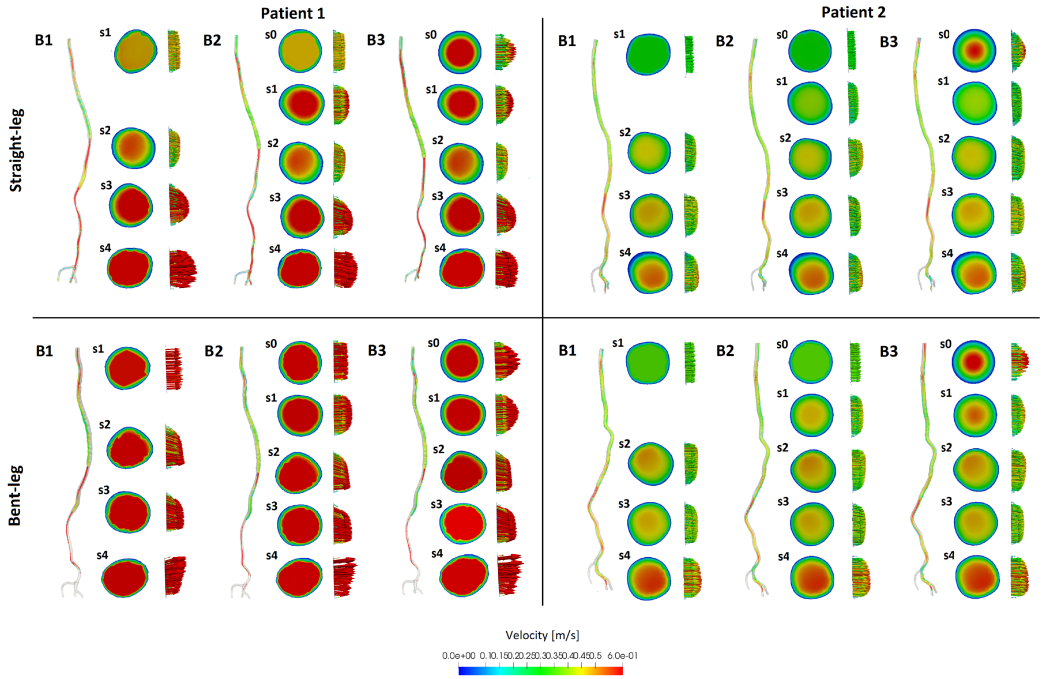

Figure 7.4: Streamlines, contours, and velocity vectors colored according to velocity magnitude at systolic peak, corresponding to the scenarios B1, B2, and B3 in both straight- and bent-leg configurations of the two patients.

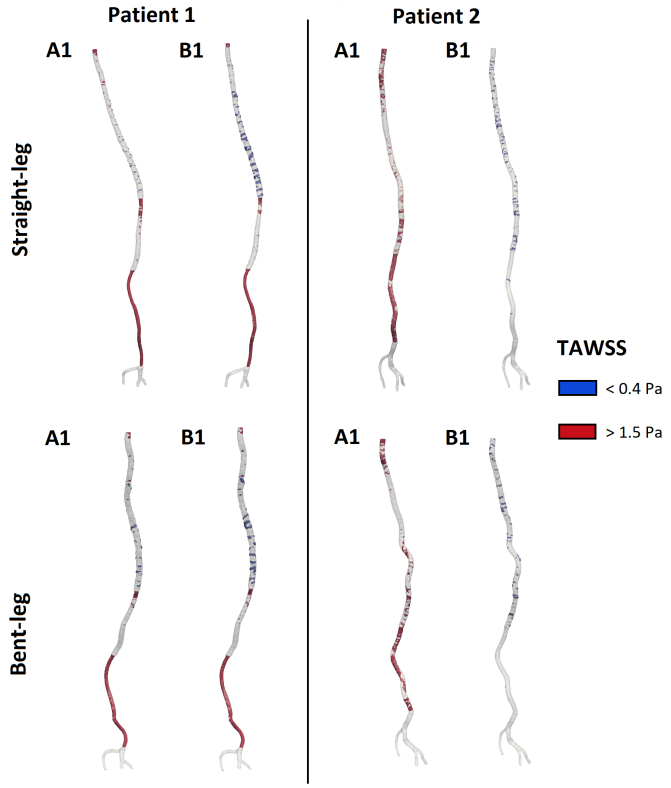

Figure 7.5: Arterial lumen colored according to low (< 0.4 Pa) and high (> 1.5 Pa) TAWSS in both straight- and bent-leg configurations of the two patients

who experienced intra-stent thrombosis during follow-up. In particular, the role of leg bending on the local hemodynamic was elucidated by modeling both straight- and bent-leg configurations. Focusing on the velocity magnitude, Figures 7.3 and 7.4 show a higher flow velocity in the distal stent region than to the proximal one, due to the luminal narrowing given by the overlapping of the two stents-grafts. As we already pointed out, the results suggest that the different inlet velocity profiles used in the simulations slightly affect the numerical solution, conversely to the determinant role of the prescribed inlet waveform. In order to obtain reliable results of clinical significance, patient-specific inflow waveforms would be very useful in understanding the hemodynamic behavior. However, our geometrical study shows velocity sensitivity, i.e., velocity magnitude variations between the two patients occur along the two FPAs by fixing a velocity inlet (i.e., scenario A or B). Although the behavior of stented FPAs has already been investigated in the literature [125], to date there is still no information on the different response between the various portions of the stented artery itself. Figure 7.8 suggests that the overlapping of the stent grafts seems

to induce a severe discontinuity of lumen diameter, dividing the region treated with endovascular stent-graft in two zones: (1) the proximal part, where thrombosis is located, it is characterized by low tortuosity, low velocity, low helicity, low TAWSS, and high OSI; (2) the distal part that presents higher tortuosity, promoting higher velocity, higher helicity, higher TAWSS, and lower OSI. In particular, by focusing on the tortuosity of the vessel (see Figure 7.8 at the bottom), the stented FPA respects the behavior that we would have expected, when considered in its entirety, i.e., increased tortuosity values with leg bending. Analyzing the stented area by portions, we have found that in both patients the tortuosity increases from the proximal artery region to the distal one; this result matches the findings of Wood et al. [123], who performed CFD simulations in the superficial femoral artery of 9 healthy men and 9 healthy women, showing that tortuosity was significantly greater for men than women, but the highest values were found in the most distal segment, regardless of sex. Then, when considering the comparison between straight- and bent- leg configuration, we observed that in both patients proximal vessel and distal

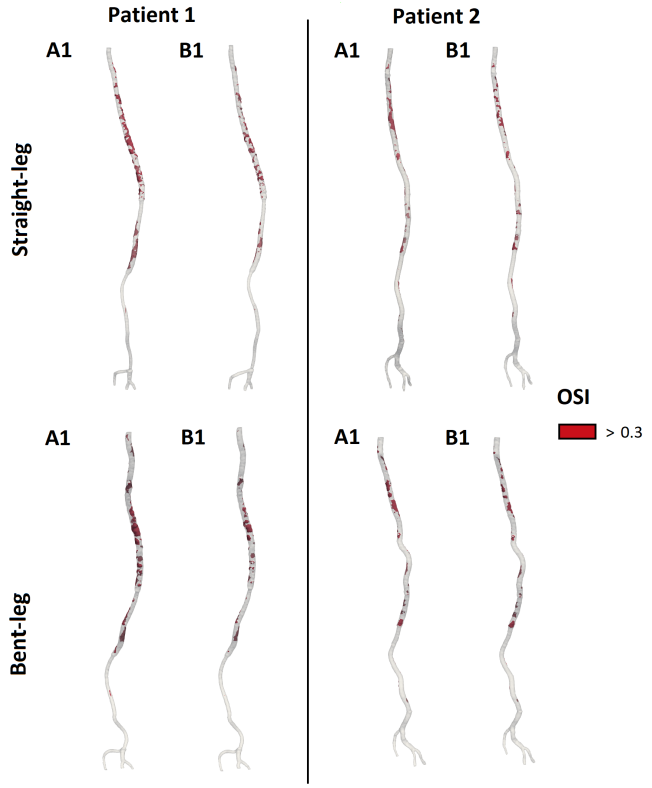

Figure 7.6: Arterial lumen colored according to high OSI ($>$ 0.3) in both straight- and bent-leg configurations of the two patients.

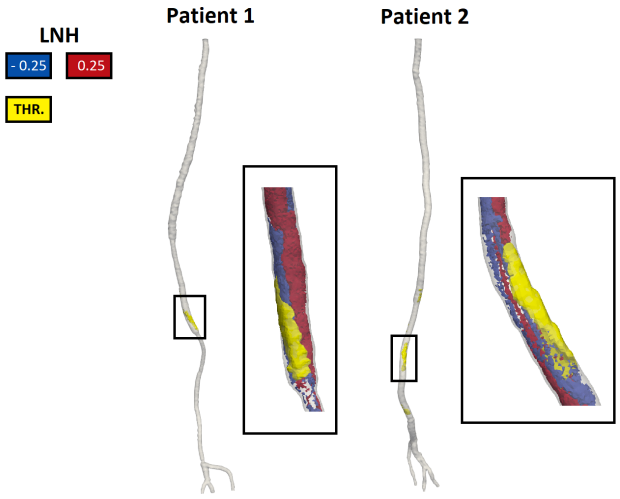

Figure 7.7: Femoro-popliteal artery and three zoom views of the lumen (rotating clockwise) of both the patients in straight-leg configuration: the area where the thrombosis is localized is highlighted by a black box. Moreover, blood flow helicity is represented: in blue the flow with negative LNH and in red the flow with positive LNH.

stent segments tortuosity increases with leg bending. However, the proximal stent, characterized by its larger diameter, slow velocity, low TAWSS, and low helicity, straightens with leg flexion. This area is also the one in which thrombosis was found in both patients, confirming that the formation of thrombosis is linked to a combination of both hemodynamic and geometric factors. Hence the importance of conducting the analyses by investigating the stented FPA not only in its entirety but by dividing it into the various portions, in order to be able to identify areas more at risk of thrombosis. The role of low TAWSS in thrombotic regions has been previously corroborated in literature. Boyd et al. [141] showed a correlation between regions of low WSS, where flow recirculation predominated, and thrombus deposition, by performing CFD simulations in 7 abdominal aortic aneurysms. The luminal area exposed to low TAWSS and high OSI in the proximal zone is greater in Patient 1 than in Patient 2 (see Figure 7.8), suggesting that patient-specific geometrical features also affect the near wall flow features.

Regarding the bulk flow, our results suggest that intra-stent thrombosis is located in the region where the intensity of helicity is low (see Figure 7.8). The fundamental role of helical (or swirling flow) in the prevention of thrombosis and disease progression has been confirmed in many literature studies [142]-

[144]. In particular, Morbiducci et al. [143] also presented an inverse relation between helical flow and OSI evaluating four bypass geometries in ascending aorta, according to our results. Moreover, our results denote that the spiral shape of thrombosis matches the path of the negative LNH region; this is more evident in Patient 1 (Figure 7.7). Figure 7.7 refers only to scenario A1, but an analogous pattern of the LNH was found using the boundary condition B1. It is hard to formulate a conclusion to explain this result; given the limited number of analysed patients, further analysis involving a cohort of patients should be investigated in order to provide more information to elucidate this observation.

From our results we found that the study in both straight- and bent-leg

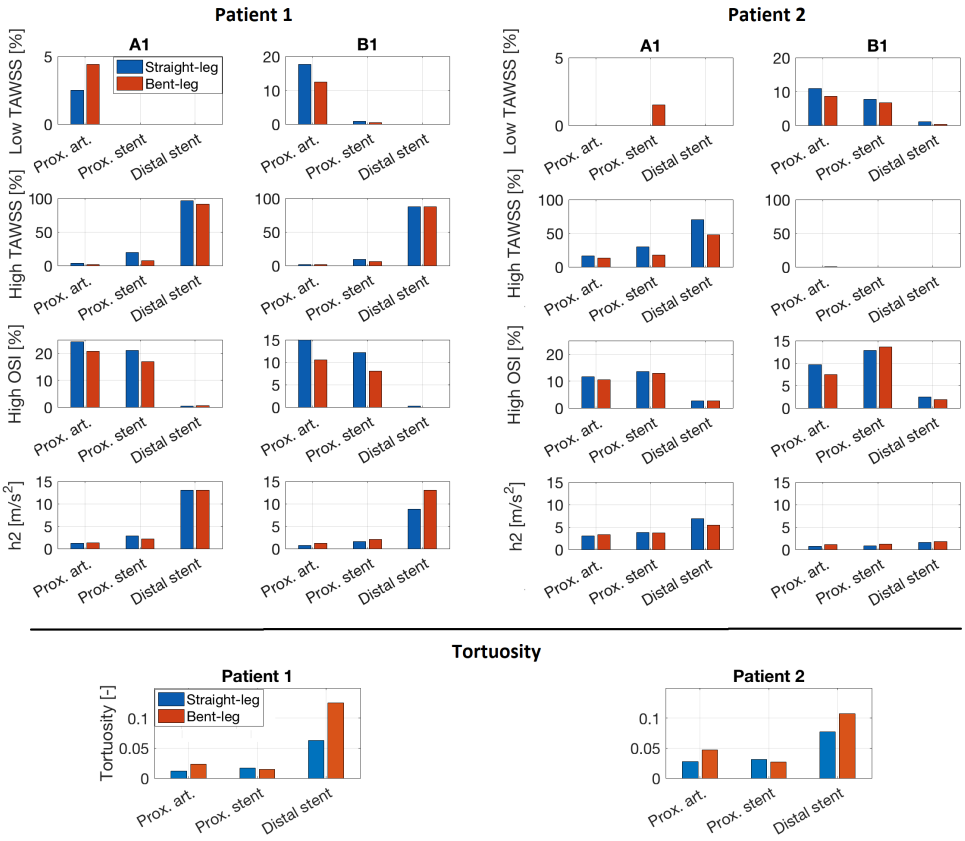

Figure 7.8: Bar plot of tortuosity, helicity (h_2 index), and percentage of luminal area exposed to both low (< 0.4 Pa) and high (> 1.5 Pa) TAWSS, respectively, and high OSI (> 0.3). The data are reported for the three zones under investigation (proximal artery, proximal stent, and distal stent) of the two patients in both leg configurations, corresponding to scenarios A1 and B1.

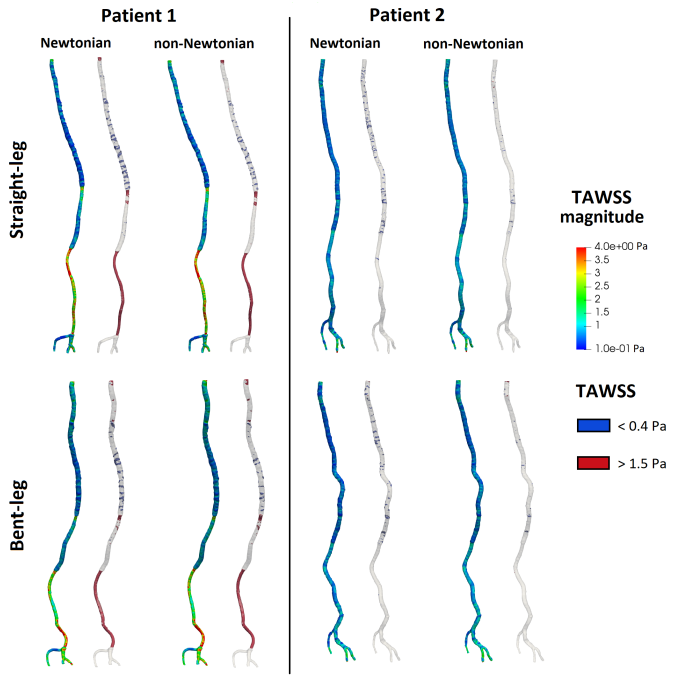

Figure 7.9: Arterial lumen colored according to the TAWSS magnitude, low (< 0.4 Pa) and high TAWSS (> 1.5 Pa) in both straight- and bent-leg configurations of the two patients. The TAWSS values represented refers to the scenario B1.

configurations is crucial in understanding and assessing the numerical results in stented arteries, given the increase of the tortuosity of the distal part of the artery due to the leg bending. Our findings match with Wensing et al. [145], who highlighted the importance of considering the impact of knee flexion in femoral and popliteal arteries, showing increasing tortuosity in bent-leg configuration of 22 healthy volunteers. Moreover, the increase of tortuosity in leg bending implies a reduction of the blood velocity in each scenario that we assumed for both patients (see velocity streamlines and contours represented in Figures 7.3 and 7.4).

The alternate bending of the legs is known to influence the mechanical solicitation of the stent [146], the shape of the artery [147], and the local hemodynamics [126] but its role in the thrombosis onset and progression is still unknown. From our results, it is evident that leg bending increases the tortuosity of the distal stent segment, which combined with an overall blood flow velocity, exacerbate the difference between the distal and proximal part of the stented region, with the latter more exposed to the risk of thrombosis (i.e., lower velocity, wider area of low wall shear stress, higher oscillatory shear stress,

and lower helicity). Such considerations are however hardly generalizable with data proposed by the present paper, which deals with only two patients, but, at the same time, call for future developments focused on such hypotheses.

Focusing on the qualitative comparison between the Newtonian and non-Newtonian model, Figure 7.9 shows an optimal agreement on the distribution of the TAWSS magnitude between the two models. These results reproduce the assumptions discussed by Liu et al. [117], who introduced that the blood viscosity properties do not affect the spatial pattern of the TAWSS qualitatively. However, looking at the luminal surface exposed to low and high TAWSS, the area with low TAWSS is greater in the Newtonian model for both the patients, while no significant difference occurs between the surfaces with high TAWSS. Our findings are in agreement with Soulis et al. [131] and Liu et al. [117], who proved an underestimated WSS given by the Newtonian model, when the magnitude of WSS is relatively small ($< 1\ N/m^2$). Analogously, we found similar results using the scenario A1, but with less marked differences, since the

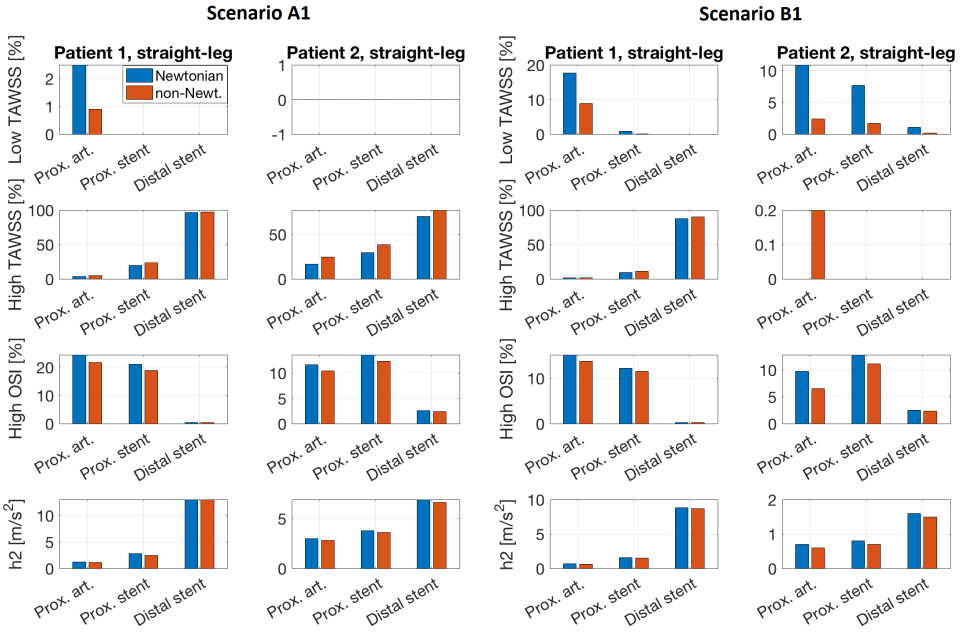

Figure 7.10: Comparison between results considering Newtonian and non-Newtonian behavior: bar plot of helicity (h_2 index), and percentage of luminal area exposed to both low (< 0.4 Pa) and high (> 1.5 Pa) TAWSS, respectively, and high OSI (> 0.3). The data are reported for the three zones under investigation (proximal artery, proximal stent, and distal stent) of the two patients in the straight-leg configuration, corresponding to scenarios A1 and B1.

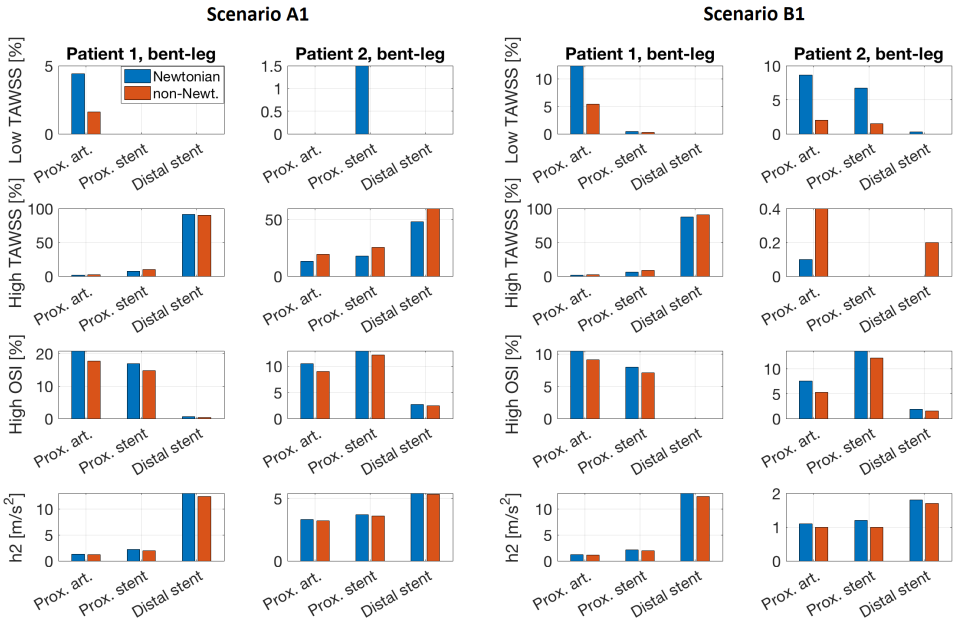

Figure 7.11: Comparison between results considering Newtonian and non-Newtonian behavior: bar plot of tortuosity, helicity (h_2 index), and percentage of luminal area exposed to both low (< 0.4 Pa) and high (> 1.5 Pa) TAWSS, respectively, and high OSI (> 0.3). The data are reported for the three zones under investigation (proximal artery, proximal stent, and distal stent) of the two patients in the bent-leg configuration, corresponding to scenarios A1 and B1.

surface exposed to low TAWSS is very small even in the Newtonian model. For this reason we chose to omit the qualitative analysis given by the scenario A1.

Figures 7.10 and 7.11 allow deepening the comparison between the Newtonian and non-Newtonian models. Significant differences based on the luminal surfaces exposed to low TAWSS are highlighted (with a maximum decrease in the proximal artery zone, compared to the non-Newtonian model, of 8.7% and 8.5% for Patients 1 and 2, respectively, in the straight-leg configuration and in the scenario B1), a good agreement occurs for the other analyzed outcomes (with a maximum OSI decrease in the proximal artery zone, compared to the non-Newtonian model, of 3.2% for patient 2 in the straight-leg configuration and in the scenario B1). In particular, as we mentioned before, the scenario B1, in which the inlet average velocity is lower and also low TAWSS values occur, provides major differences. As the velocity increases (see the results given by the scenario A1 in Figure 7.10), the Newtonian and non-Newtonian models become more similar, according to Liu et al. [117].

7.4.1 Limitations

The present work, based on the analysis of only two cases, represents a proof-of-concept study, aimed at linking post-stent geometry, hemodynamics, and thrombosis in endovascular repair of popliteal aneurysms. Further analyzes should be performed in order to obtain statistically and clinically relevant conclusions. We have already discussed the importance of considering patient-specific inlet boundary condition; therefore, in future studies inflow data elaborated by echo doppler measurements will be set at the inlet of the computational domain.

The computational domains considered in the simulations represent surrogate geometrical models of the lumen of each patient prior to thrombosis by virtually removing the thrombus during the segmentation process. Such a limitation could be overcome by analyzing the CT scans performed at different time instants, from early post-operative to annual follow-up exams.

In the present study we dealt with thrombosis only from a fluid dynamic point of view. However, further analysis should include the role of hemodynamic stress in the platelet activation [148], recently proved to be associated with aortic thrombus formation [53].

Finally, according to previous studies [120], [125], we did not take into account the stent struts; however, further developments will include this aspect, since Al-Hakim et al. [149] showed that stent struts have an effect on WSS.

7.4.2 Conclusions

The present study suggests that the overlapping of the stent-grafts seems to induce a severe discontinuity of lumen diameter, dividing the region treated with endovascular stent-graft into two zones: the proximal part, where thrombosis is located, it is characterized by low tortuosity, low velocity, low helicity, low TAWSS, and high OSI; the distal part that presents higher tortuosity, promoting higher velocity, higher helicity, higher TAWSS, and lower OSI. Since this analysis is limited to two cases, a further study with a cohort of patients should be investigated in order to generalize and validate our results. Boundary conditions affect the solution only when considering different velocity waveforms, dependent on time; different inlet velocity profiles and the use of flow extension do not provide significant variations. Accounting for actual flow rate is essential for accurate and reliable results. The Newtonian and non-Newtonian blood treatments provide similar results in both the patients, except when the magnitude of the TAWSS is relatively small (< 0.4 Pa). In this latter case the Newtonian model gives lower values of TAWSS than the non-Newtonian one. However, the Newtonian blood treatment should be a

good choice in all cases in which the analysis of WSS is not necessary. Leg bending induces significant hemodynamic differences compared to the straight leg configuration in each of the scenarios we studied for both patients. The helical form of intra-stent thrombosis suggests an implication of flow helicity in the onset and progression of thrombosis. However, further studies should be considered to investigate this aspect.

Chapter 8

Appendix 2

In this Appendix we report all the lumped parameter values estimated in the present thesis. In particular, the parameter values set in the Westerhof model are listed in Figure 8.1. Figure 8.2 reports the parameter values used in the thoracic aorta model (see Chapter 2).

Segment (D: paired segment)	Viscosity [P]	Density [g cm^{-3}]	Young's modulus [10^6 g cm^{-1} s^{-2}]	Thickness [cm]	Radius [cm]	Length [cm]	C/2 [10^{-6} g^{-1} cm^4 s^2]	R1 [g cm-4 s-1]	L1 [g cm^{-4}]	R2 [g cm-4 s-1]	L2 [g cm^{-4}]	R3 [g cm-4 s-1]	L3 [g cm^{-4}]	R4 [g cm-4 s-1]	L4 [g cm^{-4}]	R5 [g cm-4 s-1]	L5 [g cm^{-4}]
2A	0,03	1,049	4	0,164	1,47	2	2,670E-08	0,0327	3,090E-04	0,0654	1,030E-04	0,0982	6,181E-05	0,1309	4,415E-05	0,1636	3,434E-05
2B	0,03	1,049	4	0,161	1,44	2	2,558E-08	0,0355	3,221E-04	0,0711	1,074E-04	0,1066	6,441E-05	0,1421	4,601E-05	0,1777	3,578E-05
3A	0,03	1,049	4	0,132	1,12	2	1,480E-08	0,0971	5,324E-04	0,1942	1,775E-04	0,2913	1,065E-04	0,3884	7,605E-05	0,4855	5,915E-05
3B	0,03	1,049	4	0,127	1,07	3,9	2,618E-08	0,2273	1,137E-03	0,4546	3,791E-04	0,6819	2,275E-04	0,9092	1,625E-04	1,1365	1,264E-04
4A	0,03	1,049	4	0,12	0,999	5,2	3,012E-08	0,3988	1,740E-03	0,7977	5,799E-04	1,1965	3,480E-04	1,5954	2,485E-04	1,9942	1,933E-04
4B	0,03	1,049	4	0,09	0,675	5,2	1,260E-08	1,9136	3,811E-03	3,8272	1,270E-03	5,7408	7,622E-04	7,6544	5,444E-04	9,5680	4,234E-04
4C	0,03	1,049	4	0,087	0,645	5,2	1,140E-08	2,2952	4,174E-03	4,5905	1,391E-03	6,8857	8,347E-04	9,1809	5,962E-04	11,4761	4,637E-04
5A	0,03	1,049	4	0,084	0,61	5,3	1,022E-08	2,9243	4,756E-03	5,8485	1,585E-03	8,7728	9,512E-04	11,6971	6,794E-04	14,6214	5,284E-04
5B	0,03	1,049	4	0,082	0,58	5,3	9,038E-09	3,5779	5,261E-03	7,1558	1,754E-03	10,7336	1,052E-03	14,3115	7,515E-04	-	5,845E-04
5C	0,03	1,049	4	0,078	0,548	5,3	8,024E-09	4,4897	5,893E-03	8,9794	1,964E-03	13,4690	1,179E-03	17,9587	8,419E-04	-	6,548E-04
D 6A	0,03	1,049	4	0,063	0,368	5,8	3,415E-09	24,1601	1,430E-02	48,3201	4,767E-03	72,4802	2,860E-03	96,6403	2,043E-03	-	-
D 7A	0,03	1,049	4	0,055	0,29	5,8	1,958E-09	62,6466	2,303E-02	125,2932	7,676E-03	187,9397	4,606E-03	250,5863	3,290E-03	-	-
D 7B	0,03	1,049	4	0,055	0,29	2,5	8,441E-10	27,0028	9,926E-03	54,0057	3,309E-03	81,0085	1,985E-03	108,0113	1,418E-03	-	-
D 8A	0,03	1,049	16	0,052	0,255	6,3	3,891E-10	113,8259	3,235E-02	227,6519	1,078E-02	341,4778	6,470E-03	455,3037	4,622E-03	-	-
D 8B	0,03	1,049	16	0,046	0,186	6,3	1,797E-10	402,1149	6,081E-02	804,2298	2,027E-02	1.206,3446	1,216E-02	1.608,4595	8,686E-03	-	-
D 9A	0,03	1,049	4	0,053	0,27	6,1	1,739E-09	87,6872	2,794E-02	175,3744	9,313E-03	263,0616	5,588E-03	350,7488	3,991E-03	-	-
D 9B	0,03	1,049	4	0,052	0,259	6,1	1,573E-09	103,5600	3,036E-02	207,1201	1,012E-02	310,6801	6,073E-03	414,2401	4,338E-03	-	-
D 9C	0,03	1,049	4	0,051	0,249	6,1	1,432E-09	121,2255	3,285E-02	242,4509	1,095E-02	363,6764	6,570E-03	484,9018	4,693E-03	-	-
D 9D	0,03	1,049	4	0,05	0,238	6,1	1,284E-09	145,2390	3,596E-02	290,4781	1,199E-02	435,7171	7,192E-03	580,9562	5,137E-03	-	-
D 9E	0,03	1,049	4	0,049	0,225	7,1	1,300E-09	211,6360	4,683E-02	423,2721	1,561E-02	634,9081	9,366E-03	846,5442	6,690E-03	-	-
D 10A	0,03	1,049	8	0,048	0,213	6,3	5,041E-10	233,8210	4,637E-02	467,6420	1,546E-02	701,4630	9,273E-03	-	6,624E-03	-	-
D 10B	0,03	1,049	8	0,047	0,202	6,3	4,429E-10	289,0656	5,155E-02	578,1312	1,718E-02	867,1969	1,031E-02	-	7,365E-03	-	-
D 10C	0,03	1,049	8	0,046	0,19	6,3	3,808E-10	369,3070	5,827E-02	738,6140	1,942E-02	1.107,9209	1,165E-02	-	8,325E-03	-	-
D 11A	0,03	1,049	16	0,051	0,247	6,7	3,846E-10	137,5145	3,667E-02	275,0289	1,222E-02	412,5434	7,334E-03	-	5,239E-03	-	-
D 11B	0,03	1,049	16	0,049	0,219	6,7	2,849E-10	222,5152	4,665E-02	445,0304	1,555E-02	667,5456	9,329E-03	-	6,664E-03	-	-
D 11C	0,03	1,049	16	0,046	0,192	6,7	2,083E-10	376,6442	6,069E-02	753,2884	2,023E-02	1.129,9325	1,214E-02	-	8,670E-03	-	-
D 11D	0,03	1,049	16	0,044	0,165	6,7	1,426E-10	690,5584	8,217E-02	1.381,1167	2,739E-02	2.071,6751	1,643E-02	-	1,174E-02	-	-
D 11E	0,03	1,049	16	0,041	0,141	5,3	7,762E-11	1.024,3793	8,902E-02	2.048,7586	2,967E-02	3.073,1379	1,780E-02	-	-	-	-
D 12A	0,03	1,049	16	0,039	0,13	7,5	9,143E-11	2.006,0845	1,482E-01	4.012,1690	4,939E-02	6.018,2535	2,964E-02	-	-	-	-
D 12B	0,03	1,049	16	0,039	0,13	7,5	9,143E-11	2.006,0845	1,482E-01	4.012,1690	4,939E-02	6.018,2535	2,964E-02	-	-	-	-
D 12C	0,03	1,049	16	0,039	0,13	7,5	9,143E-11	2.006,0845	1,482E-01	4.012,1690	4,939E-02	6.018,2535	2,964E-02	-	-	-	-
D 12D	0,03	1,049	16	0,039	0,13	7,5	9,143E-11	2.006,0845	1,482E-01	4.012,1690	4,939E-02	6.018,2535	2,964E-02	-	-	-	-
D 12E	0,03	1,049	16	0,039	0,13	4,3	5,242E-11	1.150,1551	8,496E-02	2.300,3102	2,832E-02	3.450,4653	1,699E-02	-	-	-	-
13A	0,03	1,049	4	0,086	0,62	3,4	6,730E-09	1,7578	2,953E-03	3,5156	9,845E-04	5,2734	5,907E-04	7,0313	4,219E-04	-	-
14A	0,03	1,049	4	0,067	0,423	3,4	2,813E-09	8,1130	6,345E-03	16,2259	2,115E-03	24,3389	1,269E-03	32,4518	9,064E-04	-	-
D 14B	0,03	1,049	4	0,066	0,403	6,8	4,973E-09	19,6947	1,398E-02	39,3895	4,660E-03	59,0842	2,796E-03	78,7789	1,997E-03	-	-
D 15A	0,03	1,049	4	0,062	0,364	6,1	3,528E-09	26,5452	1,537E-02	53,0904	5,124E-03	79,6355	3,075E-03	106,1807	2,196E-03	-	-
D 15B	0,03	1,049	4	0,057	0,314	5,6	2,293E-09	44,0079	1,897E-02	88,0158	6,322E-03	132,0237	3,793E-03	176,0317	2,709E-03	-	-
D 16A	0,03	1,049	4	0,055	0,282	6,3	1,969E-09	76,1036	2,645E-02	152,2073	8,818E-03	228,3109	5,291E-03	-	3,779E-03	-	-
D 16B	0,03	1,049	4	0,053	0,266	6,3	1,724E-09	96,1336	2,973E-02	192,2673	9,910E-03	288,4009	5,946E-03	-	4,247E-03	-	-
D 16C	0,03	1,049	4	0,052	0,25	6,3	1,474E-09	123,2088	3,366E-02	246,4177	1,122E-02	369,6265	6,732E-03	-	4,808E-03	-	-
D 16D	0,03	1,049	4	0,05	0,236	4,6	9,459E-10	113,2847	2,758E-02	226,5694	9,193E-03	339,8540	5,516E-03	-	3,940E-03	-	-
D 17A	0,03	1,049	8	0,049	0,215	6,7	5,417E-10	239,5424	4,840E-02	479,0847	1,613E-02	718,6271	9,680E-03	-	6,914E-03	-	-
D 17B	0,03	1,049	8	0,047	0,203	6,7	4,774E-10	301,4061	5,429E-02	602,8122	1,810E-02	904,2183	1,086E-02	-	7,756E-03	-	-
D 17C	0,03	1,049	8	0,046	0,192	6,7	4,166E-10	376,6442	6,069E-02	753,2884	2,023E-02	1.129,9325	1,214E-02	-	8,670E-03	-	-
D 17D	0,03	1,049	8	0,045	0,183	3,7	2,051E-10	252,0338	3,689E-02	504,0675	1,230E-02	756,1013	7,378E-03	-	5,270E-03	-	-
D 18A	0,03	1,049	8	0,044	0,174	7,1	3,489E-10	591,7288	7,830E-02	1.183,4576	2,610E-02	1.775,1865	1,566E-02	-	1,119E-02	-	-
D 18B	0,03	1,049	8	0,043	0,162	7,1	2,923E-10	787,5165	9,033E-02	1.575,0330	3,011E-02	2.362,5495	1,807E-02	-	1,290E-02	-	-
D 18C	0,03	1,049	8	0,042	0,15	7,1	2,415E-10	1.071,4075	1,054E-01	2.142,8150	3,512E-02	3.214,2225	2,107E-02	-	-	-	-
D 18D	0,03	1,049	8	0,041	0,142	2,2	6,567E-11	413,3621	3,643E-02	826,7242	1,214E-02	1.240,0863	7,286E-03	-	-	-	-
D 19A	0,03	1,049	16	0,028	0,091	7,9	4,640E-11	8.800,8150	3,185E-01	17.601,6300	1,062E-01	-	6,371E-02	-	-	-	-
20A	0,03	1,049	4	0,064	0,39	1	6,838E-10	3,3022	2,195E-03	6,6044	7,318E-04	9,9066	4,391E-04	13,2088	3,136E-04	-	-
21A	0,03	1,049	4	0,045	0,18	7,1	7,528E-10	516,6896	7,317E-02	1.033,3791	2,439E-02	1.550,0687	1,463E-02	-	1,045E-02	-	-
22A	0,03	1,049	4	0,054	0,275	6,3	1,863E-09	84,1533	2,782E-02	168,3066	9,272E-03	252,4599	5,563E-03	-	3,974E-03	-	-
23A	0,03	1,049	4	0,049	0,22	6,6	1,137E-09	215,2358	4,553E-02	430,4717	1,518E-02	645,7075	9,107E-03	-	6,505E-03	-	-
D 24A	0,03	1,049	4	0,052	0,26	3,2	8,340E-10	53,4956	1,581E-02	106,9912	5,269E-03	160,4868	3,161E-03	-	2,258E-03	-	-
25AA	0,03	1,049	4	0,069	0,435	5,9	5,157E-09	12,5880	1,041E-02	25,1760	3,470E-03	37,7640	2,082E-03	50,3520	1,487E-03	-	-
25BA	0,03	1,049	4	0,043	0,16	5	3,981E-10	582,8428	6,522E-02	1.165,6856	2,174E-02	1.748,5284	1,304E-02	2.331,3712	9,317E-03	-	-
26AA	0,03	1,049	4	0,063	0,37	5,9	3,527E-09	24,0495	1,439E-02	48,0990	4,797E-03	72,1486	2,878E-03	96,1981	2,056E-03	-	-
26AB	0,03	1,049	4	0,063	0,37	5,9	3,527E-09	24,0495	1,439E-02	48,0990	4,797E-03	72,1486	2,878E-03	96,1981	2,056E-03	-	-
26AC	0,03	1,049	4	0,063	0,37	5,9	3,527E-09	24,0495	1,439E-02	48,0990	4,797E-03	72,1486	2,878E-03	96,1981	2,056E-03	-	-
26AD	0,03	1,049	4	0,063	0,37	3,1	1,853E-09	12,6362	7,561E-03	25,2724	2,520E-03	37,9086	1,512E-03	50,5448	1,080E-03	-	-
26AE	0,03	1,049	8	0,045	0,177	5,9	2,989E-10	459,2195	6,288E-02	918,4390	2,096E-02	1.377,6585	1,258E-02	-	8,983E-03	-	-
26AF	0,03	1,049	8	0,039	0,129	5,9	1,409E-10	1.627,6257	1,184E-01	3.255,2514	3,946E-02	4.882,8771	2,368E-02	-	-	-	-
26AG	0,03	1,049	16	0,026	0,083	5,9	2,849E-11	9.497,3187	2,860E-01	18.994,6374	9,532E-02	-	5,719E-02	-	-	-	-
26AH	0,03	1,049	8	0,045	0,177	5,9	2,989E-10	459,2195	6,288E-02	918,4390	2,096E-02	1.377,6585	1,258E-02	-	8,983E-03	-	-
26AI	0,03	1,049	8	0,039	0,129	5,9	1,409E-10	1.627,6257	1,184E-01	3.255,2514	3,946E-02	4.882,8771	2,368E-02	-	-	-	-
26AJ	0,03	1,049	16	0,026	0,083	5,9	2,849E-11	9.497,3187	2,860E-01	18.994,6374	9,532E-02	-	5,719E-02	-	-	-	-
26BA	0,03	1,049	4	0,063	0,37	5,9	3,527E-09	24,0495	1,439E-02	48,0990	4,797E-03	72,1486	2,878E-03	-	2,056E-03	-	-
26BB	0,03	1,049	4	0,063	0,37	5,9	3,527E-09	24,0495	1,439E-02	48,0990	4,797E-03	72,1486	2,878E-03	-	2,056E-03	-	-
26BC	0,03	1,049	4	0,063	0,37	5,9	3,527E-09	24,0495	1,439E-02	48,0990	4,797E-03	72,1486	2,878E-03	-	2,056E-03	-	-
26BD	0,03	1,049	8	0,045	0,177	5,9	2,989E-10	459,2195	6,288E-02	918,4390	2,096E-02	1.377,6585	1,258E-02	-	8,983E-03	-	-
26BE	0,03	1,049	8	0,039	0,129	5,9	1,409E-10	1.627,6257	1,184E-01	3.255,2514	3,946E-02	4.882,8771	2,368E-02	-	-	-	-
26BF	0,03	1,049	16	0,026	0,083	5,9	2,849E-11	9.497,3187	2,860E-01	18.994,6374	9,532E-02	-	5,719E-02	-	-	-	-
26BG	0,03	1,049	8	0,045	0,177	5,9	2,989E-10	459,2195	6,288E-02	918,4390	2,096E-02	1.377,6585	1,258E-02	-	8,983E-03	-	-
26BH	0,03	1,049	8	0,039	0,129	5,9	1,409E-10	1.627,6257	1,184E-01	3.255,2514	3,946E-02	4.882,8771	2,368E-02	-	-	-	-
26BI	0,03	1,049	16	0,026	0,083	5,9	2,849E-11	9.497,3187	2,860E-01	18.994,6374	9,532E-02	-	5,719E-02	-	-	-	-
D 27A	0,03	1,049	8	0,046	0,188	7,1	4,170E-10	434,1985	6,708E-02	868,3970	2,236E-02	1.302,5955	1,342E-02	-	9,582E-03	-	-
D 27B	0,03	1,049	8	0,045	0,183	7,7	4,269E-10	524,5027	7,677E-02	1.049,0054	2,559E-02	1.573,5081	1,535E-02	-	1,097E-02	-	-

Figure 8.1: Parameter values set in the arterial segments of the Westerhof model. The notation of the arterial segments is consistent with that in the Figure 2.3.

Segment (D: paired segment)	Viscosity [P]	Density [g cm^{-3}]	Young's modulus [10^6 g cm^{-1} s^{-2}]	Thickness [cm]	Radius [cm]	Length [cm]	C [10^{-6} g^{-1} cm^4 s^2]	R1 [g cm-4 s-1]	L1 [g cm^{-4}]	R2 [g cm-4 s-1]	L2 [g cm^{-4}]	R3 [g cm-4 s-1]	L3 [g cm^{-4}]	R4 [g cm-4 s-1]	L4 [g cm^{-4}]	R5 [g cm-4 s-1]	L5 [g cm^{-4}]
S1-S2	0,035	1,06	4	0,164	2,69	7,137	5,451E-07	0,0121	3,328E-04	0,0243	1,109E-04	0,0364	6,656E-05	0,0486	4,754E-05	0,0607	3,698E-05
S2-S3	0,035	1,06	4	0,161	3,367	1,32	1,977E-07	0,0009	3,929E-05	0,0018	1,310E-05	0,0027	7,857E-06	0,0037	5,612E-06	0,0046	4,365E-06
S3-S4	0,035	1,06	4	0,132	3,858	1,233	3,323E-07	0,0005	2,795E-05	0,0010	9,317E-06	0,0015	5,590E-06	0,0020	3,993E-06	0,0025	3,106E-06
S4-S5	0,035	1,06	4	0,127	4,106	3,256	1,094E-06	0,0010	6,516E-05	0,0020	2,172E-05	0,0031	1,303E-05	0,0041	9,309E-06	0,0051	7,240E-06
S5-S6	0,035	1,06	4	0,12	4,178	2,426	9,061E-07	0,0007	4,689E-05	0,0014	1,563E-05	0,0021	9,379E-06	0,0028	6,699E-06	0,0035	5,210E-06
S6-S7	0,035	1,06	4	0,09	3,572	4,964	1,537E-06	0,0027	1,313E-04	0,0054	4,376E-05	0,0082	2,625E-05	0,0109	1,875E-05	0,0136	1,459E-05
S7-S8	0,035	1,06	4	0,087	2,948	2,127	3,854E-07	0,0025	8,258E-05	0,0050	2,753E-05	0,0075	1,652E-05	0,0100	1,180E-05	0,0125	9,175E-06
S8-S9	0,035	1,06	4	0,084	2,353	4,021	3,871E-07	0,0117	2,450E-04	0,0234	8,168E-05	0,0351	4,901E-05	0,0468	3,501E-05	0,0585	2,723E-05
S9-S10	0,035	1,06	4	0,082	2,13	1,919	1,410E-07	0,0083	1,427E-04	0,0166	4,757E-05	0,0249	2,854E-05	0,0332	2,039E-05	0,0415	1,586E-05
BCT	0,035	1,06	4	0,078	1,188	1,919	2,672E-08	0,0859	4,588E-04	0,1717	1,529E-04	0,2576	9,175E-05	0,3435	6,554E-05	0,4293	5,097E-05
LCCA	0,035	1,06	4	0,063	0,638	0,655	1,830E-09	0,3523	5,429E-04	0,7047	1,810E-04	1,0570	1,086E-04	1,4094	7,756E-05	1,7617	6,033E-05
LSA	0,035	1,06	4	0,055	1,45	0,599	2,068E-08	0,0121	9,613E-05	0,0242	3,204E-05	0,0362	1,923E-05	0,0483	1,373E-05	0,0604	1,068E-05
RCA	0,035	1,06	4	0,055	0,336	1,9	9,662E-10	13,2863	5,678E-03	26,5726	1,893E-03	39,8590	1,136E-03	53,1453	8,112E-04	66,4316	6,309E-04
LCA	0,035	1,06	4	0,052	0,334	1,112	5,816E-10	7,9639	3,363E-03	15,9278	1,121E-03	23,8918	6,727E-04	31,8557	4,805E-04	39,8196	3,737E-04

Figure 8.2: Parameter values set in the arterial segments of the thoracic aorta model. The notation of the arterial segments is consistent with that in the Figure 2.10.

Chapter 9

List of Publications

1. A. Ferrarini, A. Finotello, G. Salsano, F. Auricchio, D. Palombo, G. Spinella, B. Pane, M. Conti. Impact of leg bending in the patient-specific computational fluid dynamics of popliteal stenting. Acta Mechanica Sinica (2021) 37(2):279–291

2. M. Conti, R. M. Romarowski, A. Ferrarini, M. Stochino, F. Auricchio, S. Morganti, L. K. von Segesser, E. Ferrari. Patient-specific computational fluid dynamics analysis of transcatheter aortic root replacement with chimney coronary grafts. Interactive CardioVascular and Thoracic Surgery (2020) 1–9

3. M. Conti, A. Ferrarini, A. Finotello, G. Salsano, F. Auricchio, D. Palombo, G. Spinella, B. Pane. Patient-specific computational fluid dynamics of femoro-popliteal stent-graft thrombosis. Medical Engineering and Physics 86 (2020) 57–64

Bibliography

[1] https://www.who.int

[2] Centers for Disease Control and Prevention. Underlying Cause of Death, 1999-2018. CDC WONDER Online Database. Atlanta, GA: Centers for Disease Control and Prevention; 2018. Accessed March 12, 2020.

[3] L. Formaggia, A. Quarteroni, A. Veneziani. Cardiovascular Mathematics. Springer, Volume 1, 2009.

[4] O. Frank. Die Grundfurm des artiriellen Puls. Zeitschrift fur Biologie. 37:483, 1899.

[5] G. N. Jager, N. Westerhof, A. Noordergraaf. Oscillatory Flow Impedance in Electrical Analog of Arterial System: Representation of Sleeve Effect and Non-Newtonian Properties of Blood. Circulation Research, 16:121-133, 1965.

[6] N. Westerhof, F. Bosman, C. J. De Vries, A. Noordergraaf. Analog studies of the human systemic arterial tree. J. Biomechanics, 2:121-143, 1969.

[7] A. P. Avolio. Multi-branched model of the human arterial system. Med & Biol. Eng. & Comput., 18:709-718, 1980.

[8] G. Schumacher, J. J. Kaden, F. Trinkmann. Multiple coupled resonances in the human vascular tree: refining the Westerhof model of the arterial system. J Appl Physiol, 124:131-139, 2018.

[9] M. Danielsen. Modeling of Feedback Mechanisms which Control the Heart Function in a View to an Implementation in Cardiovascular Models. Ph.D. Thesis, 13th July, 1998.

[10] L. Taelman, J. Degroote, P. Verdonck, J. Vierendeels, P. Segers. Modeling Hemodynamics in Vascular Networks Using a Geometrical Multiscale Approach: Numerical Aspects. Annals of Biomedical Engineering, 41:1445-1458, 2012.

[11] H. J. Kim, I. E. Vignol-Clementel, C. A. Figueroa, et al. On Coupling a Lumped Parameter Heart Model and a Three-Dimensional Finite Element Aorta Model. Annals of Biomedical Engineering, 37:2153-2169, 2009.

[12] K. Lagana, G. Dubini, F. Migliavacca, R. Pietrabissa, G. Pennati, et al. Multiscale modelling as a tool to prescribe realistic boundary conditions for the study of surgical procedures. Biorheology, 39:359-364, 2002.

[13] F. Migliavacca, R. Balossino, G. Pennati, G. Dubini, T. Y. Hsia, et al. Multiscale modelling in biofluidynamics: application to reconstructive paediatric cardiac surgery. J. Biomech., 39:1010-1020, 2006.

[14] A. Quarteroni, A. Veneziani. Analysis of a geometrical multiscale model based on the coupling of ODEs and PDEs for blood flow simulations. Multiscale Model. Simul., 1:173-195, 2003.

[15] E. B. Shim, R. D. Kamm, T. Heldt, R. G. Mark. Numerical analysis of blood flow through a stenosed artery using a coupled multiscale simulation method. In Computers in Cardiology, New York: IEEE, 27:219-222, 2000.

[16] A. P. Yoganathan, K. B. Chandran, F. Sotiropoulos. Flow in Prosthetic Heart Valves: State-of-the-Art and Future Directions. Annals of Biomedical Engineering, 33:1689-1694, 2005.

[17] J. Lantz, T. Ebbers, J. Engvall, M. Karlsson. Numerical and experimental assessment of turbulent kinetic energy in an aortic coarctation, Journal of Biomechanics, 46:1851-1858, 2013.

[18] H. Xu, D. Baroli, F. Di Massimo, A. Quaini, A. Veneziani. Backflow stabilization by deconvolution-based large eddy simulation modeling. Journal of Computational Physics, 404:109103, 2020.

[19] M. Conti, A. Ferrarini, A. Finotello, et al. Patient-specific computational fluid dynamics of femoro-popliteal stent-graft thrombosis. Med. Eng. Phys. 86:57-64, 2020.

[20] A. Ferrarini, A. Finotello, G. Salsano, F. Auricchio, D. Palombo, G. Spinella, B. Pane, M. Conti. Impact of leg bending in the patient-specific computational fluid dynamics of popliteal stenting. Acta Mechanica Sinica, 37(2):279-291, 2021.

[21] L. Formaggia, A. Veneziani. Reduced and multiscale models for the human cardiovascular system. Lecture notes VKI lecture series 7, 2003.

[22] A. Noordergraaf. Physical basis of ballistocardiography. Ph.D. Thesis. Univ. of Utrecht., 1956.

[23] A. Noordergraaf, H. B. K. Boom, P. D. Verdouw. A human systemic analog computer. In Proc. 1st Congr. Sot. for Ballistocardiographic Res., p. 23, 1960.

[24] J. R. Levick. An Introduction to Cardiovascular Physiology. Elsevier, 1991.

[25] R. Burattini. An arterial tree input impedance model: analysis in the frequency domain. Biomechanics, 10:20-29, 1981.

[26] R. Burattini, G. Gnudi. Computer identification of models for the arterial tree input impedance: Comparison between two new simple models and first experimental results. Med. & Biol. Eng. & Comput., 20, 134-144, 1982.

[27] K. Lu, J. W. Clark, F. H. Ghorbel, et al. A human cardiopulmonary system model applied to the analysis of the Valsalva maneuver. Am J Physiol Heart Circ Physiol, 28:H2661-H2679, 2001.

[28] D. A. Beard, K. H. Pettersen, B. E. Carlson, et al. A computational analysis of the long-term regulation of arterial pressure. F1000Research, 2:208, 2013.

[29] D. Canuto, K. Chong, C. Bowles, et al. A regulated multiscale closed-loop cardiovascular model, with applications to hemorrhage and hypertension. Int J Numer Meth Biomed Engng., 34:e2975, 2018.

[30] K. D. Lau, C. A. Figueroa. Simulation of short-term pressure regulation during the tilt test in a coupled 3D-0D closed-loop model of the circulation. Biomech Model Mechanobiol, 14:915-929, 2015.

[31] M. Conti, R. M. Romarowski, A. Ferrarini, et al. Patient-specific computational fluid dynamics analysis of transcatheter aortic root replacement with chimney coronary grafts. Interactive CardioVascular and Thoracic Surgery, 1-9, 2020.

[32] O. Franke. Die Grundform des arteriellen Pulses. Zeitung fur Biologie, 37:483-586, 1899.

[33] W. W. Nichols, M. F. O'Rourke. McDonald's Blood Flow in Arteries: Theoretical, Experimental and Clinical Principles. Hodder Arnold (4th ed.), London, 2005.

[34] T. M. van Bakel, C. J. Arthurs, F. J. Nauta, K. A. Eagle, J. A. van Herwaarden, F. L. Moll et al. Cardiac remodelling following thoracic endovascular aortic repair for descending aortic aneurysms. Eur J Cardiothorac Surg, 55:1061-70, 2019.

[35] A. Desyatova, J. MacTaggart, R. Romarowski, et al.: Effect of aging on mechanical stresses, deformations, and hemodynamics in human femoropopliteal artery due to limb flexion. Biomech. Model. Mechanobiol., 17:181-189, 2018.

[36] W. Nichols, M. F. O'Rourke, C. Vlachopoulos. McDonald's Blood Flow in Arteries, 6th edn. Hodder Arnold, London, 2011.

[37] M. B. Leon, C. R. Smith, M. J. Mack, R. R. Makkar, L. G. Svensson, S. K. Kodali et al. Transcatheter or surgical aortic-valve replacement in intermediate-risk patients. N Engl J Med, 374:1609-20, 2016.

[38] T. M. Van Bakel, C. J. Arthurs, J. A. Van Herwaarden, F. L. Moll, K. A. Eagle, H. J. Patel et al. A computational analysis of different endograft designs for Zone 0 aortic arch repair. Eur J Cardiothorac Surg, 54:389-96, 2018.

[39] F. Auricchio, M. Conti, S. Marconi, A. Reali, J. L. Tolenaar, S. Trimarchi. Patient-specific aortic endografting simulation: from diagnosis to prediction. Comput Biol Med, 43:386-94, 2013.

[40] P. Zhu, P. Zhou, X. Ling, B. E. Ohene, X. M. Bian, X. Jiang. Surgical treatment of mild to moderately dilated ascending aorta in bicuspid aortic valve aortopathy: the art of safety and simplicity. J Cardiothorac Surg, 15:6, 2020.

[41] C. Wang, E. Regar, M. Lachat, L. K. von Segesser, F. Maisano, E. Ferrari. Endovascular treatment of non-dissected ascending aorta disease: a systematic review. Eur J Cardiothorac Surg, 53:317-24, 2018.

[42] R. M. Romarowski, M. Conti, S. Morganti, V. Grassi, M. M. Marrocco-Trischitta, S. Trimarchi et al. Computational simulation of TEVAR in the ascending aorta for optimal endograft selection: a patient-specific case study. Comput Biol Med, 103:140-7, 2018.

[43] D. F. Gaia, O. Bernal, E. Castilho, C. B. N. D. Ferreira, D. Dvir, M. Simonato et al. First- in-human Endo-Bentall procedure for simultaneous treatment of the ascending aorta and aortic valve. J Am Coll Cardiol Case Rep, 2:480-5, 2020.

[44] E. Ferrari, M. Scoglio, G. Piazza, F. Maisano, V. Segesser, L. K. Berdajs. Transcatheter aortic root replacement with chimney grafts for coronary perfusion: a preliminary test in a three-dimensional-printed root model. Interact CardioVasc Thorac Surg, doi:10.1093/icvts/ivaa056, 2020.

[45] E. Ferrari, G. Piazza, M. Scoglio, D. Berdajs, P. Tozzi, F. Maisano et al. Suitability of 3D-printed root models for the development of transcatheter aortic root repair technologies. ASAIO J, 65:874-81, 2019.

[46] R. M. Romarowsky, A. Lefieux, S. Morganti, A. Veneziani, F. Auricchio. Patient-specific CFD modelling in the thoracic aorta with PC-MRI-based boundary conditions: A least-square three-element Windkessel approach. Int J Numer Meth Biomed Engng, 34:e3134, 2018.

[47] A. Updegrove, N. M. Wilson, J. Merkow, H. Lan, A. L. Marsden, S. C. Shadden. SimVascular: an open source pipeline for cardiovascular simulation. Ann Biomed Eng, 45:525-41, 2017.

[48] S. Sankaran, M. E. Moghadam, A. M. Kahn, E. E. Tseng, J. M. Guccione, A. L. Marsden. Patient-specific multiscale modeling of blood flow for coronary artery bypass graft surgery. Ann Biomed Eng, 40:2228-42, 2012.

[49] G. P. Toorop, N. Westerhof, G. Elzinga. Beat-to-beat estimation of peripheral resistance and arterial compliance during pressure transients. Am. J. Physiol. 252:H1275-H1283, 1987.

[50] H. J. Kim, I. E. Vignon-Clementel, J. S. Coogan, C. A. Figueroa, K. E. Jansen, C. A. Taylor. Patient-specific modeling of blood flow and pressure in human coronary arteries. Ann Biomed Eng, 38:3195-209, 2010.

[51] K. Johnson, P. Sharma, J. Oshinski. Coronary artery flow measurement using navigator echo gated phase contrast magnetic resonance velocity mapping at 3.0 t. J. Biomech, 41:595-602, 2008.

[52] N. Wilson, K. Wang, R. Dutton, C. Taylor. Medical Image Computing and Computer-Assisted Intervention-MICCAI 2001. A software framework for creating patient-specific geometric models from medical imaging data for simulation based medical planning of vascular surgery. Springer, 2001.

[53] F. J. Nauta, K. D. Lau, C. J. Arthurs, et al. Computational fluid dynamics and aortic thrombus formation following thoracic endovascular aortic repair. Ann. Thorac. Surg., 103:1914-1921, 2017.

[54] U. Morbiducci, R. Ponzini, G. Rizzo, M. Cadioli, A. Esposito, F. M. Montevecchi et al. Mechanistic insight into the physiological relevance of helical blood flow in the human aorta: an in vivo study. Biomech Model Mechanobiol,10:339-55, 2011.

[55] H. W. De Beaufort, M. Coda, M. Conti, T. M. Van Bakel, F. J. Nauta, E. Lanzarone et al. Changes in aortic pulse wave velocity of four thoracic aortic stent grafts in an ex vivo porcine model. PLoS One, 12:e0186080, 2017.

[56] F. J. H. Nauta, H. W. L. de Beaufort, M. Conti, S. Marconi, A. V. Kamman, A. Ferrara et al. Impact of thoracic endovascular aortic repair on radial strain in an ex vivo porcine model. Eur J Cardiothorac Surg, 51:783-9, 2017.

[57] A. Nardi, I. Avrahami. Approaches for treatment of aortic arch aneurysm, a numerical study. J Biomech, 50:158-65, 2017.

[58] R. Tricarico, Y. He, R. Tran-Son-Tay, L. Laquian, A. W. Beck, S. A. Berceli. Anatomic and hemodynamic investigation of an occluded common carotid chimney stent graft for hybrid thoracic aortic aneurysm repair. J Vasc Surg Cases Innov Tech, 5:187-94, 2019.

[59] U. Gulan, C. Calen, F. Duru, M. Holzner. Blood flow patterns and pressure loss in the ascending aorta: a comparative study on physiological and aneurysmal conditions. J Biomech, 76:152-9, 2018.

[60] H. W. de Beaufort, E. Cellitti, Q. M. de Ruiter, M. Conti, S. Trimarchi, F. L. Moll et al. Midterm outcomes and evolution of gutter area after endovascular aneurysm repair with the chimney graft procedure. J Vasc Surg, 67: 104-12, 2018.

[61] F. Auricchio, M. Conti, A. Lefieux, S. Morganti, A. Reali, F. Sardanelli et al. Patient-specific analysis of post-operative aortic hemodynamics: a focus on thoracic endovascular repair (TEVAR). Comput Mech, 54:943-53, 2014.

[62] V. Mendez, M. Di Giuseppe, S. Pasta. Comparison of hemodynamic and structural indices of ascending thoracic aortic aneurysm as predicted by 2-way FSI, CFD rigid wall simulation and patient-specific displacement-based FEA. Comput Biol Med, 100:221-9, 2018.

[63] J. H. Ferziger, M. Peric. Computational Methods for Fluid Dynamics. Springer, third edition, 2002.

[64] B. P. Leonard. A stable and accurate convective modelling procedure based on quadratic upstream interpolation. Comp. Meth. Appl. Mech. Eng., 19:59-98, 1979.

[65] P. Moin, J. Kim. Numerical investigation of turbulent channel flow. J Fluid Mech, 118:341-377, 1982.

[66] P. Sagaut. Large Eddy Simulation for Incompressible Flows. Springer, third edition, 2006.

[67] J. O. Hinze. Turbulence. McGraw-Hill Publishing Co., New York, 1975.

[68] F. Ducrous, F. Nicoud. Wall-adapting local eddy viscosity models for simulations in complex geometries. Flow, Turbulence and Combustion, 62(3):183-200, 1999.

[69] E. L. Manchester, S. Pirola, M. Y. Salmasi, D. P. O'Regan, T. Athanasiou, X. Y. Xu. Analysis of Turbulence Effects in a Patient-Specific Aorta with Aortic Valve Stenosis. Cardiovascular Engineering and Technology, https://doi.org/10.1007/s13239-021-00536-9, 2021.

[70] J. Liu, J. Niu, Y. Du, C. M. Mak, Y. Zhang. LES for pedestrian level wind around an idealized building arra–Assessment of sensitivity to influencing parameters. Sustainable Cities and Society, 44:406-415, 2019.

[71] U. Piomelli. Wall-layer models for large-eddy simulations. Progress in Aerospace Sciences, 44(6):437-446, 2008.

[72] H. B. Toda, O. Cabrit, G. Balarac, S. Bose, J. Lee, H. Choi, F. Nicoud. A subgrid-scale model based on singular values for LES in complex geometries. Center for Turbulence Research, Proceedings of the Summer Program 2010, 2010.

[73] A. Yoshizawa, K. Horiuti. A statistically-derived subgrid-scale kinetic energy model for the large-eddy simulation of turbulent flows. Journal of the Physical Society of Japan, 54:2834-39, 1985.

[74] J. Smagorinsky. General circulation experiments with the primitive equations. American Meteorological Society, 91(3):99-164, 1963.

[75] D. K. Lilly. The representation of small-scale turbulence in numerical simulation experiments. Proceedings of the IBM Scientific Computing Symposium on Environmental Sciences, 1967.

[76] A. Leonard. Energy cascade in large-eddy simulations of turbulent fluid flows. Advances in Geophysics, 18:237-48, Part A,1975.

[77] J. W. Deardorff. A numerical study of three-dimensional turbulent channel flow at large Reynolds numbers. Journal of Fluid Mechanics, 41(2):453-80, 1970.

[78] J. W. Deardorff. The use of subgrid transport equations in a three-dimensional model of atmospheric turbulence. Journal of Fluids Engineering, 95(3):429-38, 1973.

[79] J. Bo. Implementation and assessment of subgrid-scale models for large eddy simulations of incompressible turbulent flows. Thesis for the degree of Master of Science, University of Oslo, 2015.

[80] S. B. Pope. Turbulent Flows. Cambridge University Press, 2000.

[81] O. J. McMillan, J. H. Ferziger. Direct testing of subgrid-scale models. AIAA J., 17:1340-1346, 1979.

[82] D. K. Lilly. On the application of the eddy-viscosity concept in the inertial sub-range of turbulence. Tech. Rep., 123, 1966.

[83] F. P. P. Tan, N. B. Wood, G. Tabor, X. Y. Xu. Comparison of LES of Steady Transitional Flow in an Idealized Stenosed Axisymmetric Artery Model With a RANS Transitional Model. ASME J. Biomech. Eng., 133(5):051001, 2011.

[84] A. Pal, K. Anupindi, Y. Delorme, N. Ghaisas, D. A. Shetty, S. H. Frankel. Large Eddy Simulation of Transitional Flow in an Idealized Stenotic Blood Vessel: Evaluation of Subgrid Scale Models. Journal of Biomechanical Engineering, 136:071009-8, 2014.

[85] S. N. Hasham, D. Guo, D. M. Milewicz. Genetic basis of thoracic aortic aneurysms and dissections. Current Opinion in Cardiology,17(6):677-683, 2002.

[86] `https://www.german-heart-centre.com/news/can-you-live-with-a-thoracic-aortic-aneurysm/`

[87] S. Focardi. Fisica generale: meccanica e termodinamica. 2. ed, CEA, 2014.

[88] S. Zuccher. Note di Fluidodinamica. Note of the bachelor course *Dinamica dei Fluidi*, University of Verona, 2020.

[89] P. Catalano, M. Wang, G. Iaccarino, P. Moin. Numerical simulation of the flow around a circular cylinder at high Reynolds numbers. International Journal of Heat and Fluid Flow, 24:463-469, 2003.

[90] N. H. Johari, N. B. Wood, Z. Cheng, R. Torii, M. Oishi, M. Oshima, X. Y. Xu. Disturbed Flow in a Stenosed Carotid Artery Bifurcation: Comparison of RANS-Based Transitional Model and LES with Experimental Measurements. International Journal of Applied Mechanics, 11:1950032, 2019.

[91] J. Meyers, P. Sagaut. On the Required Reynolds-number Dependence of Variational Multi-scale Smagorinsky Models. ECCOMAS CFD, 2006.

[92] J. Lantz, R. Gardhagen, M. Karlsson. Quantifying turbulent wall shear stress in a subject specific human aorta using large eddy simulation. Medical Engineering & Physics, 34:1139-1148, 2012.

[93] M. Andersson, J. Lantz, T. Ebbers, M. Karlsson. Multidirectional WSS disturbances in stenotic turbulent flows: A pre- and post-intervention study in an aortic coarctation. Journal of Biomechanics, 51:8-16, 2017.

[94] M. S. Zakaria, F. Ismail, M. Tamagawa, A. F. A. Azi, S. Wiriadidjaya, A. A. Basri, K. A. Ahmad. Computational Fluid Dynamics Study of Blood Flow in Aorta using OpenFOAM. Journal of Advanced Research in Fluid Mechanics and Thermal Sciences, 43(1):81-89, (2018).

[95] F. Auricchio, M. Conti, A. Lefieux, et al. Patient-specific analysis of post-operative aortic hemodynamics: a focus on thoracic endovascular repair (TEVAR). Comput Mech., 54(4):943-953, 2014.

[96] G. H. W. van Bogerijen, F. Auricchio, M. Conti, et al. Aortic hemodynamics after thoracic endovascular aortic repair, with particular attention to the bird-beak configuration. J Endovasc Ther., 21(6):791-802, 2014.

[97] L. Antiga, M. Piccinelli, L. Botti, B. Ene-Iordache, A. Remuzzi, D. A. Steinman. An image-based modeling framework for patient-specific computational hemodynamics. Med Biol Eng Comput., 46(11):1097-1112, 2008.

[98] N. Westerhof, J. W. Lankhaar, B. E. Westerhof. The arterial windkessel. Med. Biol. Eng. Comput., 47:131-141, 2009.

[99] `https://www.paraview.org`

[100] ANSYS Fluent Theory Guide. Release 15.0, 2013.

[101] U. Morbiducci, R. Ponzini, D. Gallo, et al. Inflow boundary conditions for image-based computational hemodynamics: Impact of idealized versus measured velocity profiles in the human aorta. J. Biomech., 46:102-109, 2013.

[102] K. Lagan, R. Balossino, F. Migliavacca, G. Pennati, E. L. Bove, M. R. de Leval, G. Dubini. Multiscale modeling of the cardiovascular system: application to the study of pulmonary and coronary perfusions in the univentricular circulation. J Biomech, 38(5):1129-1141, 2005.

[103] C. A. Taylor, C. P. Cheng, L. A. Espinosa, B. T. Tang,D. Parker, R. J. Herfkens. In vivo quantification of blood flow and wall shear stress in the human abdominal aorta during lower limb exercise. Ann Biomed Eng, 30:402-408, 2002.

[104] D. Chen, M. Muller-Eschner, D. Kotelis, D. Bockler, Y. Ventikos, H. von Tengg-Kobligk. A longitudinal study of Type-B aortic dissection and endovascular repair scenarios: Computational analyses. Medical Engineering & Physics, 35:1321-1330, 2013.

[105] S. Gupta, A. R. Popescu, R. De Freitas, D. Thakrar, J. Puthumana, J. Carr, M. Markl. Four-dimensional magnetic resonance flow analysis clarifies paradoxical symptoms in a patient with aortic bypass and retrograde flow mimicking subclavian steal. Circulation, 125(6):e347-e349, 2012.

[106] Y. Amano, R. Takagi, Y. Suzuki, T. Sekine, S. Kumita, M. van Cauteren. Three-dimensional velocity mapping of thoracic aorta and supra-aortic arteries in Takayasu arteritis. J. Magn. Reson. Imaging, 31(6):1481-1485, 2010.

[107] P. Vasava, P. Jalali, M. Dabagh, P.J. Kolari. Finite element modelling of pulsatile blood flow in idealized model of human aortic arch: study of hypotension and hypertension. Comput. Math. Methods Med., 2012.

[108] J. Sotelo, J. Urbina, I. Valverde, C. Tejos, P. Irarrazaval, M. E. Andia, S. Uribe, D. E. Hurtado. 3D Quantification of Wall Shear Stress and Oscillatory Shear Index Using a Finite-Element Method in 3D CINE PC-MRI Data of the Thoracic Aorta. IEEE TRANSACTIONS ON MEDICAL IMAGING, 35(6):1475-1487, 2016.

[109] A. M. Malek, S. L. Alper, S. Izumo. Hemodynamic shear stress and its role in atherosclerosis. J. Am. Med. Assoc., 282:2035-2042, 1999.

[110] R. Jayendiran, F. Condemi, S. Campisi, M. Viallon, P. Croisille, S. Avril. Correlation Between Hemodynamics and Morphology of Ascending Thoracic Aortic Aneurysms. 6^{th} International Conference on Computational and Mathematical Biomedical Engineering - CMBE2019, 10-12 June 2019, Japan.

[111] Y. Mano, Y. Takehara, T. Sakaguchi, M.T. Alley, H. Isoda, T. Shimizu, T. Wakayama, M. Sugiyama, H. Sakahara, H. Konno, N. Unno. Hemodynamic Assessment of Celiaco-mesenteric Anastomosis in Patients with Pancreaticoduodenal Artery Aneurysm Concomitant with Celiac Artery Occlusion using Flow-sensitive Four-dimensional Magnetic Resonance Imaging. European Journal of Vascular and Endovascular Surgery, 46(3):321-328, 2013.

[112] P. K. Singh, A. Marzo, B. Howard, D. A. Rufenacht, P. Bijlenga, A. F. Frangi, P. V. Lawford, S. C. Coley, D. R. Hose, U. J. Patel. Effects of smoking and hypertension on wall shear stress and oscillatory shear index at the site of intracranial aneurysm formation. Clinical Neurology and Neurosurgery, 112:306-313, 2010.

[113] M. Alimohammadi, O. Agu, S. Balabania, Va. Diaz-Zuccarini. Development of a patient-specific simulation tool to analyse aortic dissections: Assessment of mixed patient-specific flow and pressure boundary conditions. Medical Engineering & Physics, 36:275-284, 2014.

[114] G.-Y. Zhu, Y. Wei, Y.-L. Su, Q. Yuan, C.-F. Yang. Impacts of Internal Carotid Artery Revascularization on Flow in Anterior Communicating Artery Aneurysm: A Preliminary Multiscale Numerical Investigation. Appl. Sci., 9:1-14, 2019.

[115] D. Gallo, D. A. Steinman, P. B. Bijari, U. Morbiducci. Helical flow in carotid bifurcation as surrogate marker of exposure to disturbed shear. Journal of Biomechanics, 45:2398-2404, 2012.

[116] T. A. Hope, M. D. Hope, D. D. Purcell, C. von Morze, D. B. Vigneron, M. T. Alley, W. P. Dillon. Evaluation of intracranial stenoses and aneurysms with accelerated 4D flow. Magnetic Resonance Imaging, 28:41-46, 2010.

[117] B. Liu, D. Tang. Influence of non-Newtonian properties of blood on the wall shear stress in human atherosclerotic right coronary arteries. Mol. Cell Biomech. 8:73-90, 2011.

[118] I. F. Tielliu, C. J. Zeebregts, G. Vourliotakis, et al. Stent fractures in the Hemobahn/Viabahn stent graft after endovascular popliteal aneurysm repair. J. Vasc. Surg., 51(6):1413-1418, 2010.

[119] H. B. Smouse, A. Nikanorov, D. LaFlash. Biomechanical forces in the femoropopliteal arterial segment. Endovasc. Today, 4(6):60-66, 2005.

[120] C. Gokgol, N. Diehm, L. Raber, et al. Prediction of restenosis based on hemodynamical markers in revascularized femoro-popliteal arteries during leg flexion. Biomech. Model. Mechanobiol., 18:1883-1893, 2019.

[121] S. Glagov, C. Zarins, D. P. Giddens, et al. Hemodynamics and atherosclerosis. Insights and perspectives gained from studies of human arteries. Arch. Pathol. Lab. Med., 112(10):1018-1031, 1988.

[122] L. D. Casa, D. H. Deaton, D. N. Ku. Role of high shear rate in thrombosis. J. Vasc. Surg., 61(4):1068-1080, 2015.

[123] N. B. Wood, S. Z. Zhao, A. Zambanini, et al. Curvature and tortuosity of the superficial femoral artery: a possible risk factor for peripheral arterial disease. J. Appl. Physiol., 101(5):1412-1418, 2006.

[124] A. Desyatova, W. Poulson, P. Deegan, et al. Limb flexion induced twist and associated intramural stresses in the human femoropopliteal artery. J. R. Soc. Interface, 14:20170025, 2017.

[125] M. Colombo, M. Bologna, M. Garbey, et al. Computing patient-specific hemodynamics in stented femoral artery models obtained from computed tomography using a validated 3D reconstruction method. Med. Eng. Phys., 75:23-35, 2020

[126] M. Colombo, G. Luraghi, L. Cestariolo, et al. Impact of lower limb movement on the hemodynamics of femoropopliteal arteries: a computational study. Med. Eng. Phys. 81:105-117, 2020.

[127] E. W. Merrill. Rheology of blood. Physiol. Rev., 49:863-888, 1969.

[128] D. M. Wootton, D. N. Ku. Fluid mechanics of vascular systems, diseases, and thrombosis. Annu. Rev. Biomed. Eng., 1:299-329, 1999.

[129] Y. I. Cho, K. R. Kensey. Effects of the non-Newtonian viscosity of blood on flows in a diseased arterial vessel. Part 1: Steady flows. Biorheology 28, 241-262, 1991.

[130] B. M. Johnston, P. R. Johnston, S. Corney, et al. Non-Newtonian blood flow in human right coronary arteries: transient simulations. J. Biomech., 39:1116-1128, 2005.

[131] J. V. Soulis, G. D. Giannoglou, Y. S. Chatzizisis, et al. Spatial and phasic oscillation of non-Newtonian wall shear stress in human left coronary artery bifurcation: an insight to atherogenesis. Coron. Artery Dis., 17:351-358, 2006.

[132] Y. Hua, J. H. Oh, Y. B. Kim. Influence of parent artery segmentation and boundary conditions on hemodynamic characteristics of intracranial aneurysms. Yonsei Med. J., 56:1328-1337, 2015.

[133] G. Spinella, A. Finotello, B. Pane, et al. In vivo morphological changes of the femoropopliteal arteries due to knee flexion after endovascular treatment of popliteal aneurysm. J. Endovasc. Ther., 26(4):496-504, 2019.

[134] L. Antiga, M. Piccinelli, L. Botti, et al. An image-based modeling framework for patient-specific computational hemodynamics. Med. Biol. Eng. Comput., 46(11):1097, 2008.

[135] M. Piccinelli, A. Veneziani, D. A. Steinman, et al. A framework for geometric analysis of vascular structures: application to cerebral aneurysms. IEEE Trans. Med. Imaging, 28(8):1141-1155, 2009.

[136] J. K. W. Chesnutt, H.-C. Han. Tortuosity triggers platelet activation and thrombus formation in microvessels. J. Biomech. Eng., 133:121004-1, 2011. https://doi.org/10.1115/1.4005478

[137] W. Quanyu, L. Xiaojie, P. Lingjiao, et al. Simulation analysis of blood flow in arteries of the human arm. Biomed. Eng., 29:1750031-8, 2017.

[138] J. D. Crawford, N. G. Robbins, L. A. Harry, et al. Characterization of tibial velocities by duplex ultrasound in severe peripheral arterial disease and controls. J. Vasc. Surg., 63:646-651, 2016.

[139] U. Morbiducci, D. Gallo, D. Massai, et al. Outflow conditions for image-based hemodynamic models of the carotid bifurcation: implications for indicators of abnormal flow. J. Biomech. Eng. 132, 091005-1, 2010.

[140] U. Morbiducci, R. Ponzini, D. Gallo, et al. Inflow boundary conditions for image-based computational hemodynamics: Impact of idealized versus measured velocity profiles in the human aorta. J. Biomech. 46:102-109, 2013.

[141] A. J. Boyd, D. C. S. Kuhn, R. J. Lozowy, et al. Low wall shear stress predominates at sites of abdominal aortic aneurysm rupture. J. Vasc. Surg. 63:1613-1619, 2016.

[142] C. Caro, N. Watkins, S. Sherwin. Helical graft. Patent, US 2007/0021707 A1, 2007.

[143] U. Morbiducci, R. Ponzini, M. Grigioni, et al. Helical flow as fluid dynamic signature for atherogenesis risk in aortocoronary bypass. A numeric study. J. Biomech. 40:519-34, 2007.

[144] Y. Qiu, D. Yuan, Y. Wang, et al. Hemodynamic investigation of a patient-specific abdominal aortic aneurysm with iliac artery tortuosity. Comput. Methods Biomech. Biomed. Eng., 21:824-833, 2018.

[145] P. J. W. Wensing, F. G. Scholten, P. C. Buijs, et al. Arterialtortuosity in the femoropopliteal region during knee flexion: a magnetic resonance angiographic study. J. Anat., 186:133-139, 1995.

[146] M. Conti, M. Marconi, G. Campanile, et al. Patient-specific finite element analysis of popliteal stenting. Meccanica, 52:633-644, 2017.

[147] G. Spinella, A. Finotello, B. Pane, B., et al. In vivo morphological changes of the femoropopliteal arteries due to knee flexion after endovascular treatment of popliteal aneurysm. J. Endovasc. Ther. 43:1-9, 2019.

[148] S. C. Shadden, S. Hendabadi. Potential fluid mechanic pathways of platelet activation. Biomech. Model. Mechanobiol., 12(3):467-474, 2013.

[149] R. Al-Hakim, E. W. Lee, S. T. Kee, et al. Hemodynamic analysis of edge stenosis in peripheral artery stent grafts. Diagn. Interv. Imaging, 98:729-735, 2017.